AD-A100 289 AIR FORCE GEOPHYSICS LAB HANSCOM AFB MA F/G 3/1
AN INFRARED SURVEY OF THE DIFFUSE EMISSION WITHIN 5 DEG OF THE --ETC(U)
JUN 80 S D PRICE, L P MARCOTTE
UNCLASSIFIED AFGL-TR-80-0182 NL

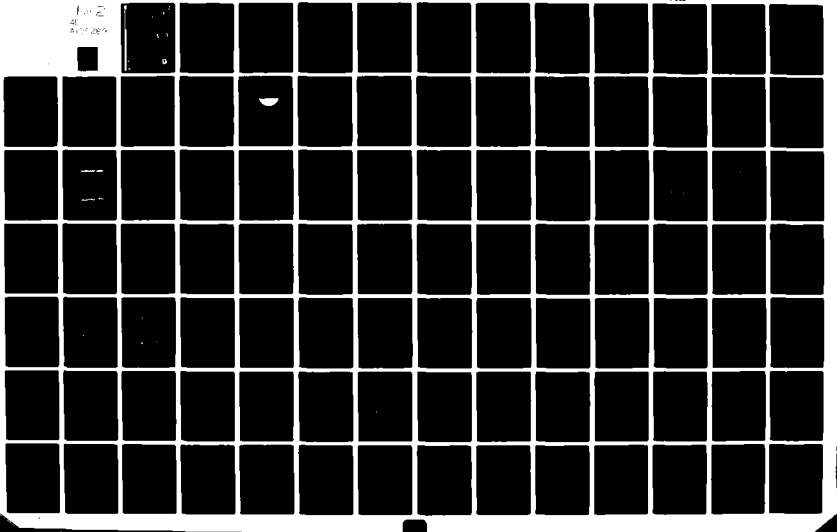

AD A100289

AFGL-TR-80-0182
ENVIRONMENTAL RESEARCH PAPERS, NO. 705

12

LEVEL II

An Infrared Survey of the Diffuse Emission Within 5° of the Galactic Plane

STEPHEN D. PRICE
LEONARD P. MARCOTTE

DTIC
ELECTE
JUN 16 1981
S D
E

5 June 1980

Approved for public release; distribution unlimited.

OPTICAL PHYSICS DIVISION PROJECT 7670
AIR FORCE GEOPHYSICS LABORATORY
HANSCOM AFB, MASSACHUSETTS 01731

AIR FORCE SYSTEMS COMMAND, USAF

DTIC FILE COPY

81 6 15 182

This report has been reviewed by the ESD Information Office (OI) and is releasable to the National Technical Information Service (NTIS).

This technical report has been reviewed and is approved for publication.

FOR THE COMMANDER

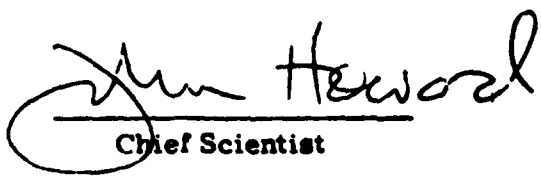

Chief Scientist

Qualified requestors may obtain additional copies from the Defense Technical Information Center. All others should apply to the National Technical Information Service.

9 Environmental research papers.

Unclassified

SECURITY CLASSIFICATION OF THIS PAGE (When Data Entered)

REPORT DOCUMENTATION PAGE	READ INSTRUCTIONS BEFORE COMPLETING FORM
1 REPORT NUMBER: AFGL-TR-80-0182	2 GOVT ACCESSION NO: AD-A100 289
3 RECIPIENT'S CATALOG NUMBER	
4 TITLE (and Subtitle): AN INFRARED SURVEY OF THE DIFFUSE EMISSION WITHIN 5 deg OF THE GALACTIC PLANE	5 TYPE OF REPORT & PERIOD COVERED: Scientific. Interim.
6 PERFORMING ORG. REPORT NUMBER: ERP No. 705	
7 AUTHOR(s): Stephan D. Price, Leonard P. Marcotte	8 CONTRACT OR GRANT NUMBER(s)
9 PERFORMING ORGANIZATION NAME AND ADDRESS: Air Force Geophysics Laboratory (OP), Hanscom AFB, Massachusetts 01731	10 PROGRAM ELEMENT, PROJECT, TASK AREA & WORK UNIT NUMBERS: 62101F, 7670 06 08
11 CONTROLLING OFFICE NAME AND ADDRESS: Air Force Geophysics Laboratory (OP), Hanscom AFB, Massachusetts 01731	12 REPORT DATE: 5 June 1980
	13 NUMBER OF PAGES: 170
14 MONITORING AGENCY NAME & ADDRESS (if different from Controlling Office): AFGL-TR-80-0182, AFGL-ERP-705	15 SECURITY CLASS (of this report): Unclassified
	15a DECLASSIFICATION/DOWNGRADING SCHEDULE

16 DISTRIBUTION STATEMENT (of this Report)

Approved for public release; distribution unlimited.

17 DISTRIBUTION STATEMENT (of the abstract entered in Block 20, if different from Report)

18 SUPPLEMENTARY NOTES

19 KEY WORDS (Continue on reverse side if necessary and identify by block number)

Infrared
Diffuse emission
Galactic structure
HII regions

20 ABSTRACT (Continue on reverse side if necessary and identify by block number)

The AFGL Infrared Sky Survey data have been processed to deconvolve the low frequency attenuation, restoring the signals from extended sources. The 11 and 20-μm scans which cover three quarters of the galactic plane have been analyzed, with lesser area covered at 4 and 27 μm. A detailed description is given of the instrumentation, the conduct of the experiment, and the data reduction procedures. The measured extended emission in the 3- to 30-μm region may be divided into several components. A number of discrete,

DD FORM 1 JAN 73 1473 EDITION OF 1 NOV 65 IS OBSOLETE

Unclassified

SECURITY CLASSIFICATION OF THIS PAGE (When Data Entered)

Unclassified

SECURITY CLASSIFICATION OF THIS PAGE(When Data Entered)

20. Abstract (Continued)

extended sources are observed within 5° of the galactic plane, the majority of which are associated with HII regions. About 25 percent of these sources are not in the AFGL catalog. A large scale diffuse emission is centered on the galactic plane at longitudes less than 90° from the galactic center. The 11 to 20-μm color ratio of this emission is distinctly smaller in the direction of the Perseus external arm and the Sagittarius-Carina spiral than closer to the center ($|l| < 65°$). Most of this background is probably due to thermal radiation from HII regions along the line of sight. Interior to ± 65°, the 4-μm measurements can be understood in terms of the 2.4-μm balloon-borne survey observation and interpreting the background at both wavelengths as being due to late type stars. The 20-μm values over these longitudes are probably due to HII regions. Additional 11-μm sources are required to explain the measured values. Appendices A, B, and D present higher resolution data than previously discussed and, for the longitude regions which contain diffuse background, intensity grids with entries every 0.°1 in latitude and longitude.

Unclassified

SECURITY CLASSIFICATION OF THIS PAGE(When Data Entered)

Accession For
NTIS GRA&I
DTIC TAB
Unannounced
Justification
By
Distribution/
Availability Codes
Dist Special
A

Preface

The intensities given in the text are based upon point source calibrations. After this report was completed, the calibration was reexamined. Electrical and optical crosstalk between detectors in the array was found to be of about 6 percent for the individual phenomenon. Further, a low level response on the order of 1 to 3 percent was measured off the detector by the sensor manufacturer. Although these effects are "calibrated out" of the point source photometry, they will produce an erroneously high measurement on extended sources; the behavior is analogous to increasing the effective field of view for each detector. All the intensity values in this report should be multiplied by 0.7 to correct for these effects.

Contents

1.	INTRODUCTION	9
2.	INSTRUMENTATION	10
	2.1 Telescope–Sensor System	10
	2.2 Payload	13
3.	THE EXPERIMENT	14
	3.1 Experiment Profile	14
	3.2 The Survey Data	15
4.	DATA REDUCTION	20
5.	RESULTS	35
	5.1 Longitudes 0° to 35°	35
	5.2 Longitudes 35° to 95°	42
	5.3 Longitudes 100° to 240°	49
	5.4 Longitudes 280° to 320°	49
6.	DISCUSSION	58
7.	CONCLUSION	67
REFERENCES		69
APPENDIX A:	Intensity Grids for the 4, 11, and 20-μm Spectral Bands Over the Region $-0.7 \leq \ell < 30^{o}$, $\lvert b \rvert \leq 4^{o}$	73
APPENDIX B:	Intensity Grids at 11, 20, and 27 μm of the Galactic Plane Between 35° and 95° Longitude	99
APPENDIX C:	Diffuse 11 and 20-μm Measurements Along the Galactic Plane Between 100° and 240° Longitude	137

PRECEDING PAGE BLANK-NOT FILMED

Contents

APPENDIX D: Intensity Grids in the 11, 20 and 27-μm Spectral Bands Covering the Region $280^{\circ} \lesssim \ell \lesssim 320^{\circ}$, $|b| \lesssim 4^{\circ}$ 141

Illustrations

1. Configuration of the Focal Plane Array 11
2. Cross-Section Schematic of the Infrared Survey Telescope 12
3. Schematic of the Rocket Payload Used for the Infrared Survey 13
4. The Survey Scan Geometry 16
5. Example of a Point Source Signature 17
6. Extended Source Signature 18
7. Impulse Response 19
8. Uncompensated Output for a Galactic Plane Crossing 21
9a. Uncompensated 11-μm Data for an 11-μm Scan Along the Galactic Plane 26
9b. Rectified Output for the Data in Figure 9a 26
10a. Uncompensated Data for the 11-μm Channel Adjacent to that in Figure 9a 27
10b. Rectified Output from the Data in Figure 10a 27
11a. Uncompensated 20-μm Output for a Scan Along the Galactic Plane 28
11b. Rectified Output from Data in Figure 11a 28
12. Rectified 11-μm Scans Across the Galactic Plane 30
13. Contour Maps at 11, 20 and 4 μm for the Region $0^{\circ} \lesssim \ell < 35^{\circ}$ 36
14. 4-μm Contour Map for the Region $0^{\circ} \lesssim \ell < 30^{\circ}$ 37
15. 11-μm Contour Map for the Region $0^{\circ} \lesssim \ell < 35^{\circ}$ 37
16. 20-μm Contour Map for the Region $0^{\circ} \lesssim \ell < 35^{\circ}$ 38
17. The 11, 20 and 27-μm Equal Intensity Contour Maps of the Galactic Plane in the Region $35^{\circ} < \ell < 95^{\circ}$ 43
18. 11-μm Map of the Galactic Plane over the Region $35^{\circ} < \ell < 95^{\circ}$ 43
19. 20-μm Map of the Galactic Plane from 35° to 95° Longitude 44
20. The 27-μm Map of the Galactic Plane Between 40° and 85° Longitude 44
21. The 11 and 20-μm Map of the Galactic Plane for Longitude Between 100° and 170° 50
22. An Expanded Version of the 11-μm Map in Figure 21 50

Illustrations

23. An Expanded Version of the 20-μm Map in Figure 21 51
24. 11 and 20-μm Maps of the Galactic Plane from 195° to 240° Longitude 51
25. Expanded Version of the 11-μm Map in Figure 24 52
26. Expanded Version of the 20-μm Map in Figure 24 52
27. The 11, 20 and 27-μm Equal Intensity Contour Maps of the Galactic Plane from 280° to 320° Longitude 55
28. 11-μm Contour Map Along the Galactic Plane from 280° to 320° Longitude 56
29. The 20-μm Map of the Galactic Equator Region Between 280° and 320° Longitude 56
30. An Expanded Version of the 27-μm Map in Figure 27 58
31. The 4-μm Surface Brightness Along the Galactic Equator 60
32. The 11-μm Surface Brightness Measured Along the Galactic Plane 61
33. The 20-μm Surface Brightness Measured Along the Galactic Plane 61

A1. 4-μm Contour Map for the Region $-0.7 < \ell \lesssim 32^{O}$ 74
A2. 11-μm Iso-Intensity Map for the Region $-0.7 < \ell < 35^{O}$ 74
A3. 20-μm Map of the Galactic Plane in the Region $-0.7 < \ell < 35^{O}$ 98

B1. 11-μm Map Along the Galactic Plane Between $35^{O} < \ell < 95^{O}$ 135
B2. 20 μm Map of the Galactic Plane in the Region $40^{O} < \ell < 85^{O}$ 135
B3. 27-μm Map of the Galactic Plane in the Region $40^{O} < \ell < 85^{O}$ 136

C1. The 11-μm Contour Map Between 100° and 170° Longitude 138
C2. The 20-μm Contour Map Between 100° and 175° Longitude 138
C3. The 11-μm Map Between 195° and 240° Longitude 139
C4. The 20-μm Map of the Region Between 195° and 240° Longitude Along the Galactic Plane 139

D1. 11-μm Contour Map 169
D2. 20-μm Contour Map 170
D3. 27-μm Contour Map 170

Tables

1. Survey System Parameters Effective Wavelength, Bandwidth, and Instantaneous Field of View 11
2. List of Extended Sources in the Region $0^{O} \lesssim \ell \lesssim 32^{O}$ 40

Tables

3. List of Extended Sources in the Region $35^{\circ} \lesssim \ell \lesssim 95^{\circ}$ 45

4. Extended Sources in the Region $100^{\circ} \lesssim \ell \lesssim 235^{\circ}$ 53

5. List of Extended Sources in the Region $280^{\circ} \lesssim \ell \lesssim 320^{\circ}$ 57

6. Comparison of the Observed Surface Brightnesses with Those Predicted from the Walker-Price Model 65

A1. 4-μm Intensity Grid Over the Region $-0.^{\circ}7 < \ell < 32^{\circ}$ (in units of 10^{-11} W cm^{-2} μm^{-1} sr^{-1}) 75

A2. 11-μm Intensity Grid Over the Region $-0.7 < \ell < 35^{\circ}$ (in units of 10^{-11} W cm^{-2} μm^{-1} sr^{-1}) 82

A3. 20-μm Intensity Grid Over the Region $-0.7 < \ell < 35^{\circ}$ (in units of 10^{-11} W cm^{-2} μm^{-1} sr^{-1}) 90

B1. 11-μm Grid of Intensities Along the Galactic Plane Between 35° and 95° Longitude (units in 10^{-11} W cm^{-2} μm^{-1} sr^{-1}) 100

B2. 20-μm Grid of Intensities Along the Galactic Equator Between 40° and 95° Longitude (units in 10^{-11} W cm^{-2} μm^{-1} sr^{-1}) 113

B3. 27-μm Grid of Intensities Along the Galactic Plane Between 40° and 85° Longitude (units in 10^{-11} W cm^{-2} μm^{-1} sr^{-1}) 125

D1. Grid of 11-μm Intensities Along the Galactic Plane Between $280^{\circ} \leq \ell \leq 320^{\circ}$ (units in 10^{-11} W cm^{-2} μm^{-1} sr^{-1}) 142

D2. Grid of 20-μm Intensities Along the Galactic Plane Between $280^{\circ} \leq \ell \leq 318^{\circ}$ (units in 10^{-11} W cm^{-2} μm^{-1} sr^{-1}) 151

D3. Grid of 27-μm Intensities Along the Galactic Plane Between $280^{\circ} \lesssim \ell \lesssim 318^{\circ}$ (units in 10^{-11} W cm^{-2} μm^{-1} sr^{-1}) 160

An Infrared Survey of the Diffuse Emission Within 5° of the Galactic Plane

1. INTRODUCTION

About 90 percent of the celestial sphere was surveyed to moderate flux levels in broad spectral bands centered at 11 and 19.8 μm on a series of rocket probe borne experiments flown in the early 1970's by the Air Force Geophysics Laboratory (AFGL). Smaller areas were also covered at 4.2 μm (78 percent of the sky) and 27.4 μm (34 percent). Initial results of this survey have been published in catalog form by Walker and Price,[1] Price and Walker,[2] and Price.[3] These source lists were generated from reduction routines which incorporated matched filters designed specifically for the detection and photometry of point sources.

The survey data have been reprocessed by the methods outlined by Price,[4] in order to extract information on extended sources. Preliminary results on the 11 and 20-μm diffuse emission from the galactic plane for the region $\ell < 30^{\circ}$ were presented by Price.[5] In this article, the measurements presented extend the preliminary results to other colors and cover most of the longitude region between $0^{\circ} < \ell < 320^{\circ}$. The general results from these observations are: (1) The in-plane brightness variation with respect to longitude at 4.2, 11, and 19.8 μm is qualitatively similar to that found at 2.4 μm, the far infrared, and for other

(Received for publication 5 June 1980)

Because of the large number of references cited above, they will not be listed here. See References, page 69.

tracers of galactic structure; (2) between $5^{o} < \ell < 30^{o}$ the 4.2 μm emission is relatively smooth and roughly constant with a full width at half maximum of 4 to 5° and in-plane radiance of about 2.0×10^{-10} W cm^{-2} μm^{-1} sr^{-1}; this is consistent with the diffuse 2.4 μm observations and the interpretation that emission at both wavelengths are due to M giants ($T_e \sim 2500^{o}$K); (3) the 11 and 19.8 μm diffuse emission is at least an order of magnitude larger than anticipated either from the 2.4 μm observations or those made in the far infrared; and (4) considerable structure is observed at 11 and 20 μm due to HII regions. The HII regions are measured to be larger than the 3 by 10 arc min beam size and are comparable to the sizes measured at radio frequencies.

2. INSTRUMENTATION

2.1 Telescope–Sensor System

In conducting a rocket-based survey, one notes that the sensitivity, areal coverage, spatial and spectral resolution must be traded off against the constraints imposed by the rocket performance, the data accuracy requirements, and data transmission rate restrictions. The telescope collecting aperture and observation time are limited by size and mass of the hardware which may be flown. The coverage is set by the available observation time and scan rate which is, in turn, a function of the desired sensitivity, the detector width, and telemetry data rate limits.

The survey instruments used for the AFGL infrared survey experiments were of modest size, with apertures of 16.5-cm diameter, and weighing less than 20 kg. The requirements for a fast, compact system with a large, relatively flat, field of view were met by using a four-mirror, folded Gregorian optical design with reimaging. The internal stops and baffles permitted by reimaging and folding the optical path were used to reduce self-emission from the telescope and, along with a baffle and inner radiation shield enclosing the optics, to minimize the side lobe response of the telescope.

Three 8-element, linear, staggered arrays of detectors, each array filtered for a different spectral region, were mounted at the focal plane of the telescope. The schematic layout of the arrays used for the first seven experiments is shown in Figure 1. These arrays used doped germanium detectors with an active area of 10.5 by 3.35 arc minutes (3×10^{-6} sr) and center to center spacing for adjacent elements of 8.8 arc minutes. These arrays were filtered for effective wavelengths of 4.2, 11.0 and 19.8 μm. Doped silicon detectors were employed for the last two flights and the detector widths increased to 5 arc min (4.5×10^{-6} sr field of view); the 4.2 μm color was replaced by one centered at 27.4 μm. The system parameters for the two sets of filter-detector combinations are given in Table 1.

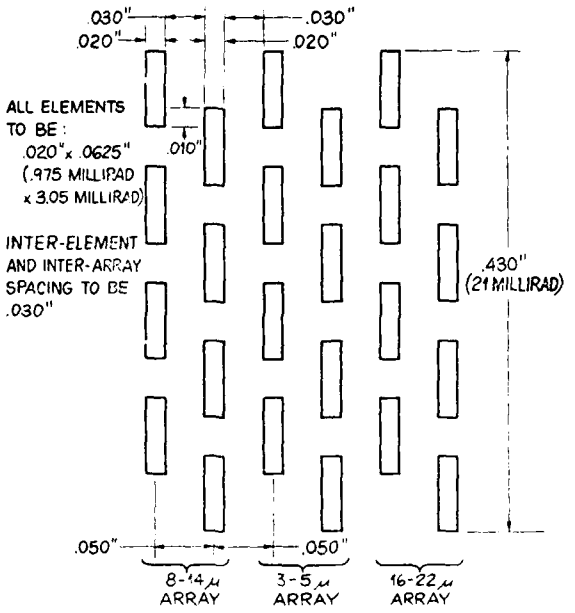

Figure 1. Configuration of the Focal Plane Arrays

Table 1. Survey System Parameters Effective Wavelength, Bandwidth, and Instantaneous Field of View

Color	Northern Experiments λ_e (μm)	Northern Experiments $\Delta\lambda_c$ (μm)	Southern Experiments λ_e (μm)	Southern Experiments $\Delta\lambda_c$ (μm)
4	4.16	1.5		
11	11.00	5.14	11.11	5.67
20	19.80	5.59	19.63	5.99
27			27.43	3.44
Field of View	10.5 by 3.35 arc min 3×10^{-6} sr		10.5 by 5 arc min 4.5×10^{-6} sr	

As seen in Figure 2, the focal plane assembly and optics are conductively cooled from a supercritical helium reservoir. The temperatures of all the optical components, baffles and stops which may be seen by a detector are cold enough to eliminate thermal background as a limiting factor in the detectors performance. The entire system is enclosed in a vacuum housing.

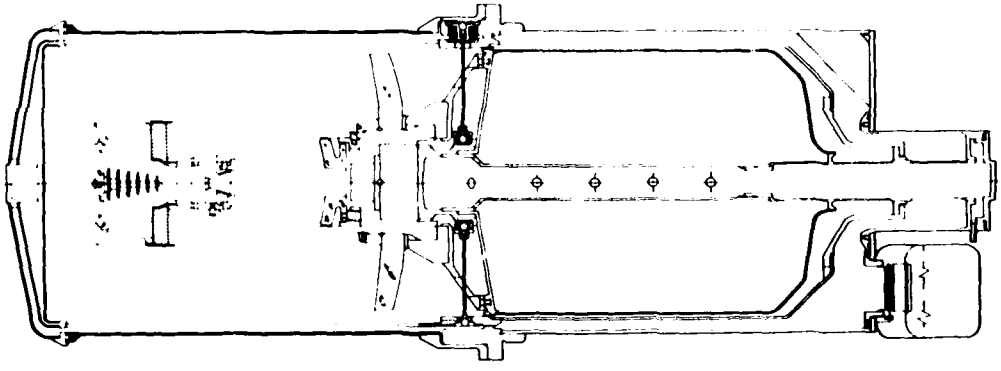

Figure 2. Cross-Section Schematic of the Infrared Survey Telescope

The signal processing electronics amplified and shaped the signal to optimize the signal-to-noise for the design scan rate of 37.5 degrees per second. The detector-preamplifier output was AC coupled to the first stage of amplification in order to eliminate DC drifts and offset problems common to extrinsic photoconductions. A high frequency boost in the first amplifier stage compensated for the $1/f^*$ behavior in detector responsivity due to the coupling of the load resistor and stray capacitance of the preamplifier. Another high-pass filter, placed between the two stages of amplification, reduced scan noise and the 1/f transistor noise from previous components. Finally, the last amplifier stage incorporated a low-pass filter to attenuate noise at the high frequency where there is relatively little signal power.

The resulting over-all detector/preamplifier/amplifier frequency response was relatively flat in the electronic bandpass, falling at the rate of 18 dB per octave at the high frequencies and 12 dB per octave at the low frequencies. The half-power characteristics frequency for the low pass filtering was set at the inverse of twice the dwell time of a point source scanned at 37.5 degrees per second. The half-power frequency of the high-pass filtering was chosen as low as

---

*f frequency

consistent with dynamic range considerations, in order to include as much of the low frequency information as possible from extended sources in the bandpass. The high-pass filter produced ringing in the signal output, the negative portions of which were preserved by biasing the "zero" volt output of the signal processing electronics to a positive value.

2.2 Payload

The rocket payload provided the observing platform for the telescope during the survey. The payload, shown schematically in Figure 3, was divided into four major sections: a sensor housing, a section containing the support instrumentation and telemetry, one for the attitude control system (ACS) and pneumatics, and a recovery section.

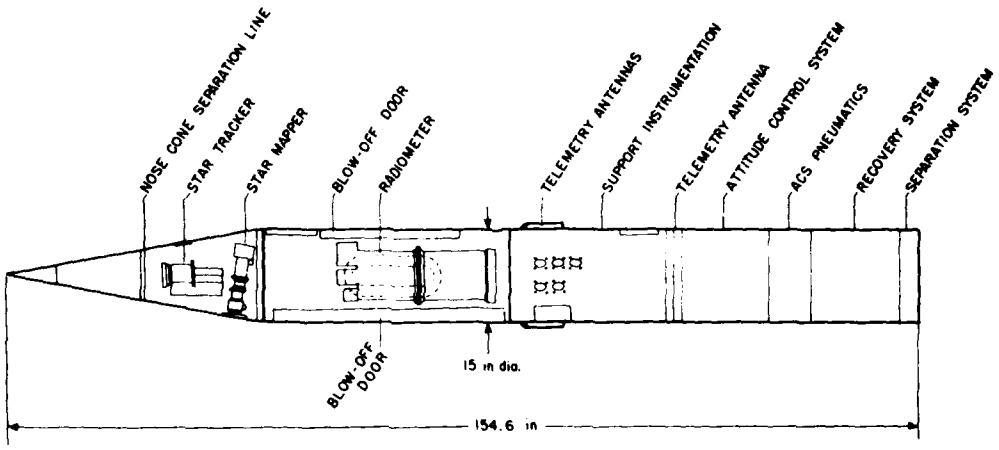

Figure 3. Schematic of the Rocket Payload Used for the Infrared Survey

A rigid, single piece, magnesium alloy casting was used for the telescope housing and aspect platform. This casting provided the stability required to maintain geometric alignment between the star tracker, star mapper, and infrared telescope. The star tracker defined the roll axis of the experiment and actively held this axis fixed in inertial space. Prior to flight, the optical axis of the tracker was accurately coaligned with the geometric longitudinal axis of the payload. The in-flight configuration of the payload was then dynamically balanced to bring the longitudinal principal moment of inertial into near coincidence with the geometrically defined roll axis. The azimuthal reference was defined by a star

mapper, which consisted of a small telescope with a "N" slit focal plane mask and a Fabry field lens to image the objective onto an S-11 photomultiplier tube. Azimuthal information was obtained from the detections of stellar transits across the recticle. The infrared telescope was mounted in a one-axis gimbal with the deployment axis orthogonal to those defined by the star mapper and tracker. Consequently, the deployment plane of the telescope contained the azimuth reference. In this configuration, a payload "alt-azimuth" coordinate was established with the star tracker coaligned to the rotation axes, the star mapper supplying the azimuth reference and the telescope deployment giving the "altitude."

Price et al[6] detail the procedures used to align accurately and calibrate geometrically the three instruments in the payload and the methods used to process the in-flight measurements, in order to obtain the desired arc minute accuracy in pointing knowledge.

The support instrumentation section contained the hardware necessary to run the experiment and transmit the data to the ground. The ACS used a roll stabilized platform with position and rate readouts in the pitch, yaw and roll axes to control the various maneuvers required of the payload during flight. More accurate position and control was obtained in pitch and yaw from the star tracker during the experiment. A nonreactive, cold helium gas pneumatic system was employed for maneuvering.

The payload was designed so that all surfaces exposed during the experiment could be easily cleaned. The volumes which for practical reasons could not be cleaned, for example, the gimbal housing and the sections containing the electronics were sealed and vented through absolute filters during the flight. Also, the clean payload was separated from the rocket sustainer prior to each experiment. Price, Cunniff and Walker[7] describe the problems posed by particulate contamination for a space borne infrared sensor and the procedures used at AFGL to reduce and control this contamination.

3. THE EXPERIMENT

3.1 Experiment Profile

All experiments were conducted essentially in the same manner. The payload was lifted above the atmosphere by a spin stabilized, Nike boosted, liquid fueled

---

6. Price, S.D., Akerstrom, D.S., Cunniff, C.V., Marcotte, L.P., Tandy, P.C., and Walker, R.G. (1978) Aspect Determination for the AFGL Infrared Celestial Survey Experiments, AFGL-TR-78-0253, AD A067 017.

7. Price, S.D., Cunniff, C.V., and Walker, R.G. (1978) Cleanliness Considerations for the AFGL Infrared Celestial Survey Experiments, AFGL-TR-78-0171, AD A060 116.

Aerobee rocket. Shortly after powered flight, the noise cone and the doors to the star mapper and telescope housing were ejected since the residual aerodynamic drag, and centrifugal force from the spin could sweep these items below and away from the vehicle. The vehicle was despun and separated from the rocket motor as soon as the aerodynamic forces were reduced to a level at which the separated payload was stable and controllable by the ACS.

After the ACS captured control of the payload attitude, the longitudinal axis and, consequently, the star tracker's optical axis were maneuvered to a programmed set of inertial coordinates corresponding to the celestial position of a bright star. The stars and launch times were chosen so that the poles of rotation were near local zenith and meridian transit. Once star presence was sensed by the star tracker, control of the pitch and yaw jets was transferred from the position gyroscopes to the tracker. The error signals from the tracker were used by the ACS to null precisely the trackers optical axis, and hence the payload roll axis to the star, maintaining this reference under roll maneuvering throughout the flight.

The infrared telescope was then deployed and the payload spun up about the roll axis to generate the survey scan. The survey scanning geometry is shown in Figure 4. The payload rotates at a roll rate, ω, about a pole of rotation defined by the celestial coordinates, α_1, δ_1, of the star near local zenith (Z) to which the star tracker is locked. The field of view of the telescope swept along a small circle centered on the pole star at a zenith angle (z), set by the telescope deployment. After the completion of each 360° roll maneuver, the sensor was stepped $1^{\circ}.1$, slightly less than the $1^{\circ}.2$ total cross scan field of view of the telescope. Three roll rate changes were programmed to compensate for the secant z distortion inherent in this scanning geometry and to maintain roughly a constant effective linear scan rate throughout the experiment.

The telescope was stowed and capped at the end of the experiment and payload recovered; the equipment was refurbished and flown again. The first seven flights were conducted from the White Sands Missile Range, New Mexico ($32^{\circ}.5$ N. latitude), and the last two from Woomera, Australia (32°S).

3.2 The Survey Data

Each experiment produced several digital data tapes containing the survey data. These tapes were generated in the following manner. The amplifier voltage outputs from each of the 24 detector channels were sampled, multiplexed, and digitized into 10-bit binary words by a pulse code modulation (PCM) encoder. The amplifier gains were designed for a preamplifier limited root-mean-square (RMS) noise value approximately equal to the digitilization level. The resulting dynamic

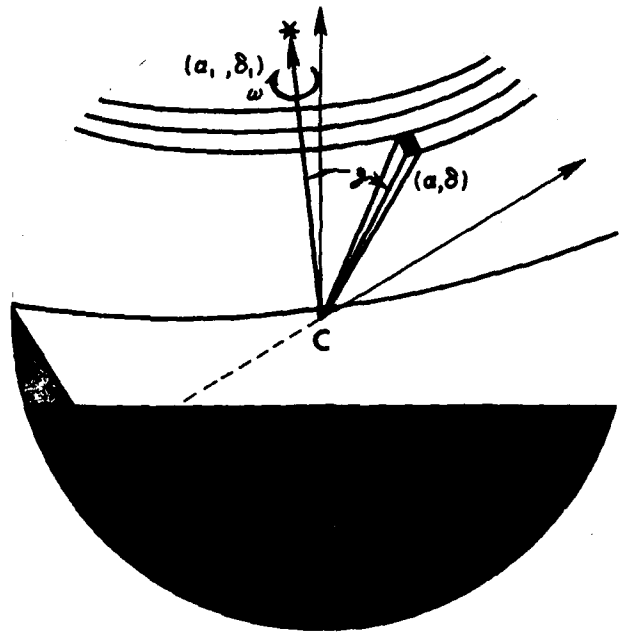

Figure 4. The Survey Scan Geometry. The local zenith is at Z and celestial pole at P. The star tracker is locked to a star near local zenith which has celestial coordinates α_1 and δ_1. The payload is spun at an angular velocity ω with the telescope deployed to various zenith angles, z

range is about 600 as the quiescent levels of the amplifiers were biased to about 40 percent of full scale to preserve the negative signal excursions due to high-pass filtering.

The PCM encoder formatted the data into a serial steam of thirty 10-bit words which included the 24 infrared detector channel outputs, the star mapper data, and diagnostic and status information on the telescope, payload and ACS. The sample rate was high enough to give 4.25 data values during the transit of a point source across a detector. This meant that with the 18 dB per octave low-pass filter in the signal electronics, less than 0.2 percent of the noise power was aliased due to the sampling.

The PCM data were telemetered to the ground during the flight and recorded on a high-speed analog tape along with a locally generated time code. These tapes were subsequently decoded and reformatted into the raw digital data tapes.

Examples of the raw digital data from the first experiment are shown in Figures 5, 6, and 7, demonstrating the diverse nature of the output. Except

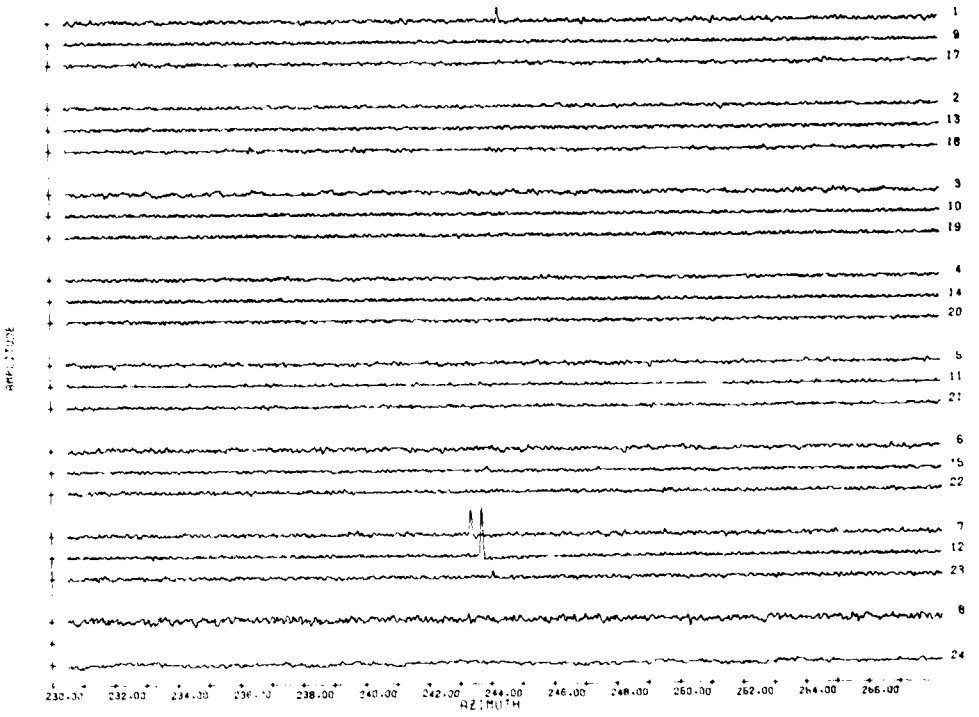

Figure 5. Example of a Point Source Signature. The output of the star RT Vir is shown in the seventh group of detectors in the middle of the figure. Each group of outputs correspond to the three colors in a given row of detectors, the 11 μm channel is at top, 4 μm in the middle and 20 μm at the bottom of the group. The groups are arranged in increasing zenith angle from top to bottom. The 4-μm detector in the eighth row, number 16, was anomalously noisy and is deleted

for number 16, the uncalibrated outputs of the channels are plotted as a function of the azimuth of the center line of the focal plane. The azimuthal offsets of the detector elements in the array produce a staggered signal from a source transit.

The data are ordered into eight groups of three outputs. Each group displays the information from a row of detectors with the top row of the array (smallest zenith angle) at the top of the figure. Further, the outputs are arranged within a group in order of a source transit, the 11-μm channel at top, 4.2 μm in the middle and 19.8 μm at the bottom (see Figure 3). The tick marks on the amplitude axis denote the quiescent, or bias, level of each detector.

A point source signature, due to a stellar transit, appears in the seventh row of detectors in the middle of Figure 5. The star is the semiregular variable

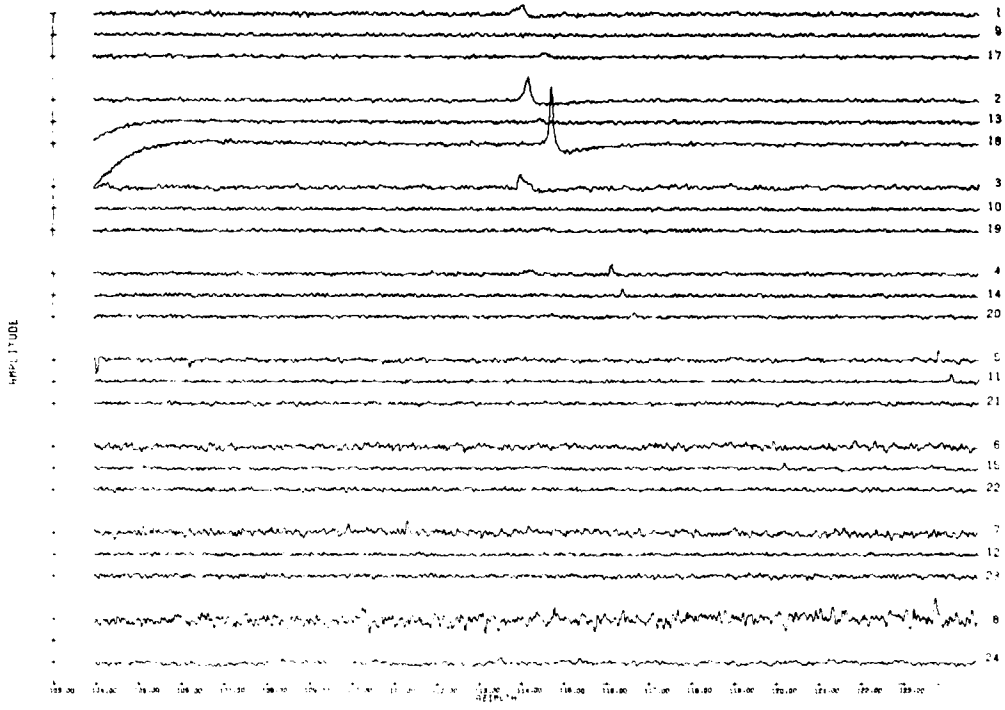

Figure 6. Extended Source Signature. The radio source W40 (Westerhout) is shown in the center of the figure on the top three rows of detectors. The width of the source is evident both in scan and cross scan. Arrangement of the output display is the same as for Figure 5

RT Vir, spectral type M8. Since the relative 11 and 20 μm responses are roughly equal and about five times that at 4 μm, the source is seen to be comparatively warm ($T_c \sim 10^{3o}$K) from the relative signal amplitude in the different colors. The cool extended source W40 (Westerhout)[8] is shown on the top three rows of Figure 6. Here the absence of significant 4.2 μm signal and the relative amplitudes in the 11 and 19.8 μm colors, indicate that this is a cool ($T_c \sim 220^{o}$K) object. The source extends over half the 1.2^{o} cross scan field of the focal plane and the signatures from the individual detectors are noticeably wider than that due to a point source. These factors attest to the significant angular extent of this object.

Figure 7 shows several phenomena. The cold 100 μm source HFE 49 (from the list of Hoffman, Frederick and Emery),[9] is seen on row one. The absence of

8. Westerhout, G. (1958) A Survey of the Continuous Radiation from the Galactic System of a Frequency of 1390 Mc/s, Bull. Astron. Neth. 14:215.

9. Hoffmann, W.F., Frederick, C.L., and Emery, R.J. (1971) 100-Micron Survey of the Galactic Plane, Astrophys. J. (Letters) 170:L89.

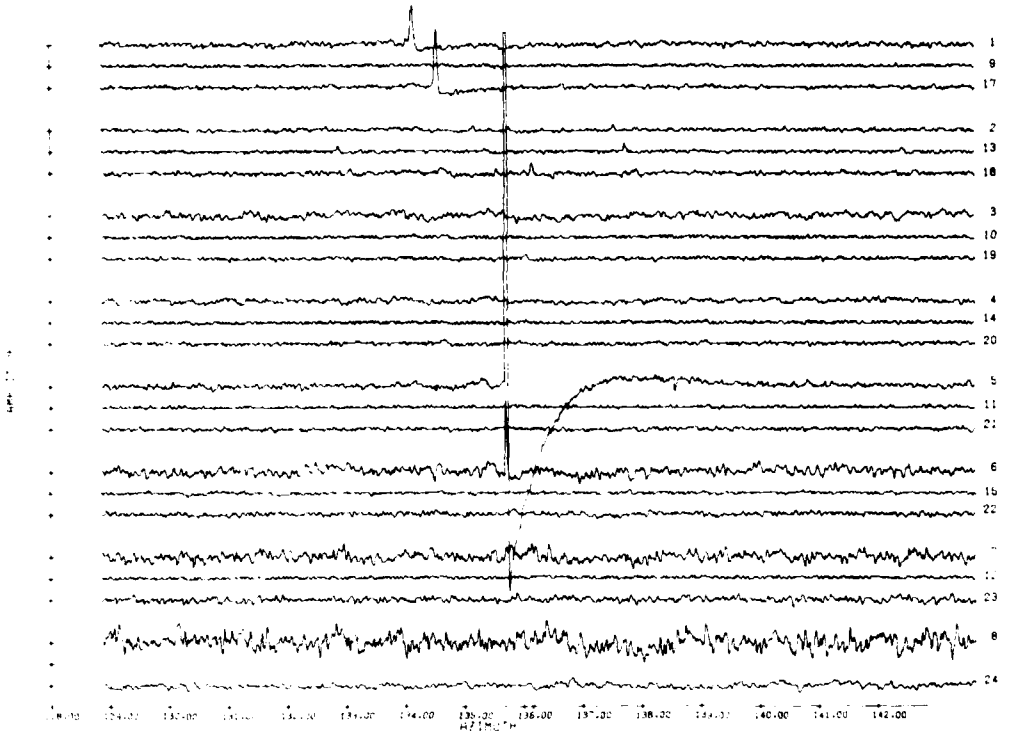

Figure 7. Impulse Response. An impulse response of the system due to a cosmic ray is seen on channel 5 with the attendant crosstalk on channel six. Source number 49 of Hoffmann, Frederick and Emery appears on channels 1 and 17. The crossing of the galactic plane is centered on the figure

4.2-μm emission and the relative 11 and 19.8-μm amplitudes again indicate the low temperature of the source, and the signature width reveals the source to be extended with respect to the 3.35 arc min in scan extent to the detector. Barely visible on the 11-μm channels (numbers 1 to 8) is the emission from the galactic plane which may be seen as a wide ($\sim 1^{0}$) positive excursion whose peak runs diagonally across the figure from an azimuth of about 134.5^{0} for channel 1 to about 136.5^{0} for channel 8. Tracking the peak is the broad, shallow negative signal produced by the high-pass filtering of the electronics. The large pulse in the center of Figure 7 is due to a cosmic ray event to which the detector crystals were sensitive. The energy deposition into the detector element by the event is so fast that it may be considered as a delta function with the resulting signature characteristic of the impulse response of the system. This pulse is significantly shorter and with a

faster rise time than that due to a point source transit. The negative signal excursion due to the high-pass filter is clearly evident, amounting to about 8 to 12 percent of the peak value. The concurrent pulse in row 6 is due to electronic cross talk which was typically about 5 percent between adjacent channels.

These figures are ordered in time during the experiment. A general increase in noise level is evident in Figure 7 as compared to Figures 5 and 6. As the experiment progressed, the telescope was stepped closer to the horizon of the earth, which resulted in an increasing detector background from the earth shine through the side lobe response of the optical system. The noise varies as the square root of the increase in this background, producing a time, or more accurately deployment, dependence in the noise level.

On the nine flights, over 100,000 square degrees of sky was scanned. For eight of these experiments, the galactic plane was crossed twice per roll and these crossings were processed for measurement of the diffuse infrared emission. Over 8,000 scans were examined; of these, the data from one experiment was dominated by extraneous factors, appearing as correlated noise; these measurements were deleted from further consideration. The remaining scans covered over three quarters of the galactic plane; these data are presented in this report.

4. DATA REDUCTION

The experiments were designed to maintain approximately the same constant effective linear scan rate on all rolls for all flights. Consequently, with the survey geometry, the transit time across a latitude band centered on the galactic equator will be a function of the galactic latitude of the pole star and, to a smaller degree, the deployment angle of the telescope. The minimum transit time across the galactic plane would be produced by a pole star in the plane. This situation results in the highest spatial frequencies due to the diffuse emission from the plane and minimum attenuation of the signal by the high-pass filter. Such is the case in Figure 8, which depicts the uncalibrated outputs of the eight 11-μm channels as they were scanned across the galactic plane at a longitude of about 30° with α Lyr, $b \simeq 19^{\circ}$, for the pole star. The broad signal centered on the plane is quite evident. On the other hand, the transit time across the plane in Figure 7 was about twice as long and suffered over twice the attenuation than shown in the data in Figure 8. Thus, it is evident that the extended source information is in the data, and remains to be extracted by adequately compensating for the attenuation due to the high-pass filter.

Extensive use of Fourier, Laplace and z-transforms and their application to signal processing is made in the following description of the data processing

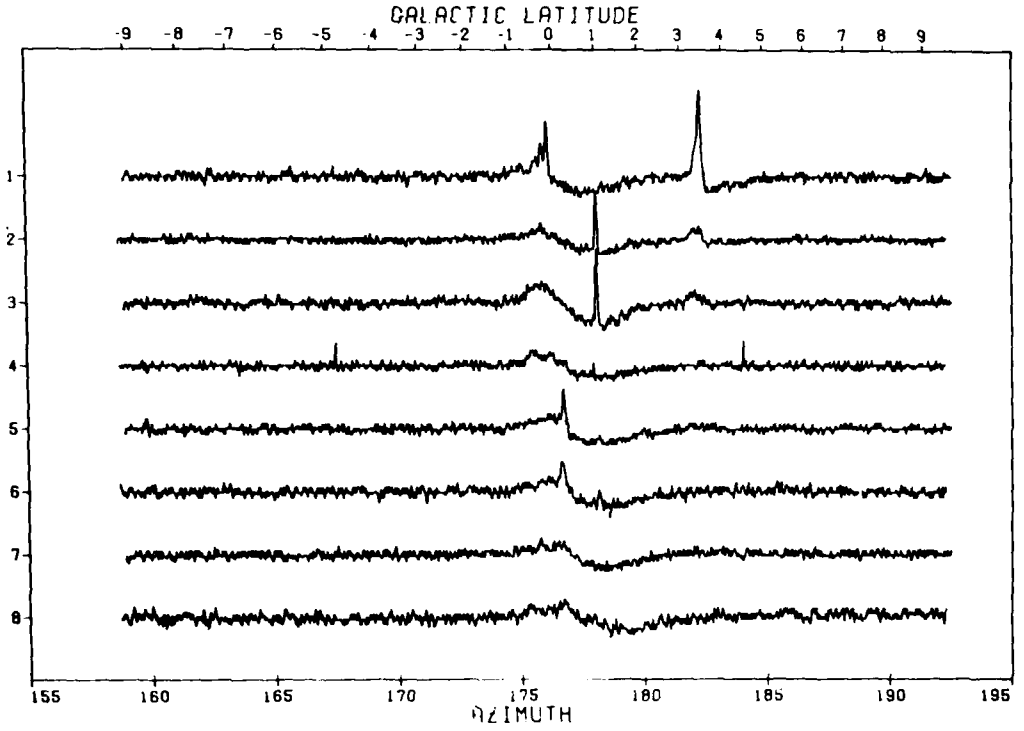

Figure 8. Uncompensated Output for a Galactic Plane Crossing. The longitude of the depicted region is about 30°, AB Aql is the peak at b ~ 0° on channel one; W40 (Westerhout) is detected on channels 1 through 3 at b ~ 3°.5

techniques used to extract the extended source signals. Bracewell[10] gives a good general discussion of these transforms, their interrelations and the application of the Laplace transforms to electrical circuits. An excellent presentation of z-transforms and their applicability to filter design and signal processing may be found in Oppenheim and Schafer.[11]

The detector-preamplifier channel electronics described in Section 2 produces an output voltage, $V_o(t)$, due to a time varying irradiance, W(t), caused by the sensor scan and modified by the system transfer function. Mathematically, $V_o(t)$ and W(t) are related through the system transfer function by

---

10. Bracewell, R. (1965) The Fourier Transform and Its Application, McGraw-Hill, Inc., New York.

11. Oppenheim, A.V., and Schafer, R.W. (1975) Digital Signal Processing, Prentice Hall, Inc., Englewood Cliffs, N.J.

$$V_o(t) = L^{-1}\left[L(W(t))R_v \frac{s^2}{(s+\omega_1)(s+\omega_2)} \frac{\omega_3^2\,\omega_4\,G}{(s+\omega_3)^2(s+\omega_4)}\right] \quad (1)$$

where L. and $L.^{-1}$ are the direct and inverse Laplace transforms; R_v the detector responsivity measured across the load resistor; s is the complex Laplacian frequency variable and the ω_i's the characteristic angular frequencies of the various filter stages. The filters were resistor-capacitor networks which have an $\omega_i = 1/RC = 2\pi f_c$ with resistor, R, capacitor, C, and a half power (3 dB) frequency, f_c, in hertz; G is the total system gain.

The transfer function in Eq. (1) assumes that the 1/f variation in detector response is exactly compensated by the high frequency gain in the first amplification stage. The first term in the transfer function, $s^2/(s+\omega_1)(s+\omega_2)$, arises from the 12 dB per octave high pass filter (second order zero). The last term, $\omega_3^2\,\omega_4\,(s+\omega_3)^2(s+\omega_4)$, is the 18 dB per octave low-pass filter (third order pole).

Compensating for the high-pass filtering is straightforward. The Laplace transform of the output voltage is divided by the high-pass filter terms. Specifically

$$H(s) = \frac{s^2}{(s+\omega_1)(s+\omega_2)} \quad (2)$$

The inverse of H(s) is defined as

$$H^{-1}(s) \quad \frac{(s+\omega_1)(s+\omega_2)}{s^2} \quad (3a)$$

The magnitude response of this inverse filter function is given in the Fourier domain as

$$|H^{-1}(f)| \quad \frac{[(f^2+f_1^2)(f^2+f_2^2)]^{1/2}}{f^2} \quad (3b)$$

Now, multiplying both sides of the Laplace transform of Eq. (1) by the inverse high-pass filter given in Eq. (3a), one gets

$$H^{-1}(s)L(V_o(t)) \quad L[W(t)R_v] \quad \frac{\omega_3^2\,\omega_4\,G}{(s+\omega_3)(s+\omega_4)} \quad (4)$$

Unfortunately, $V_o(t)$ is not analytic and the evaluation of its Laplace transform is cumbersome. Further, the data are not continuous but sampled and digitized. Thus, a digital equivalent to the operation in Eq. (4) is needed.

The one-sided z-transform, V(z), of a sequence $\{v_n\}$ is defined by a polynomial in the complex variable z as

$$V(z) = \sum_{n=o}^{\infty} v_n z^{-n}$$

where v(n) is the sampled sequence of output voltages which begins at n = o. The digital equivalent of the inverse filter in Eq. (3a) is obtained from the bilinear transformation which applies the substitution

$$S = \frac{2}{T} \frac{1 - z^{-1}}{1 + z^{-1}} \qquad T = \text{sample interval time}$$

and distorts the analog angular frequency, ω_a by

$$\Omega_d = 2 \tan^{-1} \frac{\omega_a T}{2}$$

The bilinear transformation was used in preference to others as it is free from aliasing and produces a stable digital filter from a stable analog equivalent.

With these substitutions, the digital equivalent to Eq. (3a) is

$$H_d^{-1}(z) = g \frac{(1 - \alpha z^{-1})(1 - \beta z^{-1})}{(1 - z^{-1})^2} \tag{5}$$

$$g \quad \text{gain} \quad \frac{(2 + \Omega_1)(2 + \Omega_2)}{4}$$

$$\alpha \quad \frac{2 - \Omega_1}{2 + \Omega_1} \quad ; \quad \beta \quad \frac{2 - \Omega_2}{2 + \Omega_2}$$

The digital equivalent to Eq. (4) is

$$H_d^{-1}(z)V(z) = W(z)R_v \frac{G'(1 + z^{-1})^3}{(1 - \gamma z^{-1})^2(1 - \varepsilon z^{-1})} \tag{6a}$$

$$= g \frac{(1 - \alpha z^{-1})(1 - \beta z^{-1})}{(1 - z^{-1})^2} \sum_{n=o}^{\infty} v_n z^{-n} \tag{6b}$$

where W(z) is the discrete, sampled values of the radiance.

Applying the inverse filter, $H_d^{-1}(z)$, to the raw output, one notes that this produces the discrete time sequence of the background irradiance modified by the low pass electronic filter. Thus, at least mathematically, the low frequency content of the background is restored. Practically, there are inherent difficulties in using the inverse filter.

As may be seen from Eq. (3b), the inverse filter has infinite gain at zero hertz and restoration at this frequency produces an indeterminate result. Consequently, the constant or DC component of the background is permanently lost. Further, the very large gain of the inverse filter at low frequencies will considerably enhance the 1/f detector and electronic noise, creating problems in the stability of restoring long sections of data and making the signal-to-noise of the observation a function of frequency content of the raw signal as well as intensity of the source. Another way of interpreting this is that scanning a given area of the galactic plane with an experiment which has a pole star in the plane produces a better quality restoration than a pole star of high galactic latitude. Further, the stability difficulties are solved by limiting the restoration to only those sections of data containing the source of interest, such as the galactic plane, and adopting a value of the DC or background level external to the boundaries assumed for the source. Departures of the data from the assumed constant background are then taken as baseline variations which are to be corrected.

The digital filtering in Eq. (6b) may also be expressed as a recursive relation

$$y_n = g\,(v_n - (\alpha + \beta)v_{n-1} + \alpha\beta v_{n-2}) + 2\,y_{n-1} - y_{n-2} \tag{7}$$

with $\{y_n\}$ as the output sequence. In this case the z-transform has advantage over the discrete fast Fourier transform in that the data manipulation is more compact, as it depends only on two previous output values and a weighted second difference of the input; this is a simple operation with limited storage requirements and no assumption of periodicity.

The values of α and β were determined by a systems identification analysis on selected sections of the data. Initial estimates of α and β were obtained from the circuit components and used to rectify a signal by means of Eq. (7), with the result being compared to a model. Alpha and β were iteratively adjusted by the method of steepest descent until the sum square difference between the rectified signal and model was minimized. Correct values of α and β would produce an output for a rectified impulse which returned to zero level, with no ringing, after an interval specified by the time constants of the low-pass filter. The adopted model was, thus, a zero level after a specified time from the beginning of the pulse. The rectified pulses consisted of a number of cosmic ray impulses plus a few large amplitude stellar signals. Simultaneous sum square minima were required between all the pulses and the model.

The next problem in the low frequency restoration was presented by the initial conditions. To illustrate, Figures 9, 10, and 11 show the raw and rectified output for two 11-μm and one 20-μm channels, respectively, as they scanned roughly along the galactic plane. While the reference, or zero level of the restored data in Figures 9b and 10b are reasonable and stable, that in Figure 11b is obviously not. The undulating baseline in Figure 11b is due, in part, to the low frequency noise and to errors in assuming that the initial values of the data are zero. An error either in the assumed bias level of the input data or the input and output values previous to the first data point will result in a parabolic deviation of the baseline due to the double integration in Eq. (7).

These trends and the low-frequency noise may be handled if it is assumed that the extended source of interest is entirely contained in the restored data segment and the unwanted variations represent baseline drifts of reasonably low order polynomial trends. In this case, differencing the rectified data produces an output that averages to zero for the source of interest and a constant indicative of the linear trend in the baseline. Account of higher order trends is obtained by averaging the second, third or higher differences. For the galactic plane crossings, a third order polynomial was found to fit the majority of the baselines. Specifically, corrected second differences of the rectified signal were derived by integrating the third differences minus their average. An average of the twice differenced data was found, subtracted from these data and the result numerically integrated to produce a corrected single differenced output. The corrected single differenced values are, in turn, averaged, the average subtracted, and the result integrated. The final constant of integration is taken as the average of the values external to the source limits.

In general, the extent of the galactic plane was taken to be $\pm 5^{\circ}$ latitude for the 4.2-μm channels and $\pm 3^{\circ}$ for the 11, 19.8 and 27.4 μm outputs in fitting the baseline. The 11 and 19.8-μm limits in the Cygnus X complex of emission regions

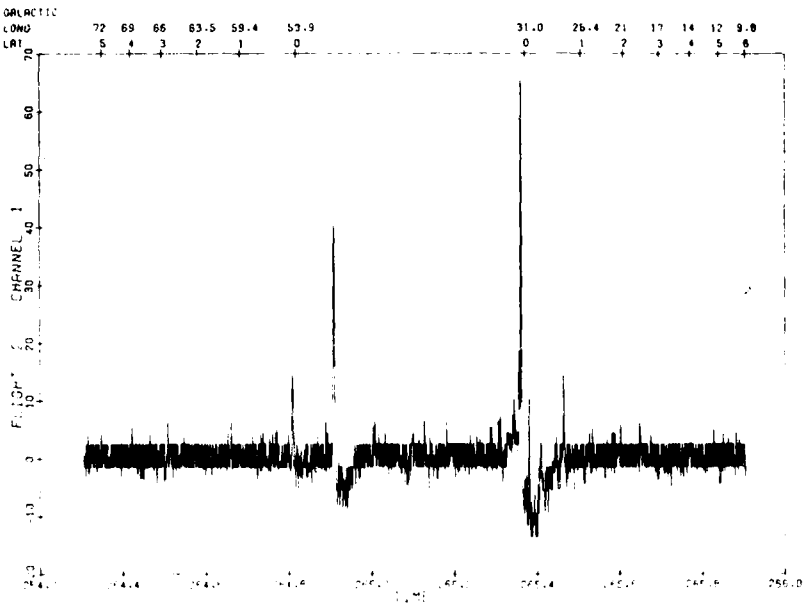

Figure 9a. Uncompensated 11-μm data for an 11-μm Scan Along the Galactic Plane

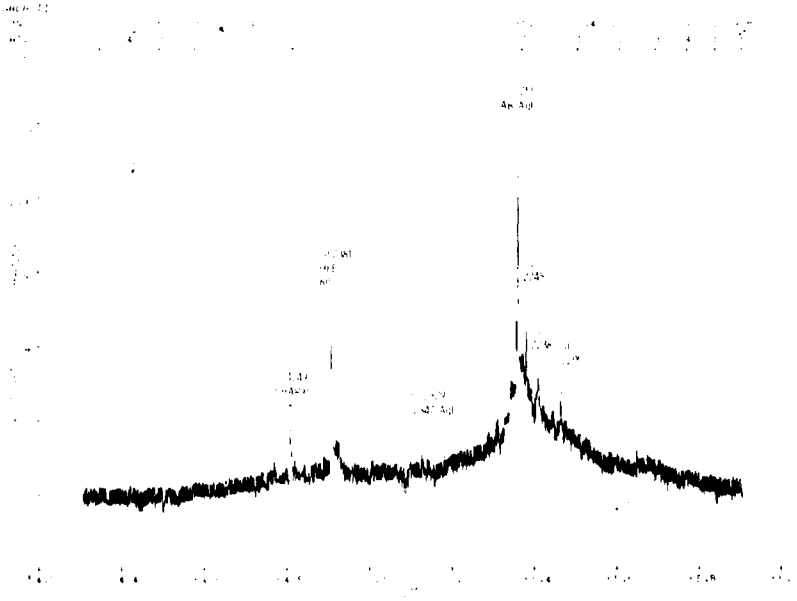

Figure 9b. Rectified Output for the Data in Figure 9a. Baseline corrections have not been made

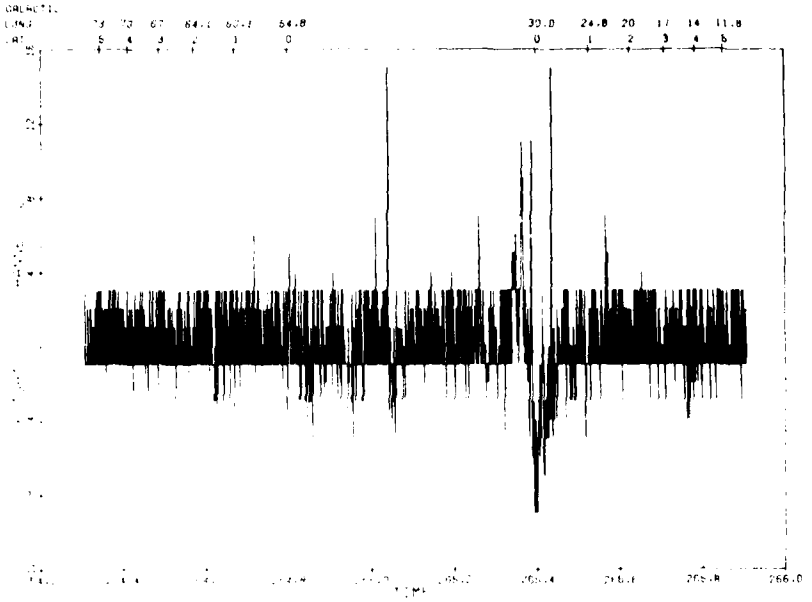

Figure 10a. Uncompensated Data for the 11-μm Channel Adjacent to that in Figure 9a

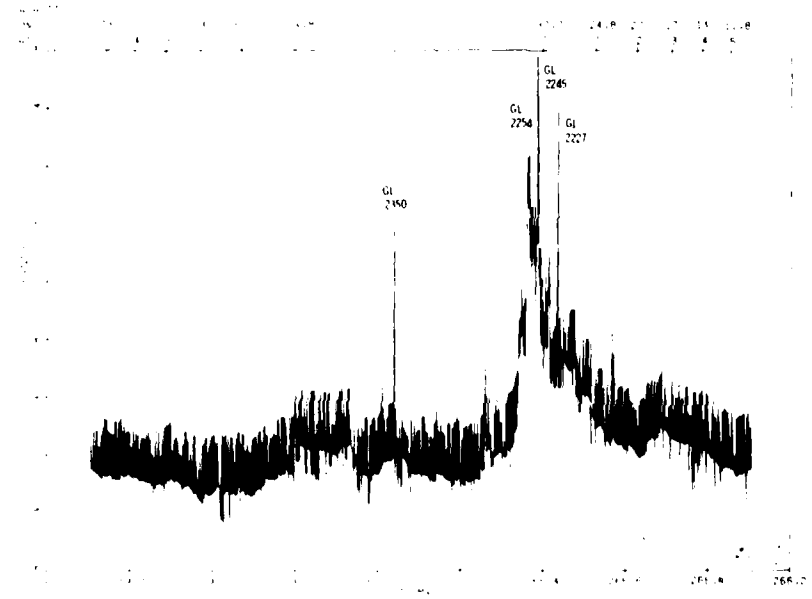

Figure 10b. Rectified Output from the Data in Figure 10a. Baseline corrections have not been made

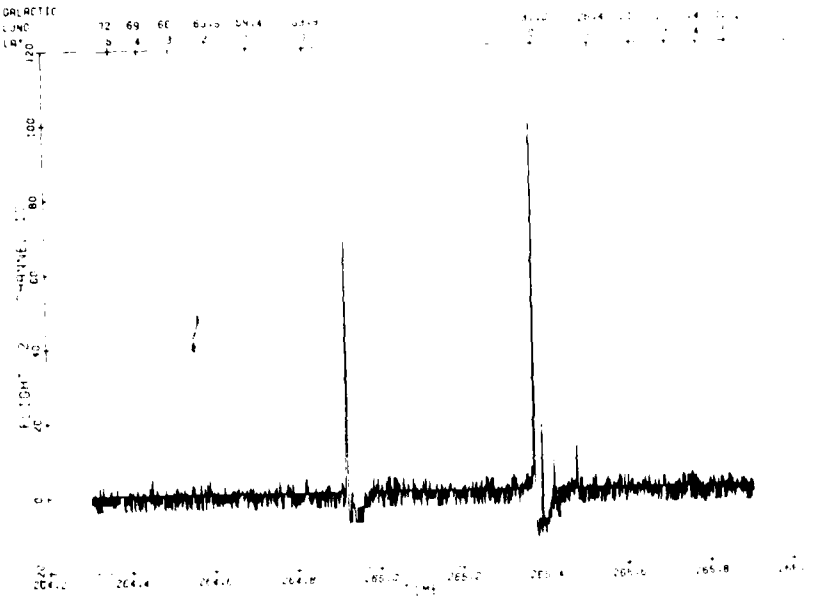

Figure 11a. Uncompensated 20-μm Output for a Scan Along the Galactic Plane

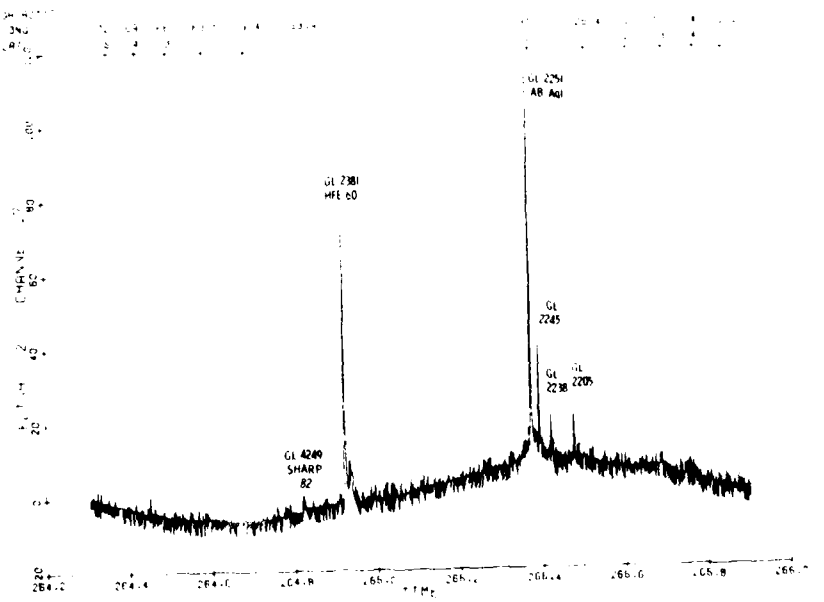

Figure 11b. Rectified Output from Data in Figure 11a. Baseline corrections have not been made

were extended to -4°, $+5^{\circ}$ latitude. The restored scans were examined after baseline corrections and all channels with uncompensated signal saturation, telemetry dropouts, and associated nonlinear effects in the raw data stream eliminated from further consideration.

Another baseline fitting was done in an attempt to eliminate possible higher order variations. An initial baseline consisting of the data outside the source limits and a linear interpolation interior to the limit values is assumed. The Fourier transform of these values are apodized with a Blackman windowing function[11] and the inverse transform of the result taken as the updated baseline. The original data external to the source limits are substituted into the updated baseline and the result transformed, apodized, and the inverse taken. This procedure is repeated until the sum square difference between the updated baseline and the original value outside the source limits fall within a goodness of fit criterion. The baseline interior to the source limits should be driven to assume the same trends and frequency characteristics of the values outside these limits by this procedure.

The baseline trends are necessarily of fairly low frequency compared to the source signal in order for them to be separated from the source. Consequently, the actual baseline determination was performed on rectified data which were decimated after being smoothed with a moving average filter. The differencing interval for the first baseline fit was taken to be roughly the half-width of the source signal. The final baseline was interpolated to the original sampling frequency, then subtracted from the rectified data in order to establish the zero reference level. An example of rectified scans after baseline corrections is given in Figure 12 which shows the data taken from Figure 8 after restoration with the recursive operation of Eq. (7) and the baseline corrections.

The next step is to apply the photometric calibration to the restored data. The calibration of the survey photometry on each detector has been described in detail by Price and Walker.[12] The salient points from this article are: (1) The stars observed during the survey were the primary calibration sources; (2) the instruments were remarkably stable under different background conditions and over a two-year period; and (3) the relative responses of the detectors in a color band from extended phenomena were in good agreement with the relative values obtained from the point sources.

The point source amplitudes used in the calibration were obtained from a cross correlation with a model pulse and were equivalent to the peak-to-peak value of the source signature. Numerically, these values are the same as the zero to peak amplitudes for rectified signals, which implies that the stellar calibrations

---

12. Price, S.D., and Walker, R.G. (1978) Calibration of the HiStar Sensors, AFGL-TR-78-0172, AD A061 020.

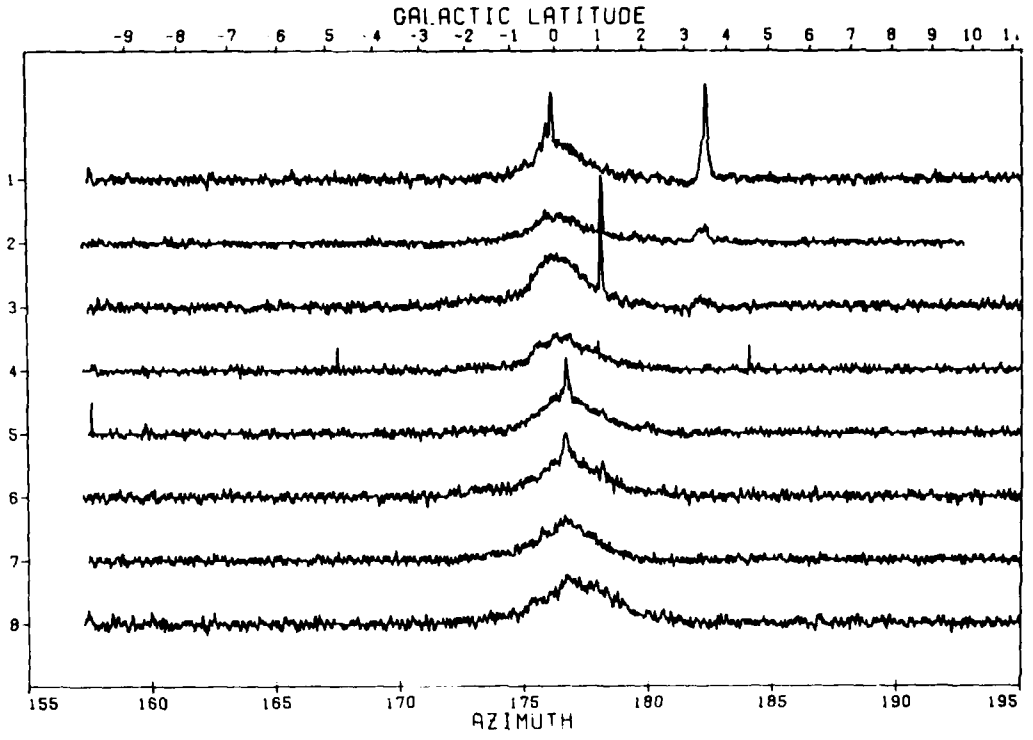

Figure 12. Rectified 11 μm Scans Across the Galactic Plane. The data from Figure 8 has been rectified and baseline trends subtracted

are applicable to the extended source data. The relative calibration obtained by Price and Walker[12] from rectified extended source measurements, scale to within a maximum difference of 25 to 30 percent of the stellar calibration. Since point source response varied over the surface of a detector, the relative responses obtained from the extended sources were adopted. The relative values were averaged in each color then scaled to 0.85 of the average in each respective color obtained from the calibration using the stars. This scale factor is the size of the discrepancy found between the survey magnitudes and those measured from the ground on reasonably stable stars. Price and Walker,[12] Gehrz et al[13] and Rudy, Gosnell and Willner[14] found that in general the AFGL magnitudes were 0.1 and 0.2 magnitudes brighter than measured from the ground. The relative calibration

13. Gehrz, R.D., Hackwell, J.A., and Grasdalen, G.L. (1979) Infrared Studies of AFGL Sources, AFGL-TR-79-0274, AD A084 713.

14. Rudy, R.J., Gosnell, T.R., and Wilner, S.P. (1979) Ground Based Measurements of Sources in the AFGL Infrared Sky Survey, AFGL-TR-79-0172, AD A081 381.

derived from extended source measurements exhibited an internal consistency of 10 to 15 percent, whereas the scatter in the survey stellar measurements was found to be 30 to 50 percent by Price and Walker.[12]

The extrinsic photoconductive detectors used for these experiments are subject to a variety of nonlinear effects associated with high background photon flux. Sayre et al[15] observed a marked variation in spectral responsivity for a Si:As detector operated under a high background by masking the photosensitive area with apertures of various areas and geometry. Arrington and Eisenmann[16, 17] found a background dependence for the responsivities of the focal plane arrays used on the southern hemisphere experiments. Also, dielectric relaxation effects can produce an enhancement of low frequency response.* The photon background incident on the detectors appears to be the dominant influence on all these effects.

These nonlinearities are incorporated in the over-all calibration errors. The effects of geometry of the detector illumination should be negligible as all the focal planes used had an aperture mask over the detectors, which shaded the contacts. If the efforts noted by Sayre et al[15] apply to these focal planes, then source geometry would have small secondary effects compared to that due to shading the contacts. The Sayre et al results were obtained under very high illumination, several orders of magnitude above that seen by the survey detectors even under the worst earthshine conditions; it is unclear that geometry effects are as important under the lower background conditions.

Dielectric relaxation and responsivity changes were found not to be significant. Price and Walker[12] found that not only was the survey calibration stable over a two-year period (the first six experiments used the same telescope system) but responsivity variations of no larger than 10 percent were observed for changes of as much as 10^3 in detector background. Further, the relative calibration obtained from sources with a range of spectral frequency distributions that illuminated the full field of the detector was found to scale within 20 percent of that obtained from

---

15. Sayre, C., Arrington, C.D., Eisenmann, W.L., and Merriam, J. (1976) Characteristics of Detectors Having Partially Illuminated Sensitive Areas, preprint from IRIS March, 1976, meeting on Detectors.

16. Arrington, D.C., and Eisenmann, W.L. (1973) Test Data for a 24-Element Array, Naval Electronics Laboratory Center, Report 2600-5.

17. Arrington, D.C., and Eisenmann, W.L. (1974) Test Data for a 24-Element Array, Naval Electronics Laboratory Center, Report 2610-17.

*NASA Ames Contract Reports CR-152, 014; CR-152, 941.

the stars. These extended sources were: (1) a series of pulses from an internal stimulator during the three roll rate changes; each pulse in the series lasted about 20 msec; (2) the amplitude of the rectified signal from the shock front of the re-entering sustainer, the width at the half intensity point varied from 25 msec to as long as one second; and (3) the detector noise measured as a function of background, with a duration of seconds. Except for the noise measurements, the source functions for these measurements are unknown and only a relative calibration could be done. However, the relative agreement using four different sources imply that no large variations exist due to background or dielectric relaxation in the data.

In part, this agreement may be due to the fact that for a given background, the systems identification will explicitly take into account the low frequency response characteristics of the detectors. Finally, it is noteworthy that no systematic differences were found in the restored scans taken with different sensor systems under widely different background conditions and frequency content of the measurement for overlapping experiments. The observations obtained on the overlapping sections of the galactic plane agree with each other to within the calibration uncertainties and the signal-to-noise of the restored signal. Also, as will be shown, the 4-μm observations are entirely in accord with independent experiments at 2.4 μm.

A conservative estimate is that the absolute intensities, including noise, are accurate to within a factor of 2. The relative uncertainty, that is color to color, should be somewhat better, about 30 percent in the 4- to 11-μm ratios and about 50 percent for ratios involving 20 and 27 μm values.

Significant scan to scan to scan correlation should exist since the emission from the galactic plane extends over a large angle. Accounting for this correlation with some form of two-dimensional smoothing should reduce the relative calibration errors in addition to the errors in baseline corrections and low frequency noise. All these effects should appear with relatively high frequency in the cross scan directions.

After low frequency restoration, baseline correction and calibration, the data was filtered by the nonlinear smoothing technique described by Rempel.[18] This method calculates a smoothed output by means of an iterated weighted least-squares parabolic fit over the n data points on either side of the value being filtered. The fit is iterated by adjusting the weights of each of the 2n + 1 data values according to their deviations from the previous solution.

---

18. Rempel, G.G. (1974) Non-linear (Parabolic) Smoothing of Experimental Data, Translation from Izv. Earth Sciences, No. 3, 101.

An initial fit is determined for the 2n + 1 data points with a least-squares parabola, P_0, which equally weights the values. The square deviations from this fit are calculated over the fitting interval, that is, for the kth point in the interval

$$d_k = |y(i + k) - P(i + k)|^2 \quad ; \quad -n \leq k \leq n$$

These values are used to generate a set of weights by

$$w_k = \frac{\max(d_k) - d_k}{(2n + 1) \max(d_k) - \sum_{k=-n}^{+n} d_k}$$

These weights are used to determine a second least-squares parabola, P_1. This curve fit leads to, in turn, a new set of deviations, then weights which are used to calculate a third least-squares parabola, P_2. The value of this third parabola at the midpoint is adopted as the smoothed i^{th} output value. The smoothing interval is advanced one data point and the iterated curve fitting procedure generates the (i + 1) smoothed value. This process continues until the entire segment has been smoothed.

As may be seen from the calculation of the weights, small deviations produce large weights and vice versa. Indeed, zero weight is assigned to the value with largest deviation. Therefore, the points which best fit the parabolic curve will dominate the least squares solution after a few iterations even with several discordant values in the interval. The algorithm very strongly attenuates rapid variations in the data, virtually eliminating changes of one fifth, or less, the length of the smoothing interval upon two successive applications of the nonlinear filter (Rempel[19]).

The iterated, nonlinear, regressive filter was used initially to smooth the restored output of each channel independently of the others. The basic coordinate for this operation was rocket azimuth at constant zenith angle, which is unique for each experiment. This smoothing has the advantage of being self-consistent in that calibration uncertainty and baseline error is unimportant, and the result is independent from that obtained on other channels. A 50-sample smoothing interval, which corresponds to a scan angle of $0^{\circ}.7$ in azimuth, was selected since it is the minimum length required essentially to eliminate point source signatures and impulse responses from the data. The output of the first smoothing is decimated by about a factor of 4 and ordered in galactic latitude by taking results in increments of $0^{\circ}.05$ (3 arc min) in galactic latitude between $+5^{\circ}$ and -5°.

Best results were obtained for the diffuse emission associated with the galactic plane by combining data from overlapping experiments at this stage and smoothing in longitude at constant latitude rather than smoothing individual experiments in terms of their respective zenith angles before combining the data. Combining data from overlapping experiments before cross scan smoothing tended to average systematic trends due to relative calibration errors and to fill in the blank coverage left when scans were eliminated due to nonlinear effects. A $1.^{\circ}3$ interval was needed for cross scan smoothing in order to incorporate all of the eight outputs in the cross scan direction of the focal plane array. There is a significant change in the diffuse emission from the galactic plane over an interval this size in rocket zenith for those experiments with pole star far from the plane. In this case, the smoothing would attenuate the signal of interest.

Thus, after the initial channel by channel filtering, all the values at a specific latitude were ordered by longitude and double smoothed by the nonlinear parabolic weighted region over a longitude interval of $1.^{\circ}3$. The filtered output is taken at specific longitudes spaced $0.^{\circ}05$ (3 arc min) apart. The end product is a smoothed grid of intensities spaced every $0.^{\circ}05$ in galactic latitude and longitude limited to the region $|b| \leq 5^{\circ}$.

These intensity grids have the highest resolution consistent with the objective to eliminate point sources and to account for systematic trend in the cross scan direction. The resolution is about two thirds the length of a smoothing interval or about $0.^{\circ}8$ latitude and $0.^{\circ}8$ in longitude. The test cases presented for one dimensional arrays by Rempel[12] show that one-sided signals, a fifth the smoothing interval, are virtually eliminated upon two successive applications of the nonlinear filter. Signals a third the width of the interval are passed at about 80 percent the original amplitude and with 40 percent increase in the width at half intensity. An examination of the grids of intensities and extended source list corroborate this estimate of the resolution. The smallest sources in the lists, and minimum separation between sources, are found to be $0.^{\circ}8$ in latitude and $0.^{\circ}8$ in longitude.

Although the diffuse emission from the galactic plane is evident from the [illegible], the color is not large enough to filter the [illegible] stars. [illegible] during [illegible]. [illegible] the [illegible]. The [illegible] to [illegible] the [illegible] [illegible] the [illegible] [illegible] [illegible]

5. RESULTS

Three-quarters of the galactic plane were covered at 11 and 20 μm and lesser areas were surveyed at 4 and 27 μm. Most of these regions were scanned on at least two different experiments. The following discussion of the general character of the observed emission is sectioned into four latitude regions which correspond to groups of overlapping experiments.

All the contour maps presented in this section, and in the Appendices, have the same intensity scale for a given color. The lowest level in each color was selected to show some effects of the noise.

The brighter contour levels were chosen empirically to emphasize the general emission from the galactic plane without swamping the plots with detail. In units of 10^{-11} W cm^{-2} μm^{-1} sr^{-1}, the 4-μm lowest contour is at 5, and each succeeding level is an increase of 5 (5, 10, 15 ...); at 11 μm, 1 is the lowest value, and each brighter level is an increase of 2 beginning at 2 (1, 2, 4, 6 ...), the 20-μm scale is half that at 11 μm (0.5, 1, 2, 3 ...) and, finally, the 27-μm lowest, and outermost, contour is set at 2.5 with successive levels being an increase of 5 beginning at 5 (2.5, 5, 10, 15 ...).

5.1 Longitudes 0° to 35°

The two flights covering this region produced measurements in the 4, 11, and 20-μm spectral bands from the galactic center to the area around AB Aql at $\ell \sim 30^{\circ}$. The data from the first experiment were of lower quality than the second, as the pole star was at a much higher galactic latitude, α CrB at $b \sim 53^{\circ}.75$ as compared to $b \sim 19^{\circ}.25$ for α Lyr. This may be qualitatively seen by comparing the 11-μm scans across AB Aql for the α CrB experiment (Figures 9 and 10) to those from the α Lyr flight for the same area in Figure 8 for the raw data and Figure 12 for the restored observations.

The sensitivity at 4 μm was about a factor of 4 less than that at the longer wavelengths. Consequently, the α Lyr flight produced the only usable 4-μm measurements through a fortunate combination of crossing the galactic plane in the region of highest emission almost perpendicularly, resulting in the minimum of electronic attenuation. Three quarters of the 20-μm array malfunctioned on the second flight so most of the observations at this wavelength in this longitude region are from the low quality α CrB experiment.

The contour maps for this region are shown in Figure 13 and expanded versions are given for better detail in Figures 14, 15 and 16 for the 4, 11 and 20-μm spectral bands, respectively. Effects of baseline errors show up as wings in the 4-μm map, Figure 14, at $\ell \sim 21^{\circ}$ and 25°, and as satellite sources at $\ell \sim 12^{\circ}$ and 16°.

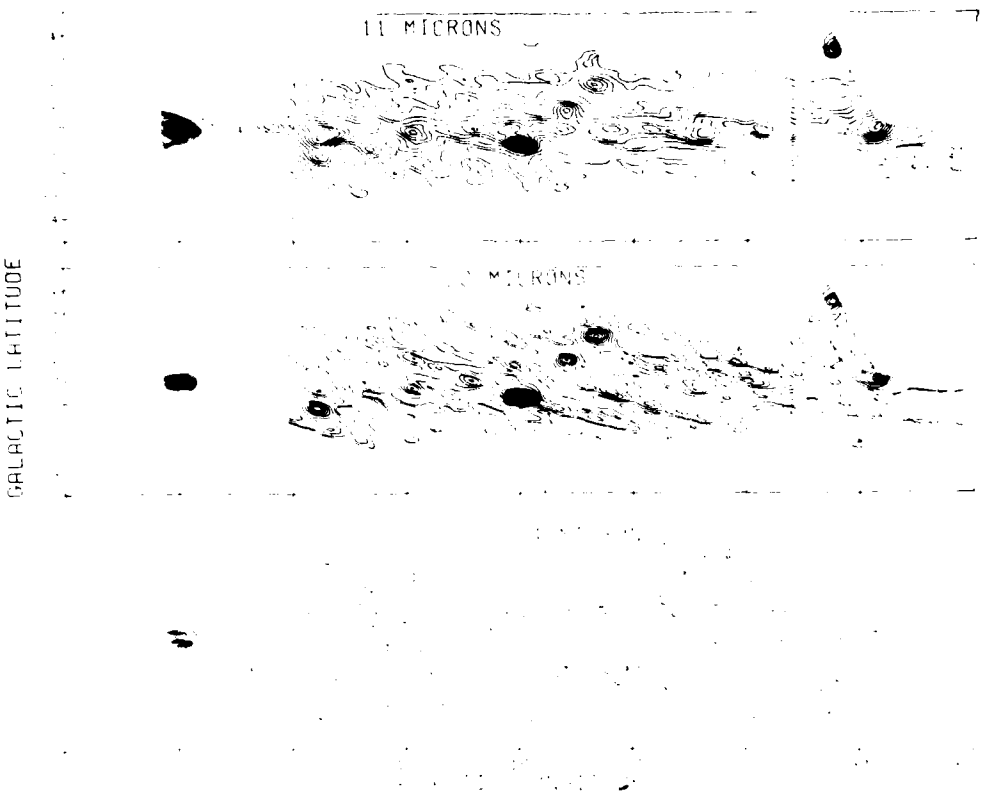

Figure 13. Contour Maps at 11, 20 and 4 μm for the Region $0^{\circ} \leq \ell < 35^{\circ}$. Contour levels at 1, 2, 4, 6 ... $\times 10^{-11}$ W cm^{-2} μm^{-1} sr^{-1} at 11 μm, 0.5, 1, 2, 3 ... $\times 10^{-11}$ W cm^{-2} μm^{-1} sr^{-1} at 20 μm and 5, 10, 15, 20 ... $\times 10^{-11}$ W cm^{-2} μm^{-1} sr^{-1} at 4 μm. The resolution on these maps is $0.^{\circ}7$ in latitude by $1.^{\circ}0$ in longitude. Features are extended sources as point sources have been eliminated in the data processing

The minimum contour level of the 11 and 20-μm maps, Figures 15 and 16, respectively, were raised for longitudes less than 5° as the signal-to-noise of the measurements were degraded in this region, due to the increased noise from the earthshine detected in the side lobe response of the optical system. The lower quality of the 20-μm data, evidenced by the striping along constant rocket zenith angle, shows the dominance of the α CrB flight. Not only is the signal-to-noise lower, but the baseline correction is more error prone as it must be fit over a larger time interval.

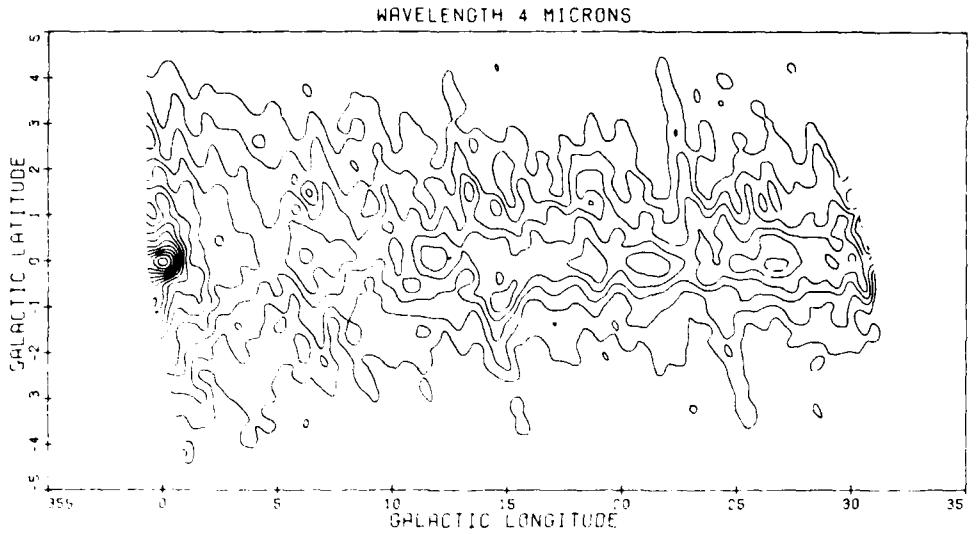

Figure 14. 4-μm Contour Map for the Region $0^{\circ} \leq \ell < 30^{\circ}$. The latitude scale is expanded over that given in Figure 13. The contour levels and resolution are the same as in Figure 13

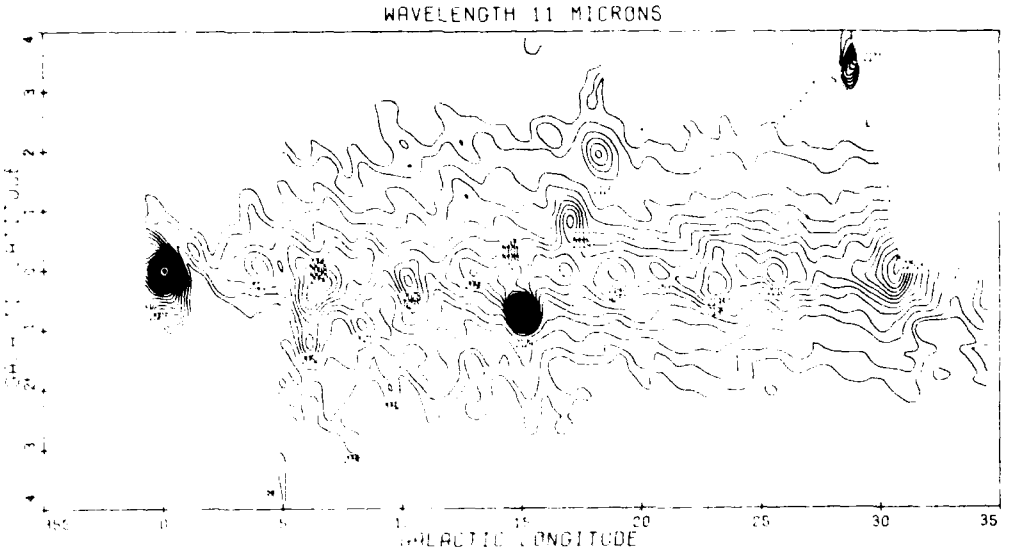

Figure 15. 11-μm Contour Map for the Region $0^{\circ} \leq \ell < 35^{\circ}$. The latitude scale has been expanded over that in Figure 13. The resolution and intensity levels are the same as in Figure 13. The contour levels are labeled on the figure and are in units of 10^{-11} W cm^{-2} μm^{-1} sr^{-1}. The numbers refer to the AFGL number of the source(s) associated with intensity peaks in the figure. Data for longitudes less than 5° are noisier than for the rest of the map and the minimum contour of this region is set at 6×10^{-11} W cm^{-1} μm^{-1} sr^{-1}

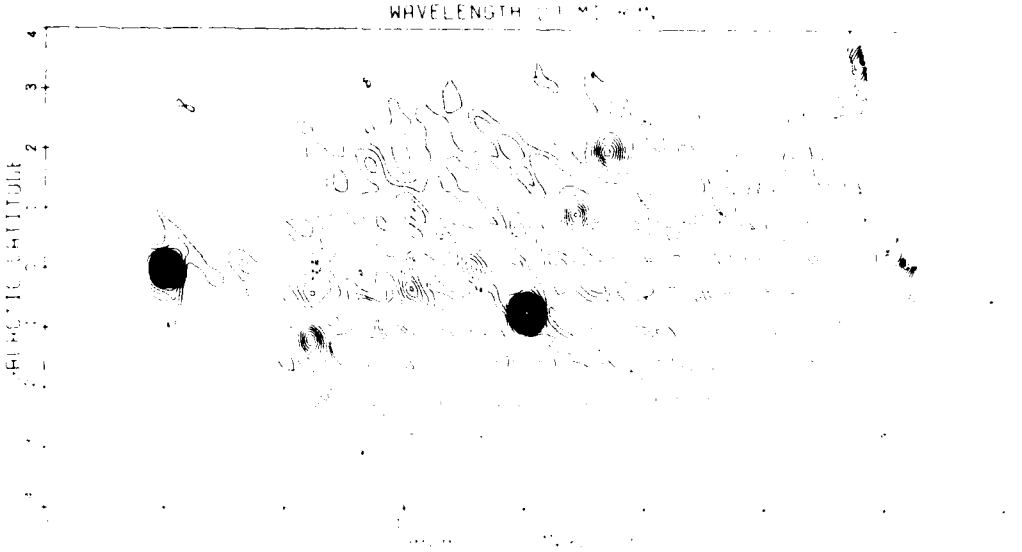

Figure 16. 20-μm Contour Map for the Region $0^{\circ} \leq \ell < 35^{\circ}$. The resolution and contour levels are the same as for the 20-μm map in Figure 13. The contour levels labeled in this figure are in terms of 10^{-11} W cm^{-2} μm^{-1} sr^{-1}. The minimum intensity level for longitudes less than 5° is set at 5×10^{-11} W cm^{-2} μm^{-1} sr^{-1} as the noise in this region is significantly higher than the rest of the plot. The numbers refer to the AFGL source(s) associated with intensity peaks.

The general character of the 4.2-μm emission is in excellent agreement with the balloon-borne 2.4-μm measurements made by Ito, Matsumoto and Uyama,[1] Okuda, Maihara, Oda and Sugiyama,[2] Oda, Maihara, Sugiyama and Okuda and the 2.4 and 3.4-μm observations of Hayakawa, Matsumoto, Murakami, Uyama, Yamagami and Thomas. The observations were made at various resolutions between 0.[illegible] and 2.0. A roughly constant 2.4-μm surface brightness of [illegible] $10^{-[illegible]}$ W cm^{-2} μm^{-1} sr^{-1} is measured along the galactic equator between [illegible] with a [illegible] full width at half maximum (FWHM). Hayakawa et al. [illegible] a narrower

[illegible] Ito, K., Matsumoto, T., and Uyama, K. (1977) Infrared profile of central [illegible] galaxy at 2.4 μm, Nature [illegible].

[illegible] Okuda, H., Maihara, T., Oda, N., and Sugiyama, T. (1977) 2.4 μm mapping [illegible]

[illegible] Central Region of the Galaxy [illegible] Infrared Source at [illegible] Astron. Astrophys. [illegible].

[illegible] Hayakawa, S., Matsumoto, T., Murakami, H., Uyama, K., Yamagami, T., [illegible] Brightness [illegible]

FWHM at 3.4 μm over these longitudes which they attribute to the lower interstellar extinction at this wavelength. The present results show an almost constant 4.2-μm surface brightness of 2×10^{-11} W cm^{-2} μm^{-1} sr at b $\sim 0^{\circ}$ between 5° and 30° longitude and a 3° FWHM. The 2.4-μm "fine structure" noted by Oda et al[22] and Hayakawa et al[23] at $\ell \simeq 14^{\circ}$, 16°, 19°, 21° and 27° also appears in Figures 13 and 14 at 4.2 μm. The 14° and 16° features are blended into a single extended plateau at 4.2 μm. The remaining features closely correspond at the two wavelengths. The peak at $\ell \sim 19^{\circ}$ is the only one which appears to be correlated with a source at longer wavelengths where it is associated with AFGL 2153 + 2162 (UY Sct).

Discrepancies between the 2.4 and 4.2 μm measurements do exist. The trend at 2.4 μm noted by Hayakawa et al[23] that the peak emission in this region occurs at b $\sim -0.^{\circ}5$ is not evident at 4.2 μm. Further, the details of the complexity of the galactic center observed by Oda et al[22] are not the same at 4.2 μm. The 4.2-μm grids clearly show emission peaks at $\ell \sim 0^{\circ}$, b = $+1^{\circ}$ and -1° as found at 2.4 μm but those intensities are much smaller than that observed for the center itself. This is contrary to what is seen at 2.4 μm.

Discrete, well-defined extended sources are prominent features of the 11 and 20-μm maps, Figures 15 and 16, respectively. A list of the extended sources discernible in the intensity grids in Appendix A has been compiled in Table 2 for this longitude region. The galactic coordinates of intensity peaks of the sources are listed in columns 1 and 2 to the nearest $0.^{\circ}1$. The peak intensities, in units of 10^{-11} W cm^{-2} μm^{-1} sr^{-1}, in 4, 11 and 20-μm spectral bands are given in columns 3, 4 and 5, respectively. The estimated angular extent of the source in longitude is given in column 6, and for latitude in column 7. The latitude estimates are more uncertain due to the more rapid variation in the diffuse background in this coordinate. The resolution of the grids is of the order of $0.^{\circ}8$ in longitude and $0.^{\circ}5$ in latitude. The true extent of sources roughly the size, or smaller than the $0.^{\circ}8$ by $0.^{\circ}5$ (fxb) resolution of the intensity grids is lost, but they must be greater than 0.3 by 0.2 as the nonlinear filtering would have eliminated smaller signals. The AFGL sources identified with the object is given in column 8 while other associations are listed in column 9. Column 10 contains pertinent comments about the object.

Most of the extended sources in Table 2 are identified with AFGL objects and almost all are associated with HII regions. The most notable exceptions are the 4-μm peaks near the galactic center at b $\sim +1.^{\circ}0$ which correspond to the 2.4-μm structure seen by Oda et al[22] and the source at $\ell \sim 17.^{\circ}0$, b $\sim -0.^{\circ}1$. The latter

Table 2. List of Extended Sources in the Region $0^{\circ} \lesssim \ell \lesssim 32^{\circ}$

ℓ	b	4 μm*	11 μm*	20 μm*	Θ_ℓ	Θ_b	AFGL	Associations	Comments
$359.^{\circ}8$	$-0.^{\circ}7$	15			$0.^{\circ}5$	$0.^{\circ}5$		Sh 16?	Probably the structure seen on the maps of Oda et al (1979)
0.0	1.3	12			1.2	1.2			Probably the structure seen on the maps of Oda et al (1979)
0.0	0.0	65	48	39	1.6	1.5	2003	FIR 5	Galactic Center
3.5	0.0		3	2	1.1	0.4		FIR 7, Sh 22, RCW 144	
3.9	0.1		4	1	0.9	0.4	2023		Peak at 11 μm, 20 μm continuous with previous source
5.0	-3.6		3		0.2	0.2	2086		
6.1	-1.2		4	8	1.2	0.8	2052	M8, RCW 146, Sh 25	
6.6	-0.3	5	10	4	1.9	1.0	2046 2048 2050	HFE 42, FIR 9, W 28 HFE 43, RCW 146 FIR 10, M20, RCW 147	Extended emission $\ell \sim 5.^{\circ}8$ to $7.^{\circ}4$, $b \sim -0.^{\circ}6$ to $+0.^{\circ}1$ coordinates are for the 11 μm peak, 20 μm peak at $\ell = 6.^{\circ}0$, $b = -0.^{\circ}5$
7.0	-2.2	6	3	3	1.0	0.7		Sh 29, Sh 31, Sh 32	20 μm peak at $\ell \sim 6.^{\circ}9$, $b \sim 2.^{\circ}2$, 11 μm peak $\ell \sim 7.^{\circ}3$, $b \sim -2.^{\circ}0$
8.0	-2.8		3	2	0.6	0.3	2096		
8.3	0.0		2	1	0.7	0.4	2051		
8.4	-1.0		6	4	0.9	0.5	2071	VX Sgr, RCW 149, Sh 34	
9.5	-2.0		3	1	0.6	0.3	2092		
10.2	-0.3		6	7	1.2	0.5	2078 4235	HFE 49 FIR 12, W 31	
11.4	-1.8		4		0.8	0.4		RCW 151, Sh 35	
12.5	-1.1		4	4	0.9	0.5	2107	Sh 39	
12.85	0.05		3	6	1.2	0.6	2090	HFE 50, FIR 13, Sh 40	
14.6	0.0		7	4	1.6	0.6	2101 2103 2105 2109	Sh 44, HFE 51, RCW 1 RCW 157, IC 4701	11 μm peak on 2105, 20 μm emission centers around AFGL 2101+2103+2109

Table 2. List of Extended Sources in the Region $0^{\circ} \leq \ell \leq 32^{\circ}$ (Cont.)

ℓ	b	4 μm*	11 μm*	20 μm*	Θ_{ℓ}	Θ_{b}	AFGL	Associations	Comments
17.0	-0.7	13	9	7	1.1	1.0	2124	S117, FIR 14, Sh 45, RCW 149	
17.6	1		2	1	0.6	0.3		Sh 46, RCW 158	
17.9	-0.4		4	3	0.8	0.4		FIR 15	
18.0	0.8		5	11	0.8	0.4	2119 2117	RCW 163, M16, FIR 15 Sh 49, NGC 6611	
18.2	-0.1	6	4	5	0.9	0.2	2147 4237	Sh 53, RCW 166	On a plateau with AFGL 2157 4 μm $17.^{\circ}8 < \ell < 19.^{\circ}5$; $0.^{\circ}4 < b < -0.^{\circ}4$
18.2	1.7		10	8	1.2	0.6	2113	NGC 6604, Sh 54, RCW 167	
18.8	-0.3		6	6	0.9	0.3	2157	W39, FIR 17, RCW 166	
19.0	2.6		4	2	0.9	0.3	2123		Peak at 11 μm
19.2	-0.7		5	7	0.8	0.4	2152	UY Sct	Peak at 20 μm
20.7	0.6	9	4	4	1.2	0.5	2169	FIR 18	4 μm peak at $\ell = 20.^{\circ}5$, $b = 0.^{\circ}0$
21.0	-0.7		3	7	1.0	0.5			20 μm displaced to $\ell = 21.^{\circ}3$, $b = -1.^{\circ}2$
23.2	-0.2		7	5	1.6	0.7	2193	W41, FIR 19&20	20 μm peak at $\ell = 22.^{\circ}7$, $b = -0.^{\circ}5$
24.5	0.9		4	3	1.0	0.6	2202	RCW 172, S59, FIR 20	
25.2	-0.1	12			1.4	0.6		W42	Overlaps with EW Sct
25.6	-0.05		7	4	1.0	0.6	2210	EW Sct, FIR 22, W42	
26.5	0.7		3	2	0.6	0.4	2205		
27.7	-0.2		4	4	1.0	0.5	2223		4 μm about twice as extensive
26.9	0.1		2		small		2227		
28.3	2.9		13	9	0.6	0.8	2177	RCW 174, W40, Sh 64	
30.7	-0.1		13	11	1.8	0.9	2251	AB Aql, FIR 25	

* 10^{-11} W cm^{-2} μm^{-1} sr^{-1}

Reference in Association Column

HFE = Hoffmann, Frederick and Emery (1971)
Sh = Sharpless (1959)
RCW = Rodgers, Campbell and Whiteoak (1960)
FIR = Nishimura, Low and Kurtz (1980)
W = Westerhout (1958)

object is near source 16 in the far infrared list of Nishimura, Low and Kurtz[23] which they associate with a strong CO peak but without bright HII emission.

The diffuse emission component at 11 and 20 μm is qualitatively similar to that observed at shorter wavelengths. A roughly constant emission centered on the galactic equator between $5^{\circ} < \ell < 30^{\circ}$ is observed to have a value of $\sim 1.2 \times 10^{-10}$ W cm^{-2} μm^{-1} sr^{-1} for the 11 μm band and $\sim 3 \times 10^{-11}$ W cm^{-2} μm^{-1} sr^{-1} at 20 μm. The FWHM is measured to be between 1.5 and 2.0 at 11 μm and 1.0 to 1.5 at 20 μm. Thus, the 4:11-μm and 11:20-μm intensity ratios along the galactic equator are roughly constant at about 1.6 and 4, respectively.

5.2 Longitudes 35° to 95°

This region was surveyed at 11 and 20 μm on four experiments. The pole stars and their galactic latitudes are, in sequence: α CrB b $\sim 53.^{\circ}75$; α And, b $\sim 32.^{\circ}85$; ε Sgr, b $\sim -9.^{\circ}6$; γ Gru, b $\sim -51.^{\circ}5$. The two southern hemisphere flights (ε Sgr, γ Gru) obtained 27.4-μm measurements between $40^{\circ} < \ell < 85^{\circ}$. At longitudes greater than about 80°, the observations are from a single experiment, the α And flight, whereas the ε Sgr dominate the data for longitudes less than 45° to 50°.

The 11, 20 and 27-μm equal intensity contour maps are shown in Figure 17 while expanded versions of these measurements are given in Figures 18, 19, and 20, respectively. The sensitivities of the 27-μm detectors were not high enough to measure the diffuse emission from the galactic plane and observations in this color are limited to the brightest discrete sources. Two general areas of 11 and 20-μm emission are apparent in this region: One extends from about 35° to 65° longitude, and associated with the diffuse emission from the galactic plane; the other is a complex of diffuse and discrete infrared emission from the Cygnus X region.

The background associated with the galactic plane decreases both in brightness and FWHM at 11 and 20 μm, with increasing longitude from $\ell \sim 38^{\circ}$ to $\ell \sim 65^{\circ}$ where the brightness drops below the detection threshold in both colors. The measurements are qualitatively similar to those observed at 2.4 μm by Ito, Matsumoto and Uyama[19] and Hoffmann, Lemke and Frey.[24] The observed 11:20-μm ratio of surface brightness along the galactic equator is almost constant somewhere between 3 and 4 out to a longitude of 65°.

The extended sources obtained from the intensity grids in Appendix B are listed in Table 3. The more prominent objects are labeled with the AFGL source

---

23. Nishimura, T., Low, F.J., and Kurtz, R.F. (1980) Far Infrared Survey of the Galactic Plane, Astrophys. J. (Letters) 239:L101.

24. Hoffman, W., Lemke, D., and Frey, A. (1978) Mapping of the Galactic Center and the Aquila Region in the Near Infrared from Balloon Altitudes, Astronomy and Astrophysics 70:427.

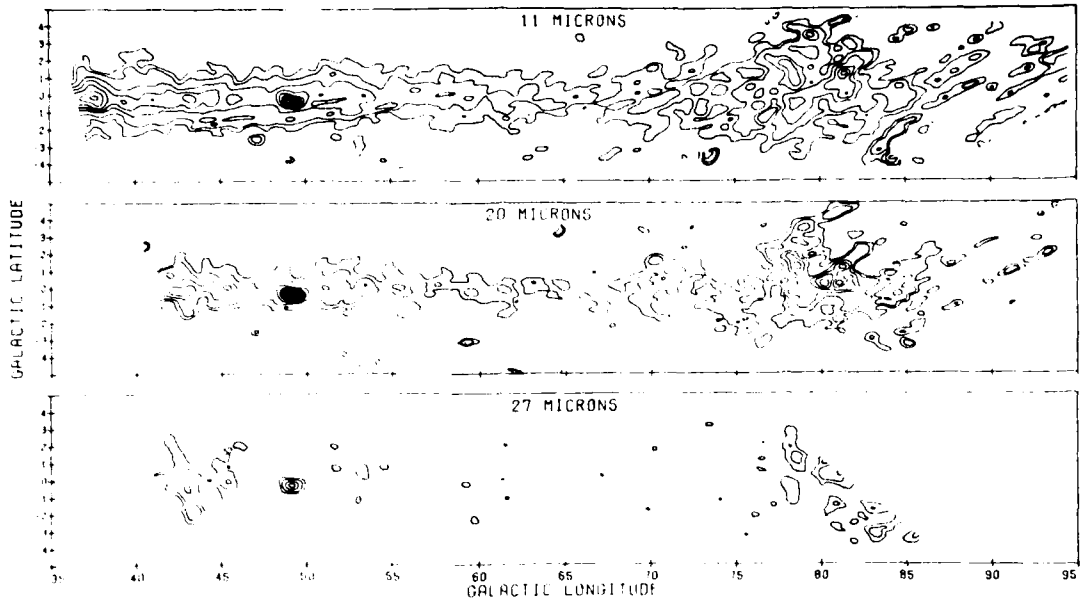

Figure 17. The 11-, 20- and 27-μm Equal Intensity Contour Maps of the Galactic Plane in the Region $35^{\circ} < \ell < 95^{\circ}$. Contour levels are 1, 2, 4, 6 ... $\times 10^{-11}$ W cm^{-2} μm^{-1} sr^{-1} for the 11-μm observations, 0.5, 1, 2, 3 ... $\times 10^{-11}$ W cm^{-2} μm^{-1} sr^{-1} at 20 μm and 2.5, 5, 10, 15 ... $\times 10^{-11}$ W cm^{-2} μm^{-1} sr^{-1} at 27 μm. The resolution of the mapping is about $0^{\circ}.7$ in latitude and $1^{\circ}.0$ in longitude in all colors. Peaks are due to sources larger than $0^{\circ}.2$

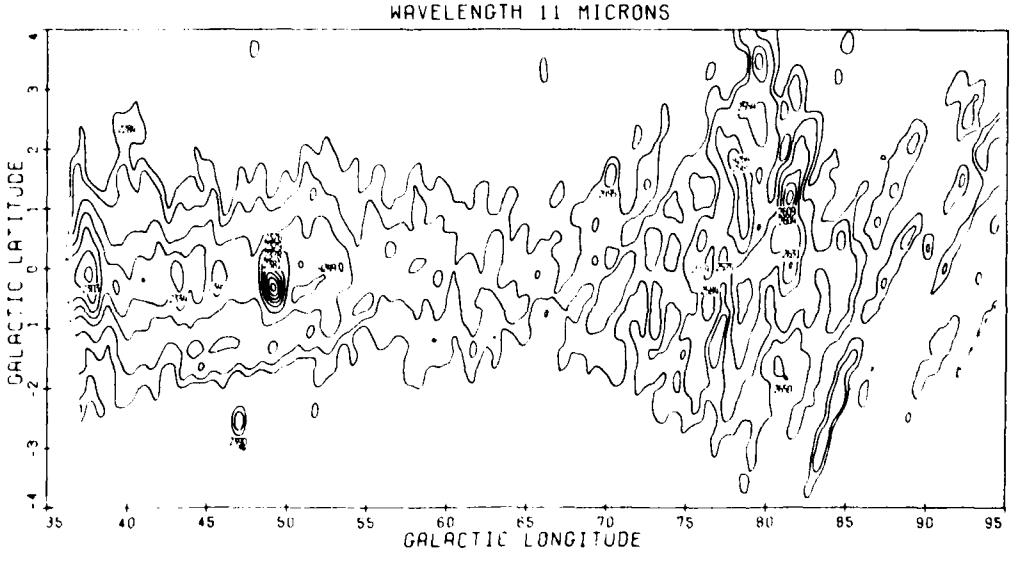

Figure 18. 11-μm Map of the Galactic Plane over the Region $35^{\circ} < \ell < 95^{\circ}$. The brightness levels are in units of 10^{-11} W cm^{-2} μm^{-1} sr^{-1}. Prominent features are labeled with the AFGL source number associated with them

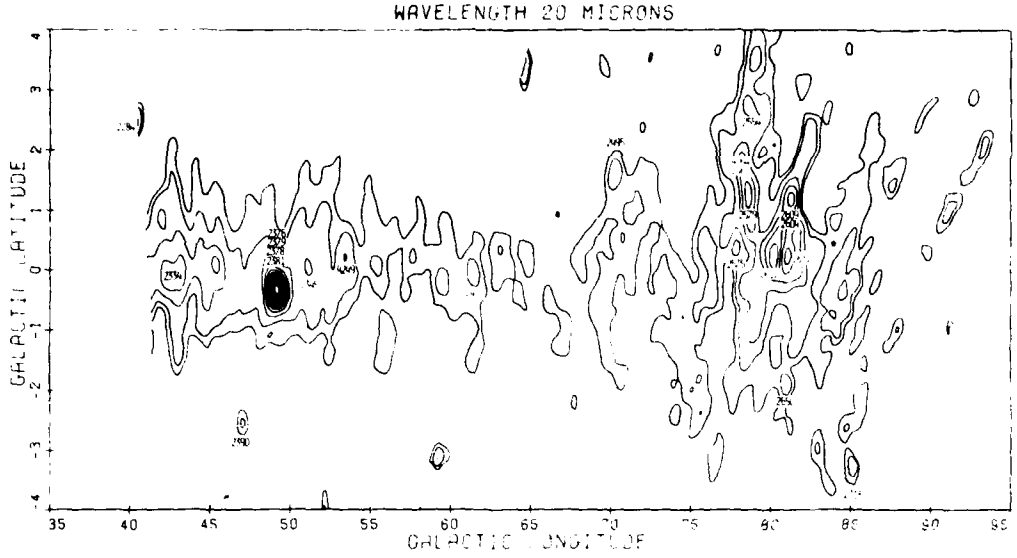

Figure 19. 20-μm Map of the Galactic Plane from 35° to 95° Longitude. Contour levels are in units of 10^{-11} W cm^{-2} μm^{-1} sr^{-1}. Intensity peaks of the extended sources in this region are labeled with the AFGL source number associated with them

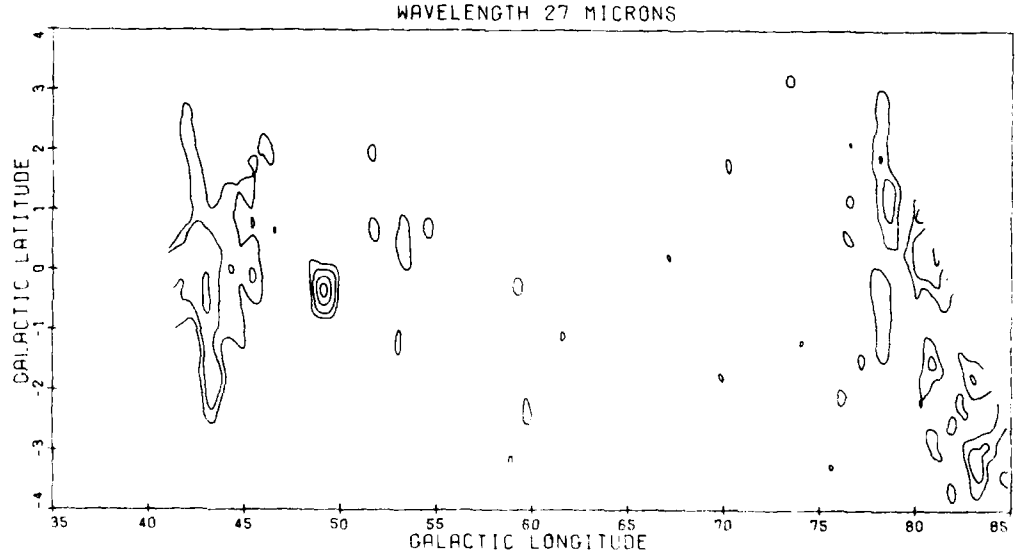

Figure 20. The 27-μm Map of the Galactic Plane Between 40° and 85° Longitude. Contour levels are 2.5, 5, 10, 15 ... $\times 10^{-11}$ W cm^{-2} μm^{-1} sr^{-1}

Table 3. List of Extended Sources in the Region $35^{\circ} \leq \ell \leq 95^{\circ}$

ℓ	b	11 μm*	20 μm*	27 μm*	Θ_ℓ	Θ_b	AFGL	Associations	Comments
$37.^{\circ}6$	$-0.^{\circ}1$	6			$1.^{\circ}7$	$1.^{\circ}5$	2303	FIR 28, W 47	
39.2	-0.2	3			0.8	0.7			
40.6	2.3	3			1.0	0.4	2284	Sh 76	
41.0	-0.2	2			0.8	0.4	2326	FIR 29	Broad peak in longitude connecting with next source
42.1	-0.2	2	2	8	0.4	0.4		FIR 30, W 49	
43.2	-0.2	5	2	8	1.1	0.6	2334		
44.7	-1.7	7			0.6	0.3	2374		
45.4	0.0	2	3	6	0.9	0.4	2341 2345		
47.0	-2.6	4	1	4	0.8	0.4	2390 2376	IRC $+10^{\circ}420$	
49.2	-0.3	14	13	19	1.6	0.9	2379 2381	HFE 59 HFE 60	Emission from AFGL 2371, 2378 and 2380 also probable
53.4	0.0	3	1	2	1.1	0.8	4249	Sh 82	
55.1	-0.6	6	1	1	0.8	0.4			
58.1	0.0	3	1	1	1.0	0.4			
59.4	-0.2	3	1	3	0.9	0.5		Sh 86, NGC 6820	
61.3	-0.2	2	1	2	0.8	0.4	2455	Sh 87 + Sh 88	
63.0	0.0	3	1	1	1.1	0.8		Sh 89	
64.8	-0.6	4	1	3	0.8	0.7	4256		Includes Sh 93 as an 11 μm and 20-μm extension
66.9	1.2	2			small			Sh 97	
70.0	-0.6	4	2	1	0.8	0.5			
70.3	1.6	4	2	3	0.8	0.3	2495	HFE 63, NGC 6857	
73.0	-0.9	3	1	1	0.8	0.8	2550		
75.4	0.1	3	1	1	0.8	0.4	2559	BI Cyg	
75.8	0.4	5	2	2	0.8	0.4	2560	BC Cyg	
76.4	-0.6	6	2	2	1.0	0.6	2584	Sh 106, CIR 5 + CIR 8	
76.6	2.2	2	2	1	1.0	0.6		G76.8+2.2	Position from 27.4 μm peak, at and 20 μm; this is an extension of the γ Cyg source

Table 3. List of Extended Sources in the Region $35^{\circ} \lesssim \ell \lesssim 95^{\circ}$ (Cont.)

ℓ	b	11 μm*	20 μm*	27 μm*	Θ_ℓ	Θ_b	AFGL	Associations	Comments
$77.^{\circ}4$	$0.^{\circ}2$	4	1	1	$0.^{\circ}9$	$0.^{\circ}6$	2575		Includes AFGL 2593
78.0	1.8	8	4	6	1.4	1.0	2565	CIR 1, W66, Sh 108	γ Cygnus complex, includes AFGL 4263 and 4264
78.5	2.7	5	3	5	1.0	0.6	2554		Includes 2557
78.5	1.2	8	5	7	0.7	0.6	2579	G78.5+1.2, IC 1318b	In an emission ridge connected to the γ Cyg source
78.5	-0.5	7	3	2	1.5	1.0	2593	W69, CIR 8	Cygnus rift, 20 and 27 μm peak on G78.2-0.4
							4267	CIR 18	
							2607		
79.0	3.5	3	4		0.9	0.6		G79.0+3.6, IC 1318a	
79.4	3.5	8	1		1.1	0.6		G79.4+3.2, G79.9 +3.3	
79.4	2.4	4	2		0.9	0.6		G79+2.4, G79.0+2.5	
80.2	0.2	3	5	10	1.0	0.7	2612	G80.4+0.4	Peaks at 20 and 27 μm; forms a ridge with AFGL 2616 in 11 μm
80.9	0.5	9	3		0.9	0.4	2616		
							2612		
81.0	-1.9	2	2	2	0.6	0.3	2650		
81.3	1.2	12	6		0.8	0.6	2604	W72	
							2609		
81.5	0.0	8	4		0.8	0.4	2631	G81.6+0.0, HFE 59+60	
82.2	2.2	5	2		0.7	0.5		G82.2+2.4	
84.6	0.5	6	2		0.7	0.7		CIR 46	
84.9	3.8	2	1		0.7	0.3		Sh 116	
84.9	-3.5	1	1		0.7	0.3	2613	NGC 7027	
85.1	-0.1	4	1		0.7	0.3		CIR 47	

*$\times 10^{-11}$ W cm^{-2} μm^{-1} sr^{-1}

References in Association Column

FIR = Nishimura, Low and Kurtz (1980)
W = Westerhout (1958)
HFE = Hoffmann, Frederick and Emery (1971)
IRC = Neugebauer and Leighton (1969)
Sh = Sharpless (1959)
G = Wendker (1970)
CIR = Campbell, Hoffmann, Thronson and Harvey (1980)

numbers associated with them in Figures 18 and 19 for the 11 and 20-μm spectral bands, respectively. The format of Table 3 is the same as Table 2 with the exception that columns 3, 4, and 5 list the observed 11, 20, and 27-μm peak intensity, respectively, in units of 10^{-11} W cm^{-2} μm^{-1} sr^{-1}.

The source at $\ell \sim 47.^{\circ}0$, $b \sim -2.^{\circ}6$ (AFGL 2390) associated with object $+10^{\circ}420$ in the catalog of Neugebauer and Leighton;[25] it is most likely the "unknown" source reported by Hoffmann et al.[24] The 2.4-μm position of Hoffman et al is $1.^{\circ}4$ from that of $+10^{\circ}420$ = AFGL 2390 and within the position accuracy of the 2.4-μm observations. Of interest is the fact that AFGL 2390 appears both in the maps of Figures 18 and 19 and in Table 3 with a measured extent equal to the resolution of the intensity grid. A source must be greater than $0.^{\circ}2$ to appear in the grids, as objects smaller than this are eliminated by the nonlinear smoothing. Note that AFGL 2650 = $+40^{\circ}448$ = NML Cyg also shows up at all three colors at the resolution limit of the data.

A number of extended sources are listed in Table 3 in the Cygnus X region; not all of these are identified with AFGL cataloged objects. Campbell, Hoffmann, Thronson, and Harvey[26] conducted an overlapping survey in broad spectral bands centered at 82 and 92 μm with $0.^{\circ}2$ resolution. Their experiment covered a 5 degree latitude strip from $\ell = 76^{\circ}$ to 90°. Forty-nine discrete sources were detected at the far infrared wavelengths, seventeen of which were associated with AFGL objects. Of these, thirteen also correspond to peaks in the 11 cm radio emission in Wendker's survey. Kleinmann, Joyce, Sargent, Gillett and Telesco[27] have previously noted the coincidence between peaks in the Wendker survey and the positions of AFGL sources. About half of the AFGL objects associated with the 11-cm peaks by Kleinmann et al[27] or with far infrared emission by Campbell et al[26] are extended enough to appear in Table 3. The remainder were either too small and, in consequence, eliminated by the smoothing, or blended into an extended emission ridge or combined with other sources. Indeed, several of the prominent ridges of far infrared emission are also seen at 11, 20 and 27 μm. The γ Cygnus ridge ($77.^{\circ}5 \lesssim \ell \lesssim 79^{\circ}$, $2.1 \lesssim b \lesssim 0.^{\circ}5$) is nicely traced out by sources 1, 6, and 10 of Campbell et al[26] with 11-μm peaks near the far infrared sources 1 and 6. Another ridge in the area $78^{\circ} \lesssim \ell \lesssim 79.^{\circ}5$, $-1.^{\circ}5 \lesssim b \lesssim 0^{\circ}$ is outlined by the 11-cm sources which Wendker[28] found in the Great Cygnus Rift of heavy obscuration. This region

25. Neugebauer, G., and Leighton, R.B. (1969) Two Micron Sky Survey—A Preliminary Catalog, NASA SP-3047.

26. Campbell, M.F., Hoffmann, W.F., Thronson, Jr., H.H., and Harvey, P.M. (1980) Far-Infrared Survey of Cygnus X, Astrophys. J. 238:122.

27. Kleinmann, S.G., Joyce, R.R., Sargent, D.G., Gillett, F.C., and Telesco, C.M. (1979) An Observational Study of the AFGL Infrared Sky Survey. IV. Further Results from the Revised Catalog, Astrophys. J. 227:126.

28. Wendker, H.J. (1970) The Cygnus X Region VI. A New 2695 MHz Continuum Survey, Astron. Astrophys. 4:378.

also contains sources 12, 18, 19 and 26 of Campbell et al;[26] the 20-μm emission peak is near the positions of far infrared sources 18 and 29.

The Cygnus X region is complex and separating the diffuse emission from discrete extended sources and from ridges of emission is not straightforward. More than half of the extended objects listed in Table 3 for this region are associated with sources, or groups of sources, in the AFGL catalog. The objects in Table 3 without AFGL associates for this region have associations in other catalogs, most notably that of Wendker.[28] The most prominent of these is the extended source at $\ell = 79.^{\circ}4$ and $b = 3.^{\circ}5$ (11-μm position) and $\ell = 79.^{\circ}0$, $b = 3.^{\circ}5$ (20-μm position). This is associated with G79.0 + 3.5, G79.4 + 3.2 and possibly G79.3 + 3.3 in the list of Wendker.[28] The gradients across this source were apparently too shallow to produce a discernible signal after the low frequency attenuation in the electronics. Indeed, all the extended sources in Table 3 corresponding to objects in Wendker's list but not in the AFGL catalog have shallow gradients at 11 cm. On the other hand, of the 15 objects in the list of AFGL sources which Kleinmann et al[27] associate with the 11-μm emission, only two were not at locations of reasonably steep 11-μm gradients.

That the AFGL catalog preferentially includes sources with reasonably steep intensity gradients coupled with the fact that the positions of the peak intensity of the sources in Table 3 are, in general, within 0.1 of the AFGL catalog position contradicts the surmise of Kleinmann et al[27] "... that the positions and extent of sources in at least one complex area (Cyg X) were inadequately determined by the AFGL survey because of spatial resolution and sensitivity." The positions for the peak of a source listed in the AFGL catalog, which includes the effects of the high pass filter, and that found after restoration are within the quoted errors of the catalog and the intensity grids in Appendix B. The position of the intensity peak, and the region of highest spatial frequencies, are quite well-defined, not at all "inadequately determined." The detection and measured angular extent of the source is a function of the intensity gradient in this region, not solely sensitivity. Objects with too shallow a gradient were not detected and thus excluded from the catalog.

The mid-infrared color of the diffuse emission in this region is redder than that derived for the galactic plane, with a 11:20 μm ratio of 2 to 2.5. There is also general correlation between the surface brightness of the 11 and 20 μm emission and the brightness temperature derived by Wendker.[28] Along the 1.5°K 11-cm contour the 11 and 20 μm emission appear to be related to the 11-cm brightness temperature by $I\ (11\ \mu m) \sim 2.5\ I\ (20\ \mu m) \sim 2 \times T_b\ (^{\circ}K^{-1})$ ($W\ cm^{-2}\ \mu m^{-1}\ sr^{-1}$).

5.3 Longitudes 100° to 240°

Three flights surveyed this longitude region in two major segments. Zeta Tau ($b \sim -5.^{\circ}7$), ζ Per ($b \sim -26.^{\circ}6$) and α And ($b \sim -32.^{\circ}9$) cover the regions between 100° and 170°. The ζ Tau and ζ Per experiments also surveyed between 195° and 240° longitude.

Figure 21 shows the 11- and 20-μm contour maps in the region $100^{\circ} < \ell < 170^{\circ}$ with expanded maps given in Figures 22 and 23, respectively. The area 195° to 240° longitude is mapped in Figure 24; individual contour maps are presented in Figure 25 for the 11-μm measurements and Figure 26 for the 20-μm values.

As may be seen from these figures, only discrete sources are contained in this region. There is no diffuse emission centered on the galactic plane above 10^{-11} W cm^{-2} μm^{-1} sr^{-1} in either color. The list of discrete sources found within these longitudes is given in Table 4. The galactic coordinates of the source are given in the first two columns of the table, longitude in column 1, latitude in column 2, and the peak intensities at 11 and 20 μm are given in columns 3 and 4, respectively. The estimated angular extent in longitude is given in column 5 and the latitude value in column 6. Associations with sources in the AFGL catalog are made in column 7, and with other catalogs in column 8. Finally, column 9 contains comments about the source.

Approximately equal numbers of HII regions in Table 4 are associated with AFGL sources as those which are not. The AFGL catalog undersamples the HII region contribution by not detecting those extended sources with shallow intensity gradients.

Several of the HII complexes are quite large. NGC 896 ($\ell \sim 134^{\circ}$, $b \sim 1.^{\circ}2$) is measured to have a diameter of about 1.5 degrees and may be larger if the lowest contour level is valid at 20 μm. Similarly, NGC 7822 is at least a degree in diameter. This source extends beyond the boundaries of the plot ($\ell \sim 118^{\circ}$, $b \sim 5^{\circ}$) and is only partially seen in Figure 21. The region containing NGC 2244 ($\ell \sim 207^{\circ}$, $b \sim 1.^{\circ}7$) is as much as 2.5 degrees across. The entire extent of this region could not be determined as the measurements across the edge of this source were eliminated because of telemetry problems on the flight that surveyed this region. Unfortunately, this scan also covered NGC 2264 which is also quite bright in the mid-infrared.

5.4 Longitudes 280° to 320°

The two southern hemisphere flights covered this region, producing data in the 11-, 20- and 27-μm spectral bands. The instrument flown on the ϵ Sgr ($b \sim -9.^{\circ}6$) experiment was more sensitive than that used on the γ Gru ($b \sim -51.^{\circ}5$) flight. Also, four of the 11-μm and two of the 20-μm detectors were inoperative on the

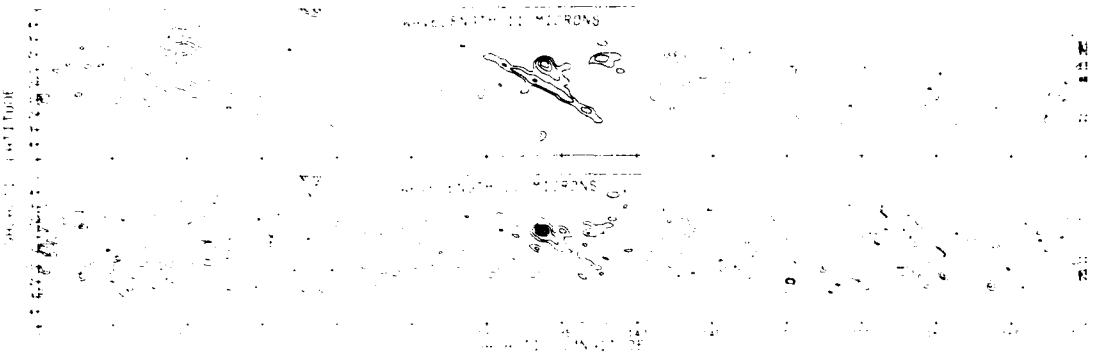

Figure 21. The 11- and 20-μm Map of the Galactic Plane for Longitude Between 100° and 170°. Contour levels are 1, 2, 4, 6, 8 ... $\times 10^{-11}$ W cm^{-2} μm^{-1} sr^{-1} for the 11-μm plot and half that for 20 μm. The blank streaks at $\ell \sim 120^{\circ}$ and 155° are due to scans which were eliminated during data processing. The resolution is approximately 0°.7 in latitude and 1°.0 in longitude

Figure 22. An Expanded Version of the 11-μm Map in Figure 32

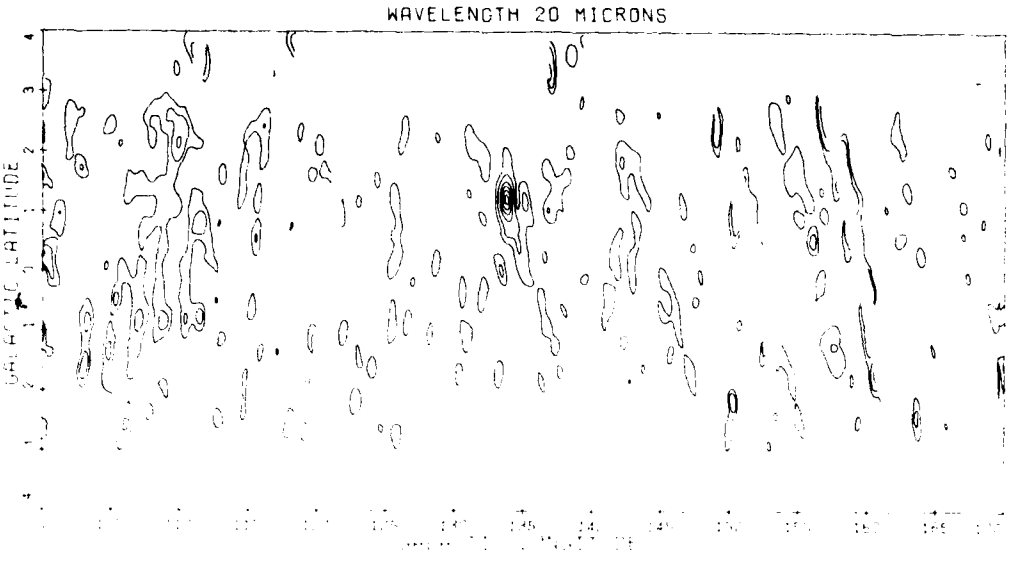

Figure 23. An Expanded Version of the 20-μm Map in Figure 21

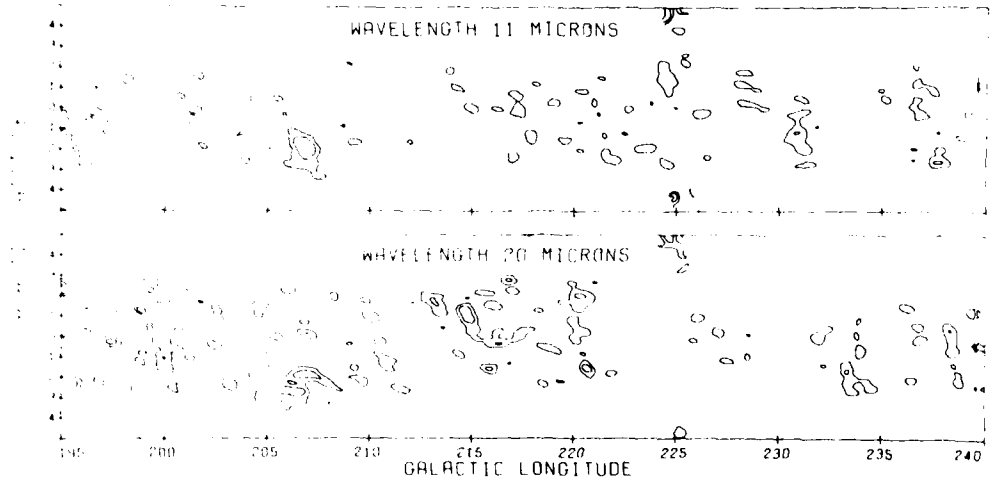

Figure 24. 11- and 20-μm Maps of the Galactic Plane from 195° to 240° Longitude. Contour levels are the same as defined in Figure 21. The resolution of these maps is approximately 0°.7 in latitude and 1°.0 in longitude

Figure 25. Expanded Version of the 11-μm Map in Figure 24

Figure 26. Expanded Version of the 20-μm Map in Figure 24

Table 4. Extended Sources in the Region $100^{\circ} \lesssim \ell \lesssim 235^{\circ}$

ℓ	b	11μm*	20μm*	Θ_{ℓ}	Θ_{b}	AFGL	Associations	Comments
$100.^{\circ}5$	$-1.^{\circ}3$	3	1	$0.^{\circ}8$	$0.^{\circ}4$			
102.8	-0.7	2	1	0.8	0.4		Sh 132	
104.4	1.8	2	1	1.0	0.9		Sh 135	Association is tentative
104.9	2.4	2	2	0.7	0.5	2885		
107.5	-0.8	2	1	1.1	0.6		Sh 142, NGC 7380	
108.8	-0.6	2	2	1.4	1.0	2991	Sh 147, Sh 148	
						2999	Sh 149, Sh 152	
						3004	Sh 153	
109.3	1.4	3	1	1.0	0.8		Sh 154	
109.8	2.4	4	2	1.5	1.0	3000	Sh 155	
111.5	0.8	4	2	1.5	1.5	3048	Sh 158, NGC 7538	
						3053	Sh 159	
						3079		
111.5	-0.7	2	2	0.8	0.4	3057	Sh 157	
113.1	-1.0	2	1	0.9	0.7	3109		
						4999		
118.0	5.0	4	4	1.0	1.0	3193	Sh 171	
						4305	NGC 7822	
126.9	-0.8	2	1	0.8	0.8	205	Sh 187	
133.4	0.0	5	1	1.0	0.5			
133.7	1.2	9	6	1.4	1.4	326	Sh 190, NGC 896	
						328	W3, W4	
						321		
						333		
137.6	1.5	3	1	2.0	0.9	4029	Sh 199, IC 1848	
						416	Sh 201	

Table 4. Extended Sources in the Region $100^{\circ} \leq \ell \leq 235^{\circ}$ (Cont.)

ℓ	b	11 μm*	20 μm*	Θ_ℓ	Θ_b	AFGL	Associations	Comments
142.3	1.8	3	1	1.3	0.7	490		
196.0	-2.4	2	2	0.6	0.6		Sh 268, Sh 270	
196.4	-1.6	1	1	0.6	0.4	902	Sh 269	
201.6	1.7	2	1	0.8	0.6			
206.8	-1.7	4	2	1.7	2.5	961 971	Sh 275, NGC 2244	
212.0	-1.4	2		0.7	0.6		Sh 284	
214.8	1.2	1.	2	1.0	1.0			
217.4	0.1	2	1	1.0	1.5			
220.7	-1.6	1	2	0.8	0.6		NGC 2316	
223.7	-1.8	2	1	1.7	0.7		RCW 1, RCW 2	Large diffuse source extends to the object at ($\ell \sim 224.7$, b = 2.7)
224.5	1.5	2		1.2	1.5		RCW 3, Sh 292, Sh 294	
224.7	-2.7	2	1	1.5	0.6	1059	Sh 295, Sh 293, Sh 296	
225.0	3.8	2	1	>1.1	1.0		RCW 4	
226.2	-0.2	2	1	1.2	1.0			
230.8	-1.1	3	1	1.0	0.8			
223.4	-1.8	1	2	0.7	0.7			

* In units of 10^{-11} W cm^{-1} μm^{-1} sr^{-1}

References in Association Column

RCW = Rodgers, Campbell and Whiteoak (1960)
Sh = Sharpless (1959)
W = Westerhout (1958)

γ Gru flight. Thus, the data from the ε Sgr experiment is dominant in this region.

The iso-intensity maps are shown for the three colors in Figure 27. Individual maps are presented in Figure 28 for the 11-μm spectral band, Figure 29 for 20 μ and Figure 30 for 27 μm. Again, the sensitivity at 27.4 μm was not high enough to detect diffuse emission from the general background arising from the galactic plane.

Prominent peaks in Figures 28 and 29 are identified with the AFGL number of the sources associated with them. A more complete list of extended sources in this region is given in Table 5. The format for this table is the same as for Table 3. The general character of the 11 and 20-μm emission over this region is similar to that observed for the complementary area $40^{\circ} \lesssim \ell \lesssim 80^{\circ}$. The diffuse

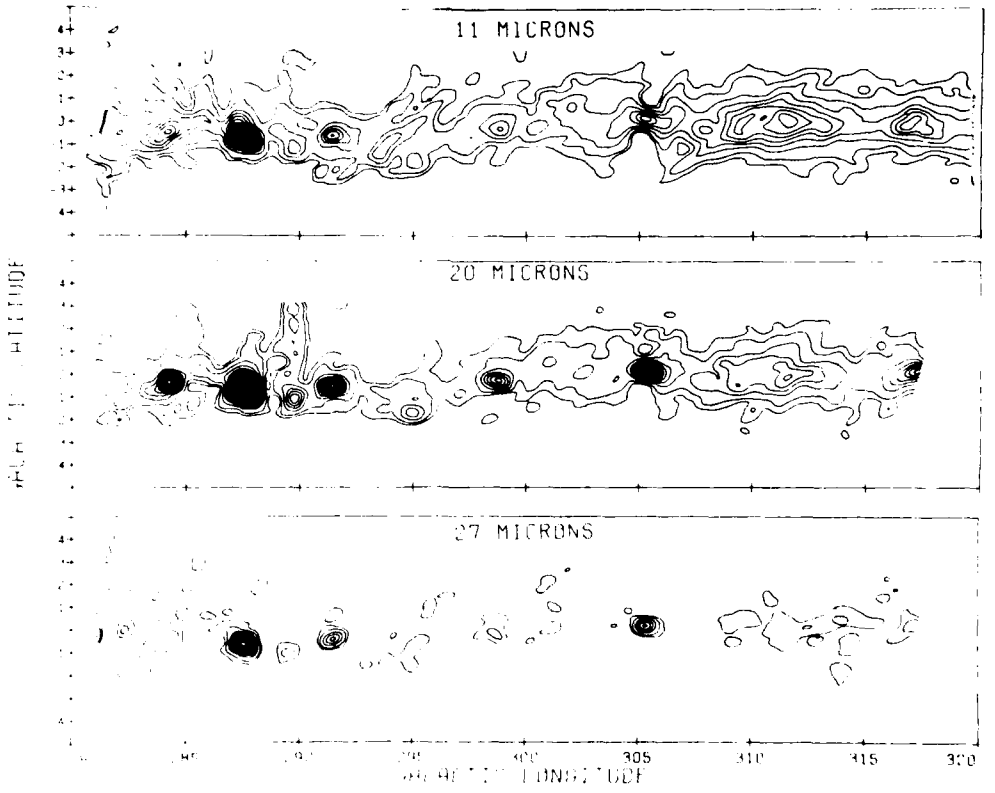

Figure 27. The 11-, 20- and 27-μm Equal Intensity Contour Maps of the Galactic Plane from 280° to 320° Longitude. Contour levels are the same as in Figure 17; at 11-μm these are 1, 2, 4, 6 ... $\times 10^{-11}$ W cm^{-2} μm^{-1} sr^{-1}, the 20 μm levels are half those at 11 μm and the 27 μm value 2.5 times those at 11 μm. The angular resolution of these plots are about $0.^{\circ}7$ in latitude and $1.^{\circ}0$ in longitude

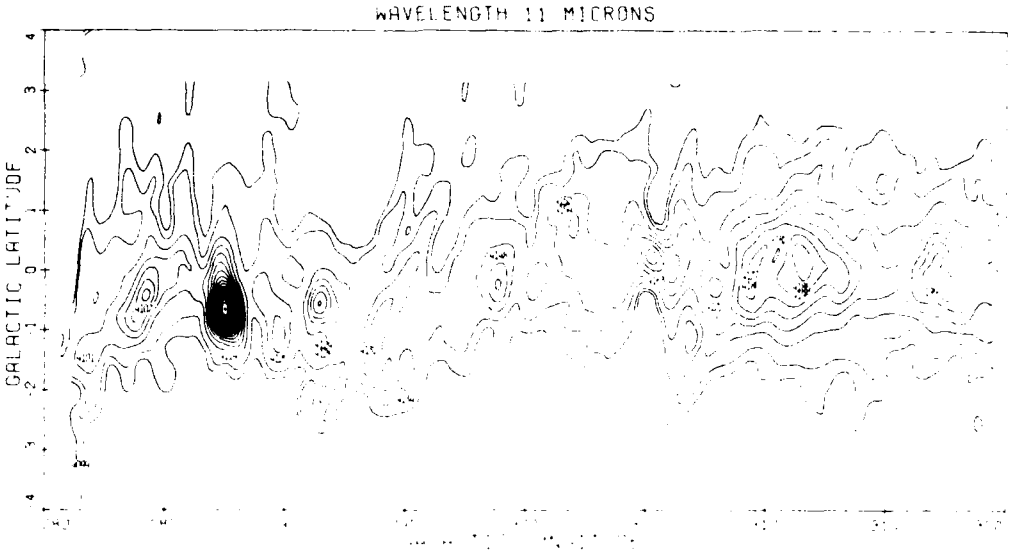

Figure 28. 11-μm Contour Map Along the Galactic Plane from 280° to 320° Longitude. This is an expanded version of the 11-μm map in Figure 27. The contour levels are in units of 10^{-11} W cm^{-2} μm^{-1} sr^{-1}. The AFGL source numbers of those sources associated with prominent extended objects in the map are also shown. Inadequate baseline correction produced the "pinching" of the contour around AFGL 4163, $\ell \sim 305^{o}$

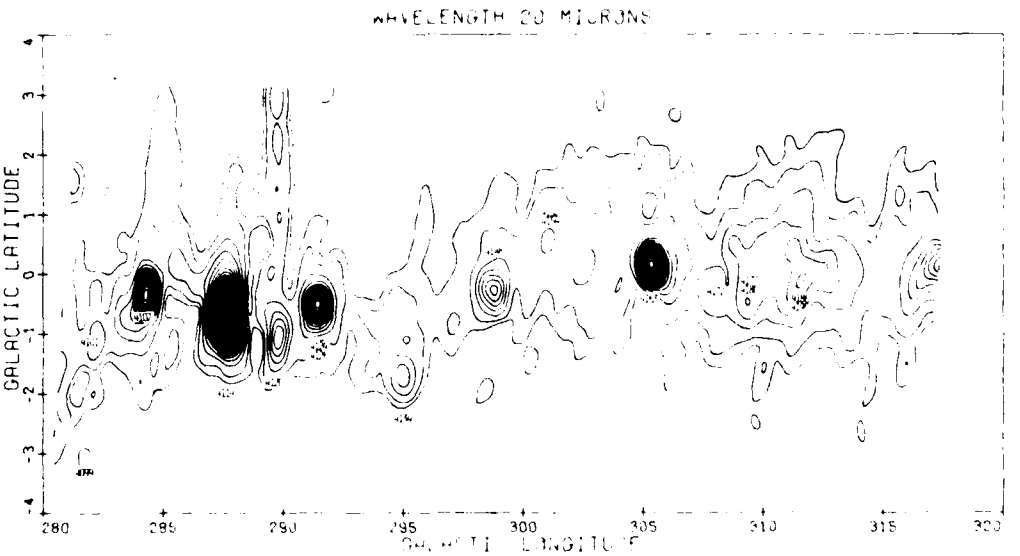

Figure 29. The 20-μm Map of the Galactic Equator Region Between 280° and 320° Longitude. The units for the contour levels are 10^{-11} W cm^{-2} μm^{-1} sr^{-1}. The numbers refer to associations with AFGL catalog sources. The wings at positive latitudes from 285° to 290° are due to baseline problems in the measurements.

Table 5. List of Extended Sources in the Region $280^{\circ} \lesssim \ell \lesssim 320^{\circ}$

ℓ	b	11 μm*	20 μm*	27 μm*	Θ_ℓ	Θ_b	AFGL	Associations	Comments
$283.^{\circ}6$	$-0.^{\circ}7$	2	2	2	$0.^{\circ}7$	$0.^{\circ}4$		RCW 48	Peak at 27 μm
282.3	-1.2	6	3	5	1.2	0.7	4101	RCW 46	
284.2	-0.4	14	16	11	1.0	0.8	4107	RCW 49, NGC 3247	11-μm emission also contains AFGL 4103 (RCW 48 + NGC 3199)
286.0	0.6	2	1	3	1.0	0.6		RCW 51	Peak in 27 μm
287.5	-0.7	39	40	64	1.6	1.6	4114	η Car, RCW 53	11-μm and 20-μm saturated, values are close to being correct as the smoothing routine also interpolates
289.8	-1.2	8	6	8	1.3	1.0	4120	RCW 54, NGC 3503	11 μm includes AFGL 4122
291.5	-0.4	11	14	25	1.3	0.9	4126	RCW 57, NGC 3603	
							4124	NGC 3581	
293.6	-1.4	9	1	3	1.2	0.9	4132	RCW 60, IC 2872	
295.1	-1.7	5	3	4	1.3	0.7	4134	RCW 62, IC 2948	
298.8	-0.4	8	6	6	1.5	1.0	4148		
300.4	-0.2	3	1	2	0.8	0.7			
301.2	0.9	2	1	2	0.7	0.5		RCW 66+68	
302.0	0.7	5	2	1	1.6	0.8	4154	RCW 65	
303.2	1.6	3	1	3	1.0	0.6		RCW 71+72+73	Source defined by 11- and 27-μm
305.3	0.2	12	19	30	2.0	1.0	4163	RCW 74	peaks
							4165		
307.8	-0.2	7	2	2	0.8	0.6	4172		
308.8	0.4	2	2	3	0.7	0.6	4174	RCW 79	
309.3	-0.5	2	3	2	0.6	0.4	4177	RCW 80	Source defined by 20- and 27-μm
309.8	0.3	8	3	4	1.0	0.5	4182		peaks
							4185		
311.3	0.1	13	4	4	5.0	2.0	4188		
							4190		
311.6	-0.5	4	3	2	1.0	0.6	4189	RCW 83	Source defined by 27-μm peak
							4199		
316.7	-0.2	6	8	6	2.0	0.1	4200		
							4204		

*$\times 10^{-11}$ W cm^{-2} μm^{-1} sr^{-1}

References in Association Column
RCW = Rodgers, Campbell and Whiteoak (1960)

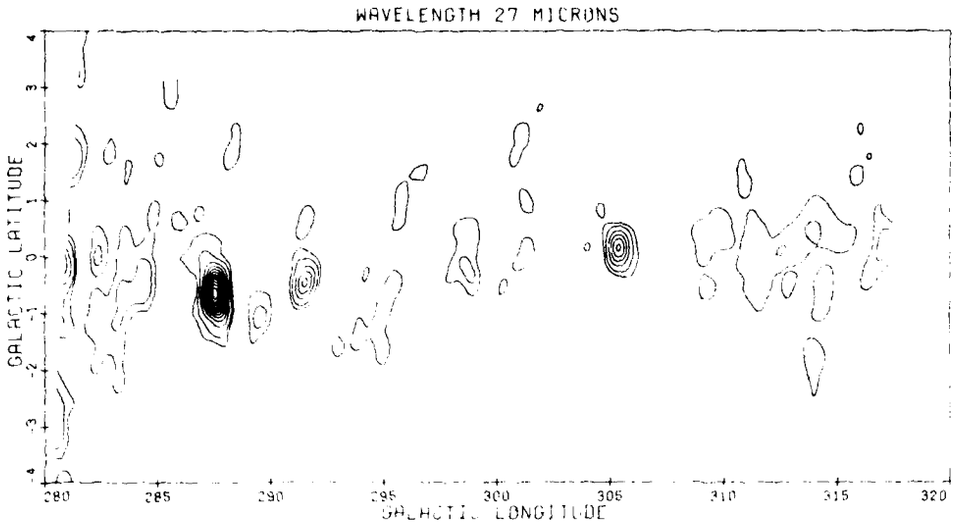

Figure 30. An Expanded Version of the 27-μm Map in Figure 27

emission from the galactic plane extends down to about 298° longitude where it becomes merged with a general background which appears to surround the large HII regions in the area between 280° and 295° longitude. Possibly this background is from the material in the Sagittarius-Carina arm which lies in this direction.

The ratio of the 11:20-μm emission is similar to that found for the complementary latitudes on the other side of the galactic center. A constant ratio of about 4 is found between 298° and 320° longitude along the galactic equator. This ratio is of the order of 2 for longitudes less than 295°.

6. DISCUSSION

The mid-infrared diffuse emission within 5° of the galactic plane is divided into three distinct components. A number of discrete extended sources were observed at 11, 20, and in the limited regions surveyed, 27μm. Almost all these discrete sources can be associated with either HII regions or dust clouds. A significant fraction of these objects (35 percent) are not correlated with entries in the AFGL catalog, particularly in the region $100^{\circ} < \ell < 240^{\circ}$. These sources have low surface brightnesses, relatively shallow intensity gradients and, consequently, were filtered out by the AC coupling of the electronic bandpass of the system. These results imply that the proportion of HII regions which contributes to the mid-infrared background needs to be increased 25 to 35 percent over what is derived from the contents of the AFGL catalog.

The discrete sources are observed against a large scale diffuse mid-infrared emission for longitudes less than 90° from the galactic center. This diffuse emission appears to be composed of two distinct backgrounds. The first, exhibits approximately constant surface brightness at 11 and 20 μm along the galactic equator from 10° to 30° longitude, then falls with increasing longitude reaching the limits of detection in either color at 60° to 68° longitude. A similar decline in surface brightness is also found at the equivalent negative longitudes. This emission is characterized by an almost constant intensity ratio (I_{11}/I_{20}) of 4 which is equivalent to a magnitude color difference, $m_{11} - m_{20} \sim 1.0$ magnitudes or an integrated in-band color temperature of 450° to 500°K.

A different diffuse component of emission is evident in the regions, $70^{\circ} < \ell < 85^{\circ}$ and $280^{\circ} < \ell < 295^{\circ}$. These longitudes are in the general directions of the Perseus external spiral arm and the Sagittarius-Carina spiral arm, respectively. The intensity ratio in both these areas is about 2 to 2.5. The magnitude color difference is about 1.8 magnitude which is equivalent to an integrated in-band color temperature of 250°K. Thus these regions are notably redder than those closer to the galactic center.

The measured surface brightness along the galactic is shown in Figures 31, 32 and 33 for the 4, 11 and 20-μm spectral bands, respectively, for an in-plane resolution of about $0.^{\circ}7$. An almost constant surface brightness is measured between 10 and 30° in longitude, with values of 20 ± 5, 12 ± 2, and $3 \pm 1 \times 10^{-11}$ W cm^{-2} μm^{-1} sr^{-1} at 4, 11 and 20 μm, where the error is the uncertainty of the average. These values are systematically too low by an amount equal to the background level at the limits adopted for the extent of the mid-infrared emission. A zero background level was assumed external to these limits.

The 11 to 20 μm color intensity of 4 was found to extend out to $\ell \sim \pm 60^{\circ}$. Over the region of 10° to 30° longitude along the galactic equator, this emission can be fit by 500°K black-body emission with a dilution factor of 2.3×10^{-8}. This agreement is fortuitous for, as we shall see, the majority of the 4-μm background is due to late type giant stars, while other sources of mid-infrared emission are required to explain the 11- and 20-μm observations.

A straightforward, albeit naive, accounting of the mid-infrared may be obtained by extrapolating the 2.4-μm balloon-borne diffuse measurements. The diffuse galactic background at 2.4 μm is assumed to be due to the integrated intensity of all the many stars in the large field of view used on these experiments. Further, the composition of these stars is assumed to be the same mix of spectral types as in the solar neighborhood. The spectroscopic studies of the Two Micron

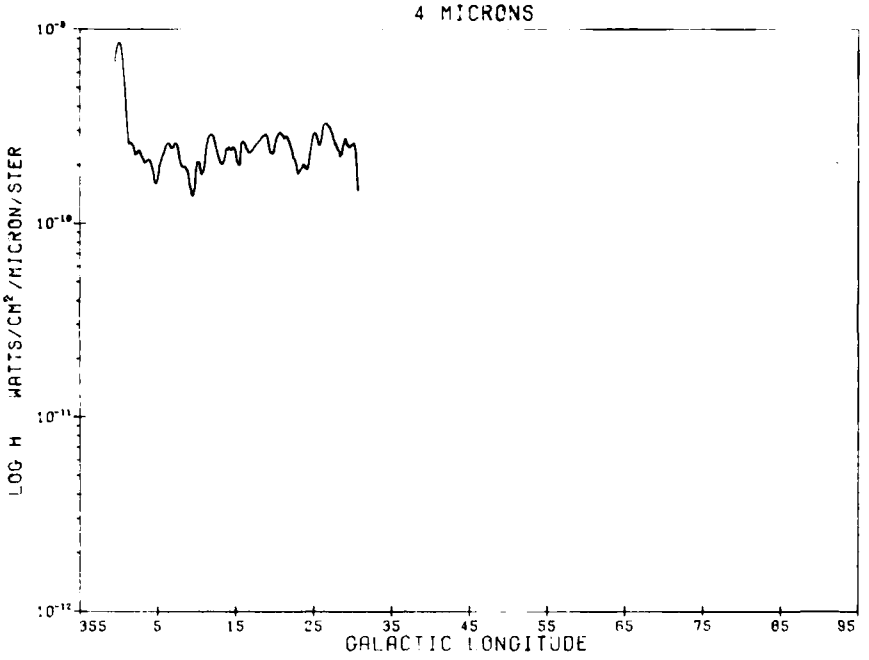

Figure 31. The 4-μm Surface Brightness Along the Galactic Equator. Values are taken from the data in Appendix A and, consequently, have a resolution of about $0.^{O}8$ in longitude. The noise level is about 10^{-10} W cm^{-2} μm^{-1} sr^{-1}

Sky Survey (Neugebauer and Leighton)[25] performed by Grasdalen and Gausted,[29] Vogt[30] and Hansen and Blanco[31] show that 70 percent of the sources brighter than an apparent magnitude of 3.0 at 2.2 μm are M giant stars. Further, the mode of spectral types is M5 to M6 with half of all sources in the survey having spectral types within two subclasses of this. The stellar content of the background is assumed to be due to M5-M6 giants which have an infrared color temperature of $2500^{O}K$. This approximation is in agreement with the findings of Harris and Rowan-Robinson[32] for the subclass of sources in the AFCRL catalog (Walker and

29. Grasdalen, G.L., and Gausted, J.E. (1971) A Comparison of the Two-Micron Sky Survey with the Dearborn Catalog of Faint Red Stars, Astronom. J. 76:231.

30. Vogt, S.S. (1973) Low Dispersion Spectroscopic Classification of the Unidentified Sources in the Two Micron Sky Survey, Astronom. J. 78:389.

31. Hansen, O.L., and Blanco, V.M. (1975) Classification of 831 Two-Micron Sky Survey Sources South of $+5^{\delta}$, Astronom. J. 80:1011.

32. Harris, S., and Rowan-Robinson, M. (1977) The Brightest Sources in the AFCRL Survey, Astronomy and Astrophysics 60:405.

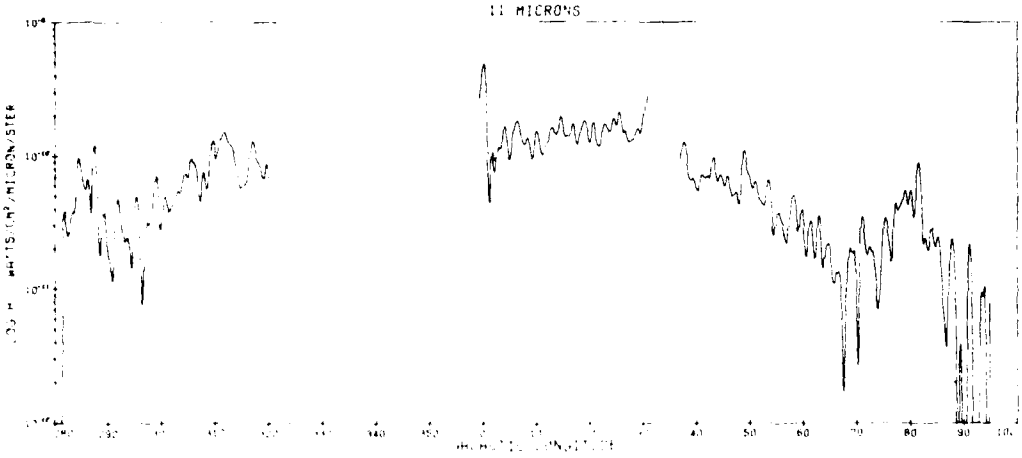

Figure 32. The 11-μm Surface Brightness Measured Along the Galactic Plane. The resolution is about $0.^{\circ}7$ in longitude. The measurement uncertainty is about 5×10^{-12} W cm^{-2} μm^{-1} sr^{-1} with about 5 times that value in the longitude region $1^{\circ} < \ell < 5^{\circ}$

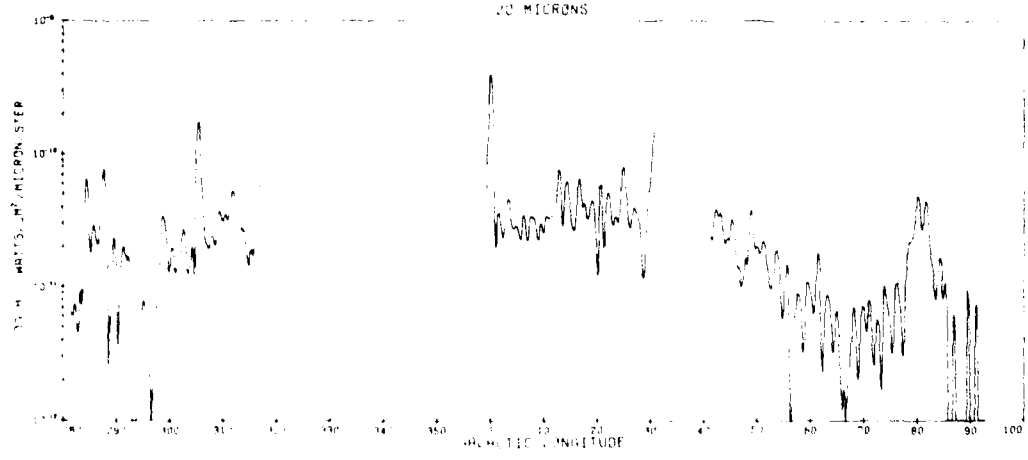

Figure 33. The 20-μm Surface Brightness Measured Along the Galactic Plane. The measurement error is estimated to be about 3×10^{-12} W cm^{-2} μm^{-1} sr^{-1}

Price)[1] they classify as stars. Harris and Rowan-Robinson[32] also found that for their subclass of stars that, in general, no excess emission is evident at 4.2 μm while on the average 0.6 and 1.1 magnitudes of infrared excess exists, at 11 and 20 μm, respectively. Gerhz et al[13] also obtained a mean color excess m(4.8 μm) - m(11.4) of 0.6 to 0.7 magnitudes on sources selected from the AFGL catalog, which they classify as stars.

The assumed background is, therefore, composed of black-body radiators with a characteristic temperature of 2500°K which have excesses at 11 μm and 20 μm, respectively, of 1.75 and 2.75 over the flux obtained by extrapolating along the black-body curve. The surface brightness at 4, 11 and 20 μm are then extrapolated to be 0.28, 0.02 and 0.003, respectively, times that at 2.4 μm if effects of interstellar extinction are not important. The observed ratios are, in sequence, 0.33, 0.20 and 0.05.

Oda et al[21] and Okuda, Maihara, Oda and Sugiyama[20] determined that the surface brightness at 2.4 μm along the galactic plane has been dimmed by about a factor of 4 within 8° of the galactic center and halved at $\ell \sim 25^{\circ}$, due to interstellar extinction. The absorption coefficient at 4.2 μm is estimated to be about half that at 2.4 μm, that is, $A_{4.2} \sim 0.5\, A_{2.4}$, from van de Hulst curve 15 given by Johnson[33] and from the analyses of Becklin, Mathews, Neugebauer and Wilner.[34] The difference in interstellar extinction between 2.4 μm and 4.2 μm would bring the calculated and observed surface brightness into even better agreement.

The situation at the longer wavelengths is not as clear. The van de Hulst curve 15 predicts extinction coefficients at 11 and 20 μm which are a fifth and a tenth that at 2.2 μm, respectively, but the analyses of Becklin et al lead to values of $A_{11} \sim A_{22}$ and $A_{20} \sim 0.3\, A_{2.2}$. At best, the predicted stellar background at 11 and 20 μm underestimates that observed by an order of magnitude and additional sources of mid-infrared emission are required.

Harris and Rowan-Robinson[32] have divided the contents of a "reliable" subset of the AFCRL catalog into three categories based upon the 4, 11 and 20-μm survey photometry. These classes are: "stars" with m(4)-m(11) < 2.0, "circumstellar dust shells" with m(4)-m(11) $\geq$ 2.0 and m(11)-m(20) < 2.0, and "dust clouds" which have m(4)-m(11) $\geq$ 2 and m(11)-m(20) $\geq$ 2. The "dust clouds" are almost chiefly

---

33. Johnson, H.L. (1968) Interstellar Extinction in Nebulae and Interstellar Matter, Vol. VII of Stars and Stellar System, Middlehurst and Aller, ed., University of Chicago, Chicago, p. 167.

34. Becklin, E.E., Mathews, K., Neugebauer, G., and Wilner, S.P. (1978) Infrared Observations of the Galactic Center. IV. The Interstellar Extinction, Astrophys. J. 220:831.

composed of HII regions (Rowan-Robinson).[35] Thus, these two classes of objects are markedly brighter at 11 and 20 μm than at 4 μm.

Harris and Rowan-Robinson[32] found that in the subset of objects they selected from the AFCRL catalog, the "circumstellar shells" and "dust clouds" are significantly more numerous above the flux cutoff of m(11) = -2.0 and m(20) = -4.0. These excesses are increased if account is taken of the revisions in the AFGL catalog (Section 9 of Harris and Rowan-Robinson).[32] There are roughly 41 sources brighter than m(11) = -2.5 and m(20) = -4.0 in the AFGL catalog if the source counts are normalized to π steradians. Assuming that a typical star has colors of m(4)-m(11) = 0.6 and m(4)-m(11) = 1.1, one notes that the 4-μm source counts predict that 7.5 stars contribute to the count at 11 μm and 3.5 at 20 μm. The nonstellar objects are thus 5.5 times more numerous than stars at 11 μm and 12 times at 20 μm. If these sources contribute to the infrared background in the same proportions down to very low levels, then this could account for about a third of the observed diffuse emission at 11 and 20 μm.

A somewhat more complex, multicomponent model of the mid-infrared background was developed by Walker and Price based upon the content of the AFCRL catalog (Walker and Price).[1] This model assumes that the space density of sources vary in the same fashion as that found by Hidajat and Blanco[38] for late M giants in the direction of the nuclear bulge. Specifically

$$D(R, z) = \frac{n(0, 0)\, R_c^2}{(R_c^2 + R^2)}\; e^{-z^2/2\sigma^2} \qquad (8)$$

The distance, in cylindrical coordinates, from the galactic center and height above the plane are given by the variables R and z, respectively; R_c is the characteristics size of the core region. The parameters σ and n(0, 0) are the scale height of the disk and central density of the class of sources in question. These values are either adopted or derived, along with the intrinsic luminosity, for each component of the model. A value of 3 kpc for R_c was selected as giving a reasonable fit to the galactic rotation curve if the mass distribution interior to the sun is given by Eq. (8). The ratio of source densities between the galactic center and the solar neighborhood, is six times greater than that found by Hidajat and Blanco.[36]

---

35. Rowan-Robinson, M. (1979) Clouds of Dust and Molecules in the Galaxy, Astrophys. J. 234:111.

36. Hidajat, B., and Blanco, V.M. (1968) Distribution of Giant M Stars in the Galactic Disk, Astron. J. 73:712.

The AFCRL catalog was divided into two subsets, one composed of late type giant stars with a value of σ = 450 pc taken from Hidajat and Blanco;[36] the other is a collection of objects confined to the disk (for example, compact HII regions, supergiants and so on) with an assumed σ = 100 pc. The catalog limits were not faint enough to see out of the plane of giant stars, which is in agreement with, Hughes[37] and the fact that in general only the reddest sources in the TMSS with K > 1.5 were included in the AFCRL catalog. The intrinsic luminosities of the disk sources are large enough that these sources have a pure disk population. The volume emissivity of each class of sources was found by a least squares solution to the source counts in each color as a function of irradiance, assuming a purely spherical distribution for the giants and a pure disk distribution for the remainder, that is,

$$N(H_\lambda) = a_1 H_\lambda^{-3/2} + a_2 H_\lambda^{-1}$$

where $N(H\lambda)$ is the number of sources in color (λ) brighter than an irradiance H_λ and the volume emissivities near the sun is a_1 for the giants and a_2 for the disk population.

The volume emissivities then derived lead to the following mean colors for each class: m(4)-m(11) = 2.1 and m(11)-m(20) = 1.3 for giants, m(4)-m(11) = 2.9 and m(11)-m(20) = 1.8 for the disk sources. These colors are consistent with those of Harris and Rowan-Robinson[33] if the sources in the "dust shell" category are distributed among the other two subsets.

The density gradient derived from Eq. (8) in the solar vicinity is about half those obtained from the exponential volume emissivity models proposed by Hayakawa, Ito, Matsumoto and Uyama[38] and Maihara et al[39] to account for the observed diffuse 2.4 μm emission. These exponential models also include the effects of interstellar extinction taken to be proportional to the observed galactic distribution of molecules. The apparent volume emissivity of the exponential models is reduced to within a factor of 2 of that in Eq. (8) if account is taken of the interstellar extinction interior to the sun.

---

37. Hughes, E.C., Jr. (1969) The Luminosities and Spatial Distribution of Stars Detected on a Two Micro Sky Survey, Ph.D. dissertation, California Institute of Technology.

38. Hayakawa, S., Ito, K., Matsumoto, T., and Uyama, K. (1977) Overall Distribution of Infrared Sources in Our Galaxy, Astronomy and Astrophysics 58:325.

39. Maihara, T., Oda, N., Sugiyama, T., and Okuda, H. (1978) 2.4-Micron Observation of the Galaxy and the Galactic Structure, Publ. Astron. Soc. Japan 30:1.

Table 6 compares the observed surface brightnesses along the galactic plane at various colors and those calculated by means of Eq. (8). The columns are the respective surface brightnesses at the various labeled longitudes. The first row of Table 6 represents the 2.4 μm observed surface brightness from Hayakawa et al[23] and Ito et al.[40] The model values derived from the work of Krassner,[41] Krassner, Hilgeman and Bressenden,[42] Leisawitz and Krassner[43] are listed in the second row. This work uses a variation of Eq. (8) and derives the model parameters from the Two-Micron Sky Survey (Neugebauer and Leighton).[25] The model results have been scaled to account for the small shift in wavelength and to adjust the absolute magnitude and space density to more realistic values. The next three rows give, respectively, the observed 4-μm surface brightness, the model values from Eq. (8) given by Greenebaum[44] and the model values increased at $\ell = 20^{\circ}$ and 30° in the same proportions as those required at 2.4 μm to bring the observed and model values into agreement. This enhancement is a crude approximation to account for the 5 kpc ring of additional stellar sources proposed by Maihara.[45] The Greenebaum article corrects roundoff errors in some of the integration algorithms used by Walker and Price.[15] The equivalent comparison between the observed and calculated surface brightnesses at 11 μm are given in the next three rows and the 20-μm values are presented in the last three rows.

Table 6. Comparison of the Observed Surface Brightnesses with Those Predicted from the Walker-Price Model*

	ℓ =	0°	10°	20°	30°	45°	60°
2.4 μm	Obs	17	7	6	6	2	1.2
	Model	7	6	4	3	2	1.5
4.2 μm	Obs	8.5	2	2.5	2.6		
	Model	2.5	2.1	1.6	1.1	0.8	0.6
		2.5	2.1	2.4	2.2		
11 μm	Obs	4.8	1.7	1.3	1.5	0.6	0.1
	Model	0.4	0.4	0.3	0.2	0.15	0.1
		0.4	0.4	0.5	0.4		
20 μm	Obs	3.9	0.3	0.2	0.4	0.3	0.1
	Model	0.2	0.15	0.1	0.1	0.05	0.04
		0.2	0.15	0.15	0.2		

*In units of 10^{-11} W cm^{-2} μm^{-1} sr^{-1}

Because of the large number of references cited above, they will not be listed here. See References, page 69.

Very good agreement between the model and observations is apparent at the short wavelengths, while the model underestimates the 11- and 20-μm observations by a factor of 2 to 3. A qualitatively similar result was obtained earlier by simply extrapolating. Thus, although late type giant stars are significant contributors to the infrared background, accounting for almost all the diffuse emission shortward of 5 μ, other sources dominate at 11 and 20 μm. The AFGL catalog contents show that much of the observed 11- and 20-μm background is due to stars with deep circumstellar shells, bipolar nebulae and compact HII region.

There is some evidence for the hypotheses that there is a significant diffuse component of the background at 11 and 20 μm. Strom, Strom, Grasdalen and Capps[46] found a reasonably good correlation between the 11-cm fluxes measured by Altenhoff, Downes, Good, Maxwell and Rinehart[47] and the 11 and 20-μm magnitudes from the AFGL catalog on the HII regions common to both lists. The relationship is given in Figures 1 and 2 of Strom et al[46] and can be expressed as $2.5 \log S(11\ cm) = 0.5 - m(11\ \mu m) = -2 - m(20\ \mu)$ or, in terms of flux units $S(11\ \mu m) = 3S(20\ \mu m) = 20\ F(11\ cm)$. The magnitude difference of the 59 sources studied by Rowan-Robinson[35] is $m(11)-m(20) = 2.9 \pm 0.5$, in agreement with the relationship derived above. Lebofsky, Sargent, Kleinmann, and Rieke[48] have argued that the 11-μm flux dependence on the 11 cm values should be halved on the basis that Strom et al[46] biased their sample by preferentially selecting the brightest HII regions.

Mezger[49] and Fazio[50] find that thermal free-free and bound-free 11-cm emission becomes significant when a compact HII region becomes optically visible. Both stages of evolution have significant amounts of mid-infrared emission from the dust shell surrounding the exciting star. Some correlation between 11-cm and mid-infrared emission is, therefore, expected for these HII regions. Mezger[51] has proposed that the thermal emission measured along the galactic plane in the radio region can be explained as arising from a large, extended, low density HII region created by the overlapping Stromgren spheres of the O stars in the galactic plane which have dissipated their optical HII regions. If a continuum of evolutionary states of HII regions co-exist with the low density ionized region and a range of dust temperature occur in the low density region, then some correlation should exist between the radio flux and that in the mid-infrared.

A correlation was noted previously for the Cygnus X region between the 11 cm unresolved thermal emission observed by Wendker[28] and the mid-infrared. The mid-infrared surface brightness is expressed in terms of radio brightness

---

Because of the large number of references cited above, they will not be listed here. See References, page 59.

temperature as $I(11) \simeq 2.5I(20) \simeq 2\ T_B\ (^oK^{-1}) \times 10^{-11}$ W cm^{-2} μm^{-1} sr. In terms of flux density for the respective fields of view, the 11-cm and 11-μm fluxes are $S(11\ \mu m) \sim 13\ S(11\ cm)$ for this region, a value quite similar to that obtained by Lebofsky et al[50] for HII regions in general. If this relationship also applies to the region $10^o < \ell < 30^o$, then the 2.8°K brightness temperature along the galactic plane observed by Altenhoff et al[49] at 11 cm predicts an 11 and 20-μm surface brightness of 6 and 2×10^{-11} W cm^{-2} μm^{-1} sr^{-1}, respectively. The ratio between the 11 and 20-μm diffuse backgrounds in the Cygnus X region is higher than the average for the HII regions studied by Strom et al[46] and Rowan-Robinson,[35] $I(11)/I(20) \sim 2$ to 2.5 as opposed to $I(11) \simeq I(20)$. The high resolution map of Price[52] for this area show that the I(11)/I(20) values for the discrete AFGL sources contained therein are the same after deconvolution as are in the AFGL catalog. Thus, if either the 11 or 20-μm diffuse measurements are systematically changed, then the I(11)/I(20) ratio of the HII regions will scale similarly, preserving the discrepancy. The possibility that the deconvolution systematically scales the low frequencies differently at 20 μm than at 11 μm is countered, in part, by the fact that the color ratios measured along the ecliptic plane on the ε Sgr flight (Price, Marcotte and Murdock)[53] are as low as the physics will allow unless an exotic particle composition applies. These deconvolved measurements have a characteristic frequency of about 1 hertz. The surplus of 11 μm emission over that predicted in the region $|\ell| < 35^o$ is apparently real.

It is proposed that the diffuse infrared background shortward of 5 μm is due to stars, the majority of which are giants. About half of the galactic background observed at 11 μm and almost all that at 20 m can be explained as HII regions along the line of sight. This includes a possibly significant contribution from a large, extended low-density component. The remaining 11 and 20 μm are probably due to circumstellar shell sources plus other disk population objects.

7. CONCLUSION

About three quarters of the galactic plane has been surveyed in the mid-infrared. The observed in-plane variations of surface brightness is qualitatively very similar to measurements at other wavelengths; this includes the enhancements observed in the longitude regions $20^o < \ell < 35^o$ and $70^o < \ell < 75^o$.

---

52. Price, S.D. (1980) Medium Resolution IR-Maps of the Cygnus X Region, Bull. Am. Astron. Soc. 12 (in press).

53. Price, S.D., Marcotte, L.P., and Murdock, T.L. (1980) Infrared Observations of the Zodiacal Dust Cloud, Astronom. J. 85:765.

The 4-μm measurements are explainable in terms of the 2.4-μm balloon borne observations and both backgrounds being due to late type giant and supergiant stars. The stellar contributions at the 11 and 20 μm are about an order of magnitude lower than what is measured. The source counts of the 11 and 20-μm contents of the AFGL catalog indicate that, in the mid-infrared, objects such as stars with optically thick dust shells, bipolar nebulae and compact HII regions are extrapolated to be significant contributors to the diffuse galactic background. A large scale diffuse mid-infrared emission may also exist which is correlated with the free-free thermal emission at 11 cm.

A number of discrete, extended sources were found within 5 degrees of the galactic plane. Almost all of these objects can be associated with HII regions, although a third of them were not included in the AFGL catalog. This implies that HII are more populous objects than the catalog currently predicts.

References

1. Walker, R.G., and Price, S.D. (1975) AFCRL Infrared Sky Survey Volume I. Catalog of Observations at 4, 11 and 20 μm, AFCRL-TR-75-0373, AD A016 397.

2. Price, S.D., and Walker, R.G. (1976) The AFGL Four Color Infrared Four Color Sky Survey Catalog of Observations at 4.2, 11.0, 19.8 and 27.4 μm, AFGL-TR-76-0208, AD A034 448.

3. Price, S.D. (1977a) The AFGL Four Color Infrared Sky Survey: Supplemental Catalog, AFGL-TR-77-0160, AD A048 048.

4. Price, S.D. (1978) Extended Source Extraction from the Air Force Geophysics Laboratory (AFGL) Infrared Sky Survey Data, Proc. Soc. Photoopt. Instrum. Engrs. 156:108.

5. Price, S.D. (1977b) Extended Infrared Emission from the Galactic Plane, Bull. Am. Astron. Soc. 9(No.3), pp.

6. Price, S.D., Akerstrom, D.S., Cunniff, C.V., Marcotte, L.P., Tandy, P.C., and Walker, R.G. (1978) Aspect Determination for the AFGL Infrared Celestial Survey Experiments, AFGL-TR-78-0253, AD A067 017.

7. Price, S.D., Cunniff, C.V., and Walker, R.G. (1978) Cleanliness Considerations for the AFGL Infrared Celestial Survey Experiments, AFGL-TR-78-0171, AD A060 116.

8. Westerhout, G. (1958) A Survey of the Continuous Radiation from the Galactic System of a Frequency of 1390 Mc/s, Bull. Astron. Neth. 14:215.

9. Hoffmann, W.F., Frederick, C.L., and Emery, R.J. (1971) 100-Micron Survey of the Galactic Plane, Astrophys. J. (Letters) 170:L89.

10. Bracewell, R. (1965) The Fourier Transform and Its Application, McGraw-Hill, New York.

11. Oppenheim, A.V., and Schafer, R.W. (1975) Digital Signal Processing, Prentice Hall, Inc., Englewood Cliffs, N.J.

12. Price, S.D., and Walker, R.G. (1978) Calibration of the HiStar Sensors, AFGL-TR-78-0172, AD A061 020.

13. Gerhz, R.D., Hackwell, J.A., and Grasdalen, G.L. (1979) Infrared Studies of AFGL Sources, AFGL-TR-79-0274, AD A084 713.

14. Rudy, R.J., Gosnell, T.R., and Willner, S.P. (1979) Ground Based Measurements of Sources in the AFGL Infrared Sky Survey, AFGL-TR-79-0172, AD A081 381.

15. Sayre, C., Arrington, C.D., Eisenmann, W.L., and Merriam, J. (1976) Characteristics of Detectors Having Partially Illuminated Sensitive Areas, preprint from IRIS March, 1976, meeting on Detectors.

16. Arrington, D.C., and Eisenmann, W.L. (1973) Test Data for a 24-Element Array, Naval Electronics Laboratory Center, Report 2600-5.

17. Arrington, D.C., and Eisenmann, W.L. (1974) Test Data for a 24-Element Array, Naval Electronics Laboratory Center, Report 2610-17.

18. Rempel, G.G. (1974) Non-linear (Parabolic) Smoothing of Experimental Data, Translation from Izv. Earth Sciences, No. 3, 101.

19. Ito, K., Matsumoto, T., and Uyama, K. (1977) Infrared profile of central portion of our galaxy at 2.47 μm, Nature 265:517.

20. Okuda, H., Maihara, T., Oda, N., and Sugiyama, T. (1977) 2.4 μm Mapping of the Galactic Central Region, Nature 265:515.

21. Oda, N., Maihara, T., Sugiyama, T., and Okuda, H. (1979) Cosmic Dust in the Central Region of the Galaxy and Anomalous Infrared Source at $\ell \sim 355^{\circ}$, $b \sim -1^{\circ}$, Astron. Astrophys. 72:309.

22. Hayakawa, S., Matsumoto, T., Murakami, H., Uyama, K., Yamagami, T., and Thomas, J.A. (1979) Near IR Surface Brightness of Southern Galactic Plane, Nature 279:510.

23. Nishimura, T., Low, F.J., and Kurtz, R.F. (1980) Far Infrared Survey of the Galactic Plane, Astrophys. J. (Letters) 239:L101.

24. Hoffmann, W., Lemke, D., and Frey, A. (1978) Mapping of the Galactic Center and the Aquila Region in the Near Infrared from Balloon Altitudes, Astronomy and Astrophysics 70:427.

25. Neugebauer, G., and Leighton, R.B. (1969) Two Micron Sky Survey—A Preliminary Catalog, NASA SP-3047.

26. Campbell, M.F., Hoffmann, W.F., Thronson, Jr., H.H., and Harvey, P.M. (1980) Far-Infrared Survey of Cygnus X, Astrophys. J. 238:122.

27. Kleinmann, S.G., Joyce, R.R., Sargent, D.G., Gillett, F.C., and Telesco, C.M. (1979) An Observational Study of the AFGL Infrared Sky Survey. IV. Further Results from the Revised Catalog, Astrophys. J. 227:126.

28. Wendker, H.J. (1970) The Cygnus X Region VI. A New 2695 MHz Continuum Survey, Astron. Astrophys. 4:378.

29. Grasdalen, G.L., and Gausted, J.E. (1971) A Comparison of the Two-Micron Sky Survey with the Dearborn Catalog of Faint Red Stars, Astronom. J. 76:231.

30. Vogt, S.S. (1973) Low Dispersion Spectroscopic Classification of the Unidentified Sources in the Two Micron Sky Survey, Astronom. J. 78:389.

31. Hansen, O.L., and Blanco, V.M. (1975) Classification of 831 Two-Micron Sky Survey Sources South of +5°, Astronom. J. 80:1011.

32. Harris, S., and Rowan-Robinson, M. (1977) The Brightest Sources in the AFCRL Survey, Astronomy and Astrophysics 60:405.

33. Johnson, H.L. (1968) Interstellar Extinction in Nebulae and Interstellar Matter, Vol. VII of Stars and Stellar System, ed. Middlehurst and Aller, University of Chicago, Chicago, p. 167.

34. Becklin, E.E., Mathews, K., Neugebauer, G., and Wilner, S.P. (1978) Infrared Observations of the Galactic Center. IV. The Interstellar Extinction, Astrophys. J. 220:831.

35. Rowan-Robinson, M. (1979) Clouds of Dust and Molecules in the Galaxy, Astrophys. J. 234:111.

36. Hidajat, B., and Blanco, V.M. (1968) Distribution of Giant M Stars in the Galactic Disk, Astron. J. 73:712.

37. Hughes, E.C., Jr. (1969) The Luminosities and Spatial Distribution of Stars Detected on a Two Micron Sky Survey, Ph.D. dissertation, California Institute of Technology.

38. Hayakawa, S., Ito, K., Matsumoto, T., and Uyama, K. (1977) Overall Distribution of Infrared Sources in Our Galaxy, Astronomy and Astrophysics 58:325.

39. Maihara, T., Oda, N., Sugiyama, T., and Okuda, H. (1978) 2.4-Micron Observation of the Galaxy and the Galactic Structure, Publ. Astron. Soc. Japan 30:1.

40. Ito, K., Matsumoto, T., and Uyama, K. (1976) Observations of the Diffuse Infrared Radiation from our Galaxy at 2.4 μm, Publ. Astron. Soc. Japan, 28:427.

41. Krassner, J. (1979) Predicted 2.2 μm Celestial Backgrounds for Infrared Telescopes, Proc. Soc. Photoopt. Instrum. Engrs., Vol. 172.

42. Krassner, J., Hilgeman, T., and Brissenden (1979) Celestial Backgrounds at 2.2 Microns, Grumman Research Dept. Memorandum RM-675.

43. Leisawitz, D., and Krassner, J. (1979) Improved Two Micron Celestial Background Estimates, Grumman Research Dept. Mem. RM-682.

44. Greenbaum, M. (1977) Computer Implementation of the Walker Star Model, Research Note N-1364-3-64 Riverside Research Institute.

45. Maihara, T. (1978) On the Mass Density Distribution of the Inner Galaxy, IAU Symposium 84, The Large Scale Structure of the Galaxy, W.B. Burton, Ed., Reidel, Dordtrect, p. 381.

46. Strom, S.E., Strom, K.M., Grasdalen, G., and Capps, R.W. (1974) Infrared Observations of HII Regions in External Galaxies, Astrophys. J. (Letters) 193:L7.

47. Altenhoff, W.J., Downes, D., Goad, L., Maxwell, A., and Rinehart, R. (1970) Surveys of the Galactic Plane at 1.414, 2.695 and 5.000 GHz, Astron. Astrophys. Suppl. 1:319.

48. Lebofsky, M.J., Sargent, D.G., Kleinmann, S.G., and Rieke, G.H. (1978) An Observational Study of the AFCRL Infrared Sky Survey. III. Further Searches for AFCRL/AFGL Sources and an Evolution of the Contents of the Mid-Infrared Sky, Astrophys. J. 219:487.

49. Mezger, P.G. (1978a) Interstellar Matter in Infrared Astronomy, Setti and Fazio, Ed., Reidel, Dordtrect, p. 1.

50. Fazio, G.G. (1978) Infrared Observations of HII Regions, in Infrared Astronomy, Setti and Fazio, Ed., Reidel, Dordtrect, p. 25.

51. Mezger, P.G. (1978b) The Galactic Extended Low-Density HII Region and Its Relation to Star Formation and Diffuse IR Emission, Astron. Astrophys. 20:565.

52. Price, S.D. (1980) Medium Resolution IR-Maps of the Cygnus X Region, Bull. Am. Astron. Soc. 12 (in press).

53. Price, S.D., Marcotte, L.P., and Murdock, T.L. (1980) Infrared Observations of the Zodiacal Dust Cloud, Astronom. J. 85:765.

Appendix A

Intensity Grids for the 4, 11, and 20-μm Spectral Bands Over the Region $-0.7 \lesssim \ell \lesssim 30^{\circ}$, $|b| \leq 4^{\circ}$

This Appendix contains the intensity grids generated after the data had been smoothed in rocket azimuth at constant zenith angle and in longitude at constant latitude by an iterated, nonlinear, weighted parabolic regressive filter. The resolution is approximately $0.^{\circ}5$ in latitude and $0.^{\circ}8$ in longitude. The extensive grids listed in this Appendix are included in order to provide much better resolution than obtained from the contour plots presented in the text. This resolution is useful in separating the extended sources from each other and the diffuse background.

Table A1 lists the 4 μm observed intensities every $0.^{\circ}1$ in galactic latitude and longitude. The longitude increases across the table and every degree is appropriately labeled at the top. The latitude varies between -4° and $+4^{\circ}$, labeled at the left of the grid for every degree. The entries are in units of 10^{-11} W cm^{-2} μm^{-1} sr^{-1}. The blank entries are areas of no data, either because the region is out of bounds of the scan, or beyond the adopted source limits. The data in Table A1 have been plotted as a contour map in Figure A1.

The 11-μm intensity grid is listed in Table A2. The format is the same as for Table A1. Again the entries are in units of 10^{-11} W cm^{-2} μm^{-1} sr^{-1}. Figure A2 is the 11-μm contour map generated from the intensity grid listed in Table A2.

The 20-μm intensity grid for this region is given in Table A3. The format is the same as for Tables A1 and A2 and the entries are also 10^{-11} W cm^{-2} μm^{-1} sr^{-1}. The blank holes and stripping in the grid occurred when two or more adjacent

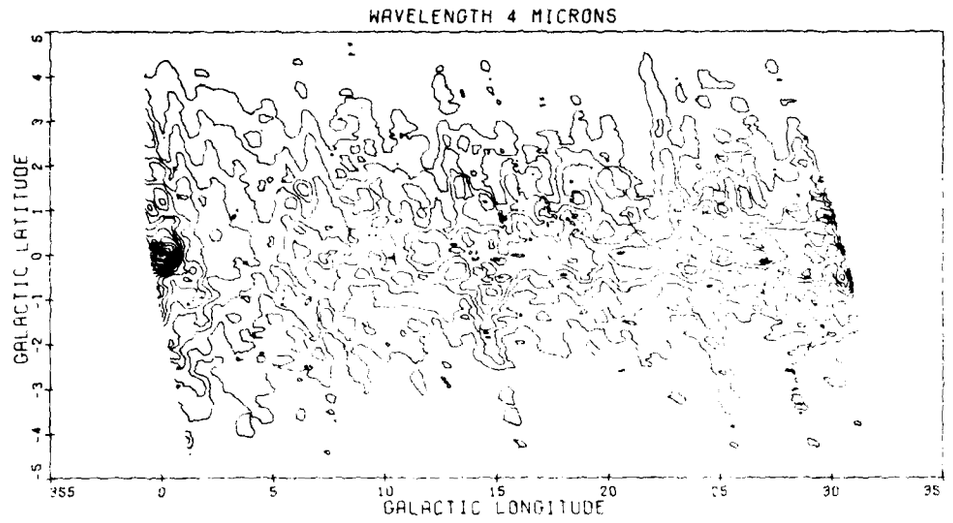

Figure A1. 4-μm Contour Map for the Region $-0.7 < \ell \lesssim 32^{\circ}$. This map was generated from the intensity grid in Table A1. The outermost contour is 5×10^{-11} W cm^{-2} μm^{-1} sr^{-1} with each succeeding contour level being an increase of 5×10^{-11} W cm^{-2} μm^{-1} sr^{-1}

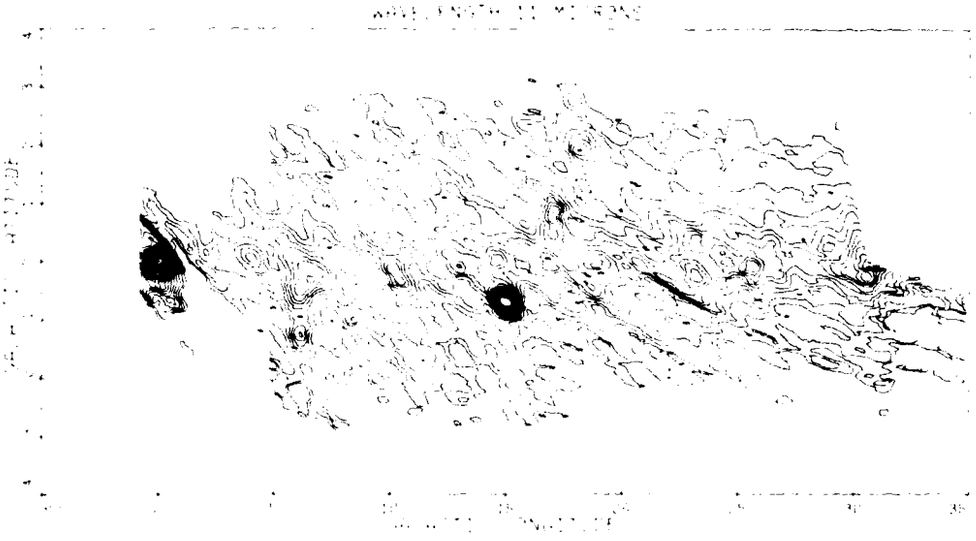

Figure A2. 11-μm Iso-Intensity Map for the Region $-0.^{\circ}7 < \ell < 35^{\circ}$. The lowest contour represents a brightness of 1×10^{-11} W cm^{-2} μm^{-1} sr^{-1}, the next level is 2×10^{-11} W cm^{-2} μm^{-1} sr^{-1} and each subsequent level is a brightness increase of 2×10^{-11} W cm^{-2} μm^{-1} sr^{-1} (1, 2, 4, 6, etc. $\times 10^{-11}$ W cm^{-2} μm^{-1} sr^{-1}). Contours in the region $\ell < 5^{\circ}$ have been limited to levels brighter than 6×10^{-11} W cm^{-2} μm^{-1} sr^{-1} due to a larger noise for the scans across this area. Highest contour shown is 5×10^{-10} W cm^{-2} μm^{-1} sr^{-1} which is less than the peak brightness of M17

Table A1. 4-μm Intensity Grid over the Region $-0.^{0}7 < \ell \lesssim 32.^{0}$ (in units of 10^{-11} W cm^{-2} μm^{-1} sr^{-1})

Table A1. 4-μm Intensity Grid Over the Region $-0''.7 < \ell \lesssim 32''$ (in units of 10^{-11} W cm^{-2} μm^{-1} sr^{-1})(Cont.)

Table A1. 4-μm Intensity Grid Over the Region $-0.^{o}7 < \ell' \lesssim 32^{o}$ (in units of 10^{-11} W cm^{-2} μm^{-1} sr^{-1}) (Cont.)

Table A1. 4-μm Intensity Grid Over the Region $-0.^{0}7 < \ell \lesssim 32^{0}$ (in units of 10^{-11} W cm^{-2} μm^{-1} sr^{-1}) (Cont.)

Table A1. 4-μm Intensity Grid Over the Region $-0.^{\circ}7 < l < 32^{\circ}$ (in units of 10^{-11} W cm^{-2} μm^{-1} sr^{-1}) (Cont.)

Table A1. 4-μm Intensity Grid Over the Region $-0.7^{\circ} < \ell < 32^{\circ}$ (in units of 10^{-11} W cm^{-2} μm^{-1} sr^{-1}) (Cont.)

Table A1. 4-μm Intensity Grid Over the Region $-0.7° \leq \ell \leq 32.0°$ (in units of 10^{-11} W cm^{-2} μm^{-1} sr^{-1}) (Cont.)

Table A2. 11-μm Intensity Grid Over the Region $-0.^{0}7 < \ell < 35^{\circ}$ (in units of 10^{-11} W cm^{-2} μm^{-1} sr^{-1})

Table A2. 11-μm Intensity Grid Over the Region $-0.7 < \ell < 35^{\circ}$ (in units of 10^{-11} W cm^{-2} μm^{-1} sr^{-1}) (Cont.)

Table A2. 11-μm Intensity Grid Over the Region $-0.7 < \ell < 35^{\circ}$ (in units of 10^{-11} W cm^{-2} μm^{-1} sr^{-1}) (Cont.)

Table A2. 11-μm Intensity Grid over the Region $-0.^{\circ}7 < \ell < 35.^{\circ}$ (in units of 10^{-11} W cm^{-2} μm^{-1} sr^{-1}) (Cont.)

Table A2. 11-μm Intensity Grid Over the Region $-0.^{o}7 < l < 35^{o}$ (in units of 10^{-11} W cm^{-2} μm^{-1} sr^{-1}) (Cont.)

Table A2. 11-μm Intensity Grid Over the Region $-0.7 < l < 35^{\circ}$ (in units of 10^{-11} W cm^{-2} μm^{-1} sr^{-1}) (Cont.)

Table A2. 11-μm Intensity Grid Over the Region $-0.^{0}7 < \ell < 35^{0}$ (in units of 10^{-11} W cm^{-2} μm^{-1} sr^{-1}) (Cont.)

Table A2. 11-μm Intensity Grid Over the Region $-0.^{o}7 < \ell < 35^{o}$ (in units of 10^{-11} W cm^{-2} μm^{-1} sr^{-1}) (Cont.)

Table A3. 20-μm Intensity Grid Over the Region $-0.^{o}7 < l < 35^{o}$ (in units of 10^{-11} W cm^{-2} μm^{-1} sr^{-1})

Table A3. 20-μm Intensity Grid Over the Region $-0.^{\circ}7 < l < 35^{\circ}$ (in units of 10^{-11} W cm^{-2} μm^{-1} sr^{-1}) (Cont.)

Table A3. 20-μm Intensity Grid Over the Region $-0.7 < \ell < 35^{\circ}$ (in units of 10^{-11} W cm^{-2} μm^{-1} sr^{-1}) (Cont.)

Table A3. 20-μm Intensity Grid Over the Region $-0.7^{o} < \lambda < 35^{o}$ (in units of 10^{-11} W cm^{-2} μm^{-1} sr^{-1}) (Cont.)

Table A3. 20-μm Intensity Grid Over the Region $-0.^{0}7 < l < 35^{0}$ (in units of 10^{-11} W cm^{-2} μm^{-1} sr^{-1}) (Cont.)

Table A3. 20-μm Intensity Grid Over the Region $-0.^{\circ}7 < \ell < 35^{\circ}$ (in units of 10^{-11} W cm^{-2} μm^{-1} sr^{-1}) (Cont.)

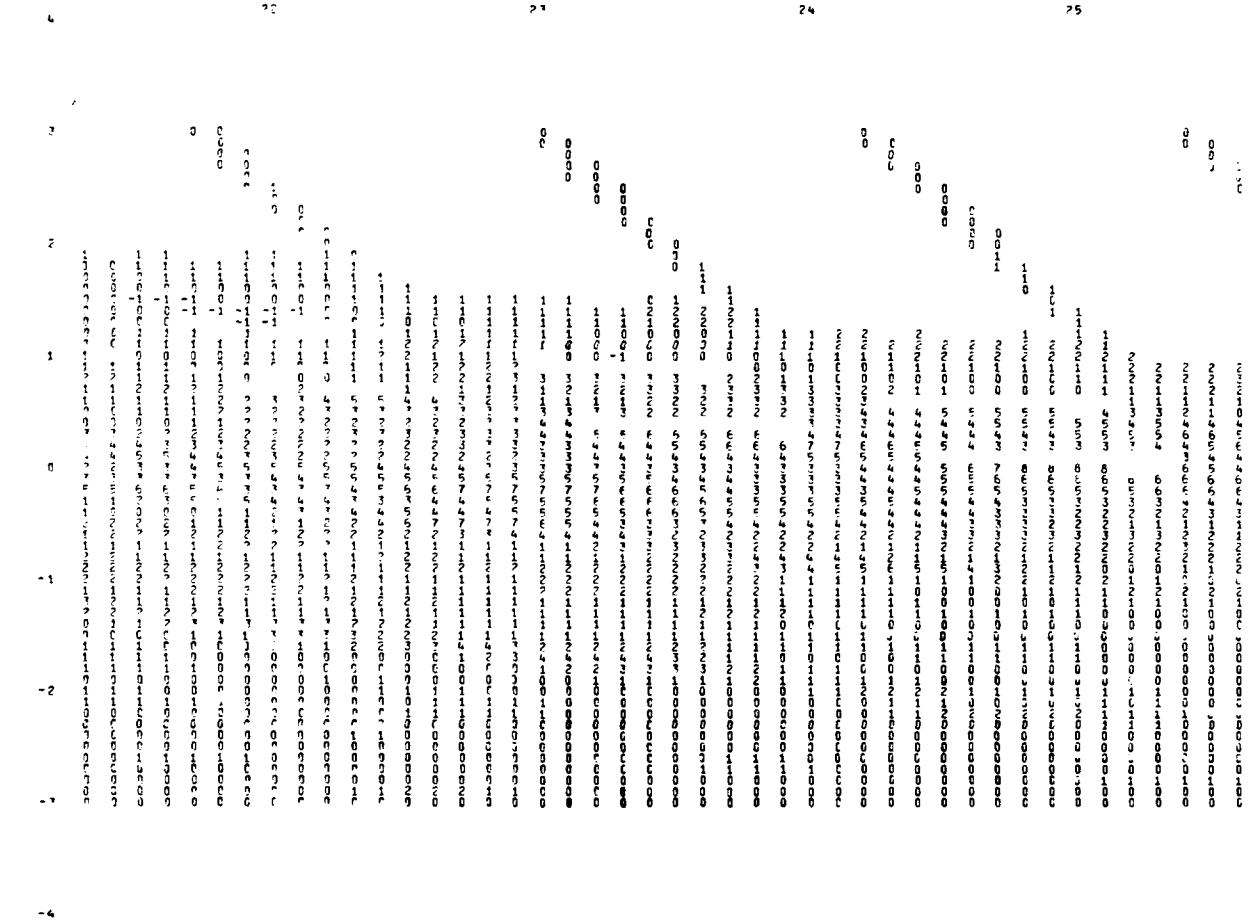

AD-A100 289 AIR FORCE GEOPHYSICS LAB HANSCOM AFB MA F/G 3/1
AN INFRARED SURVEY OF THE DIFFUSE EMISSION WITHIN 5 DEG OF THE --ETC(U)
JUN 80 S D PRICE, L P MARCOTTE
UNCLASSIFIED AFGL-TR-80-0182 NL

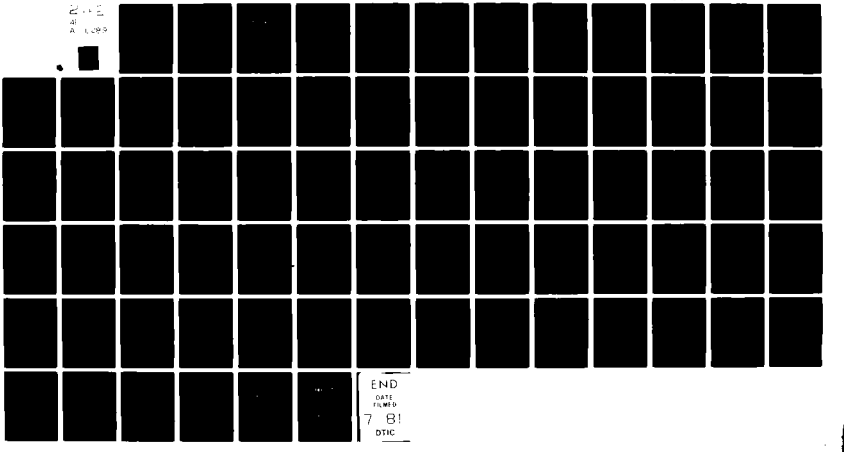

END
DATE FILMED
7 81
DTIC

Table A3. 20-μm Intensity Grid Over the Region $-0.^{\circ}7 < l < 35^{\circ}$ (in units of 10^{-11} W cm^{-2} μm^{-1} sr^{-1}) (Cont.)

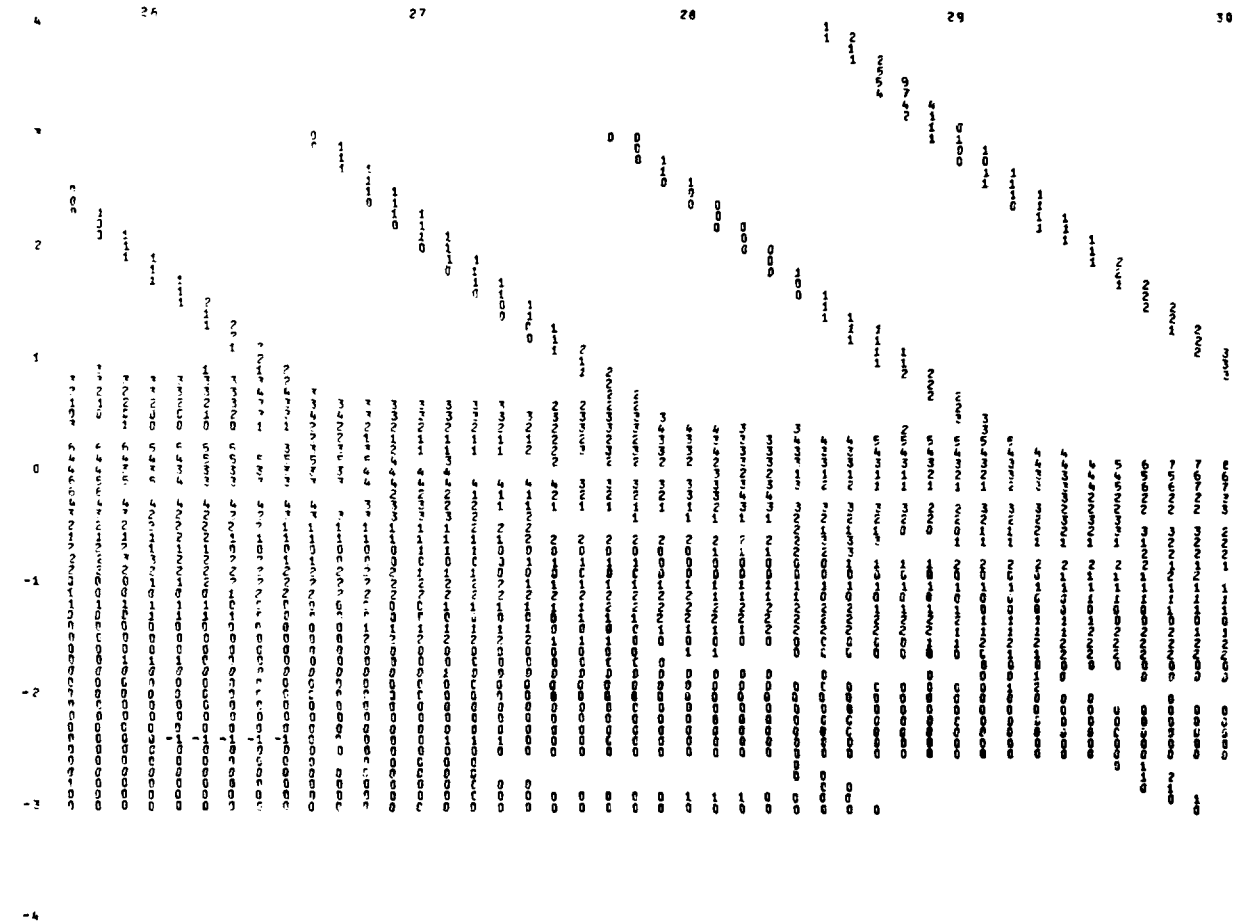

channels were missing. The data from these channels were eliminated due to nonlinear effects such as saturation, which cannot be compensated for in the restoration procedure. In the case of the α Lyr experiment, six of the 20-μm channels malfunctioned. The gaps in coverage left by these malfunctioning channels produce the stripping in the 20 μm intensity grid in Table A3 and Figure A3 at the positive latitude for longitudes greater than 20°.

Effects of noise and uncertainties associated with the restoration process are evident in Figures A1, A2 and A3. The wings in Figure A1 at $\ell \sim 22^{\circ}$ to 26° and the satellite sources at $\ell \sim 13^{\circ}$, $b \sim 3^{\circ}.5$ and $\ell \sim 16^{\circ}$, $b \sim -3^{\circ}.5$ are caused by inadequate baseline compensation. Baseline problems also cause the "pinching" of the contours in all these plots. These wings, satellite sources and pinching, all occur along lines of constant rocket zenith angle. These problems seldom show up at the second contour level or brighter.

The quality of the 20 μm data is markedly lower than that at 4 and 11 μm as may be seen from the figures. The 20-μm observations come, dominatingly, from the α CrB experiment. As pointed out in the text scans across the galactic plane from this flight were significantly longer than the overlapping α Lyr experiment. The baseline corrections were necessarily longer for this experiment and the spectral frequency content of the detection of the diffuse emission from the galactic plane was lower. The double integration used in the restoration routine produces a quadratic dependence of gross baseline errors on the duration of data length processed. These two experiments used the same telescope system and, consequently, the observations should contain the same noise characteristics. At low frequencies this noise should have been roughly proportional to $1/f$ (f = frequency) before the signal was band shaped with the high pass electronic filter. Thus, not only were the baseline uncertainties larger for the α CrB experiment than for the α Lyr flight due to the longer scan time across the galactic plane, but the lower frequency content produced by the diffuse emission from the plane resulted in a lower signal-to-noise measurement in the restored data.

Further, constant rocket zenith angles with respect to the α CrB experiment form arcs in the Figures A2 and A3. Since the observed diffuse mid-infrared emission is almost constant as a function of longitude in this region, the sections of scan which cross constant latitude lines at smaller angles will detect the emission at lower spectral frequencies which, in turn, results in a lower signal-to-noise in the restored data. The sections of the α CrB scans which are at negative latitudes are shallower, with respect to constant latitude lines, than those at positive latitudes as may be seen in Figure A3. The 11-μm map in Figure A2 more clearly shows the change in signal-to-noise in going from negative to positive latitudes. Here the data from the α CrB flight has been averaged with that from the better quality α Lyr experiment, but the striping from the α CrB experiment is

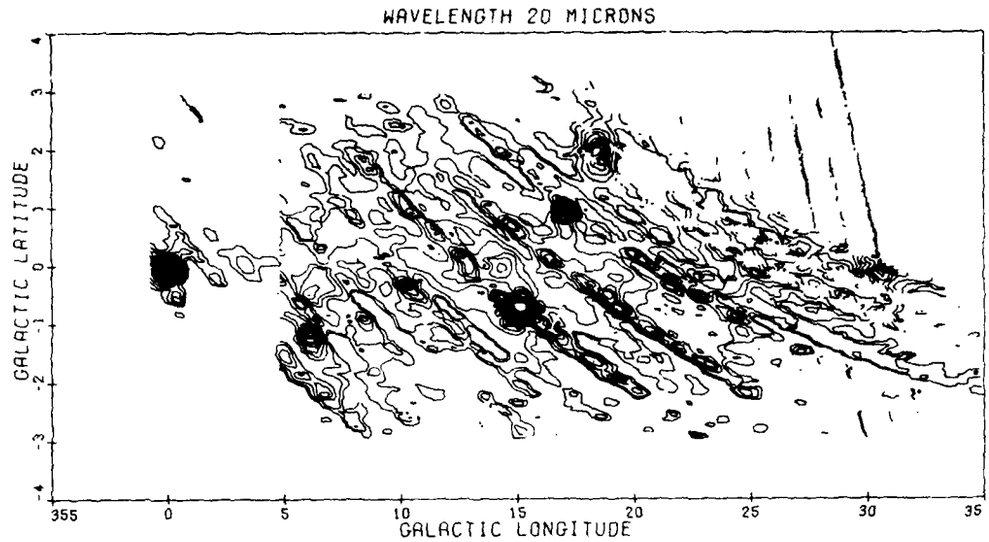

Figure A3. 20-μm Map of the Galactic Plane in the Region $-0.^{\circ}7 < \ell < 35^{\circ}$. The lowest contour is 5×10^{-12} W cm^{-2} μm^{-1} sr^{-1}, the next level is 1×10^{-11} W cm^{-2} μm^{-1} sr^{-1} and each Succeeding Level an Increase of 1×10^{-11} W cm^{-2} μm^{-1} sr^{-1} ($0.5, 1, 2, 3, 35c \times 10^{-11}$ W cm^{-2} μm^{-1} sr^{-1}). The contours in the area $\ell < 5^{\circ}$ are limited to being brighter than 2×10^{-11} W cm^{-2} μm^{-1} sr^{-1} due to the increased noise for the scans across this region. The hole in M17 is caused by limiting the brightest contour to 5×10^{-10} W cm^{-2} μm^{-1} sr^{-1}

evident at negative latitudes. Sources which are relatively small in extent on either flight, for example the galactic center, M16, M17 and NGC 6604, are restored with good fidelity on either flight.

Although the signal to noise of the restored measurements on the diffuse emission from the galactic plane depended on the latitude of the pole star, reasonably good data were obtained on all the flights. Additional smoothing of the measurements shown in Figures A1, A2, and A3 improved the signal-to-noise considerably.

Appendix B

Intensity Grids at 11, 20 and 27 μm of the Galactic Plane Between 35° and 95° Longitude

Tables B1, B2 and B3 list the 11-, 20- and 27-μm intensity grids, respectively, of the data in this longitude region after restoration, baseline correction, and the two dimensional nonlinear smoothing. The format is the same for all three tables; the longitude increases from left to right, latitude increases from -4° to $+4^{\circ}$ from the bottom to the top of the page. Every even degree in latitude and longitude is labeled. The intensity values are in units of 10^{-11} W cm^{-2} μm^{-1} sr^{-1} and are listed every $0^{\circ}.1$ in longitude and latitude. The spatial resolution of these measurements are of the order of $0^{\circ}.5$ in latitude and $0^{\circ}.8$ in longitude with sources smaller than $0^{\circ}.2$ in extent being eliminated in the data processing. Blank areas are either regions not scanned by the experiments, outside the limits adopted for the source or were created when two or more adjacent channels were eliminated due to nonlinear effects such as saturation.

The data used to compile the intensity grids were also used to generate contour maps which have the same resolution as the tables. Figure B1 shows the 11-μm contour map, Figure B2 the 20-μm map and Figure B3 the 27-μm measurements. The effects of the α CrB ($b \sim 53^{\circ}.75$) is apparent as striping at negative latitudes between 45° and 65° longitude.

Table B1. 11-μm Grid of Intensities Along the Galactic Plane Between 35° and 95° Longitude (units in 10^{-11} W cm^{-2} μm^{-1} sr^{-1})

Table B1. 11-μm Grid of Intensities Along the Galactic Plane Between 35° and 95° Longitude (units in 10^{-11} W cm^{-2} μm^{-1} sr^{-1}) (Cont.)

Table B1. 11-μm Grid of Intensities Along the Galactic Plane Between 35° and 95° Longitude (units in 10^{-11} W cm^{-2} μm^{-1} sr^{-1}) (Cont.)

Table B1. 11μm Grid of Intensities Along the Galactic Plane Between 35° and 95° Longitude (units in 10^{-11} W cm^{-2} μm^{-1} sr^{-1}) (Cont.)

Table B1. 11-μm Grid of Intensities Along the Galactic Plane Between 35° and 95° Longitude (units in 10^{-11} W cm^{-2} μm^{-1} sr^{-1}) (Cont.)

Table B1. 11-μm Grid of Intensities Along the Galactic Plane Between 35° and 95° Longitude (units in 10^{-11} W cm^{-2} μm^{-1} sr^{-1}) (Cont.)

Table B1. 11-μm Grid of Intensities Along the Galactic Plane Between 35° and 95° Longitude (units in 10^{-11} W cm^{-2} μm^{-1} sr^{-1}) (Cont.)

Table B1. 11-μm Grid of Intensities Along the Galactic Plane Between 35° and 95° Longitude (units in 10^{-11} W cm^{-2} μm^{-1} sr^{-1}) (Cont.)

Table B1. 11-μm Grid of Intensities Along the Galactic Plane Between 35° and 95° Longitude (units in 10^{-11} W cm^{-2} μm^{-1} sr^{-1}) (*Cont.*)

Table B1. 11-μm Grid of Intensities Along the Galactic Plane Between 35° and 95° Longitude (units in 10^{-11} W cm^{-2} μm^{-1} sr^{-1}) (Cont.)

Table B1. 11-μm Grid of Intensities Along the Galactic Plane Between 35° and 95° Longitude (units in 10^{-11} W cm^{-2} μm^{-1} sr^{-1}) (Cont.)

Table B1. 11-μm Grid of Intensities Along the Galactic Plane Between 35° and 95° Longitude (units in 10^{-11} W cm^{-2} μm^{-1} sr^{-1}) (Cont.)

Table B1. 11 μm Grid of Intensities Along the Galactic Plane Between 35° and 95° Longitude (units in 10^{-11} W cm^{-2} μm^{-1} sr^{-1}) (Cont.)

Table B2. 20-μm Grid of Intensities Along the Galactic Equator Between 40° and 95° Longitude (units in 10^{-11} W cm^{-2} μm^{-1} sr^{-1})

Table B2. 20-μm Grid of Intensities Along the Galactic Equator Between 40° and 95° Longitude (*units in* 10^{-11} *W cm*$^{-2}$ *μm*$^{-1}$ *sr*$^{-1}$) (Cont.)

Table B2. 20-μm Grid of Intensities Along the Galactic Equator Between 40° and 95° Longitude (units in 10^{-11} W cm^{-2} μm^{-1} sr^{-1}) (Cont.)

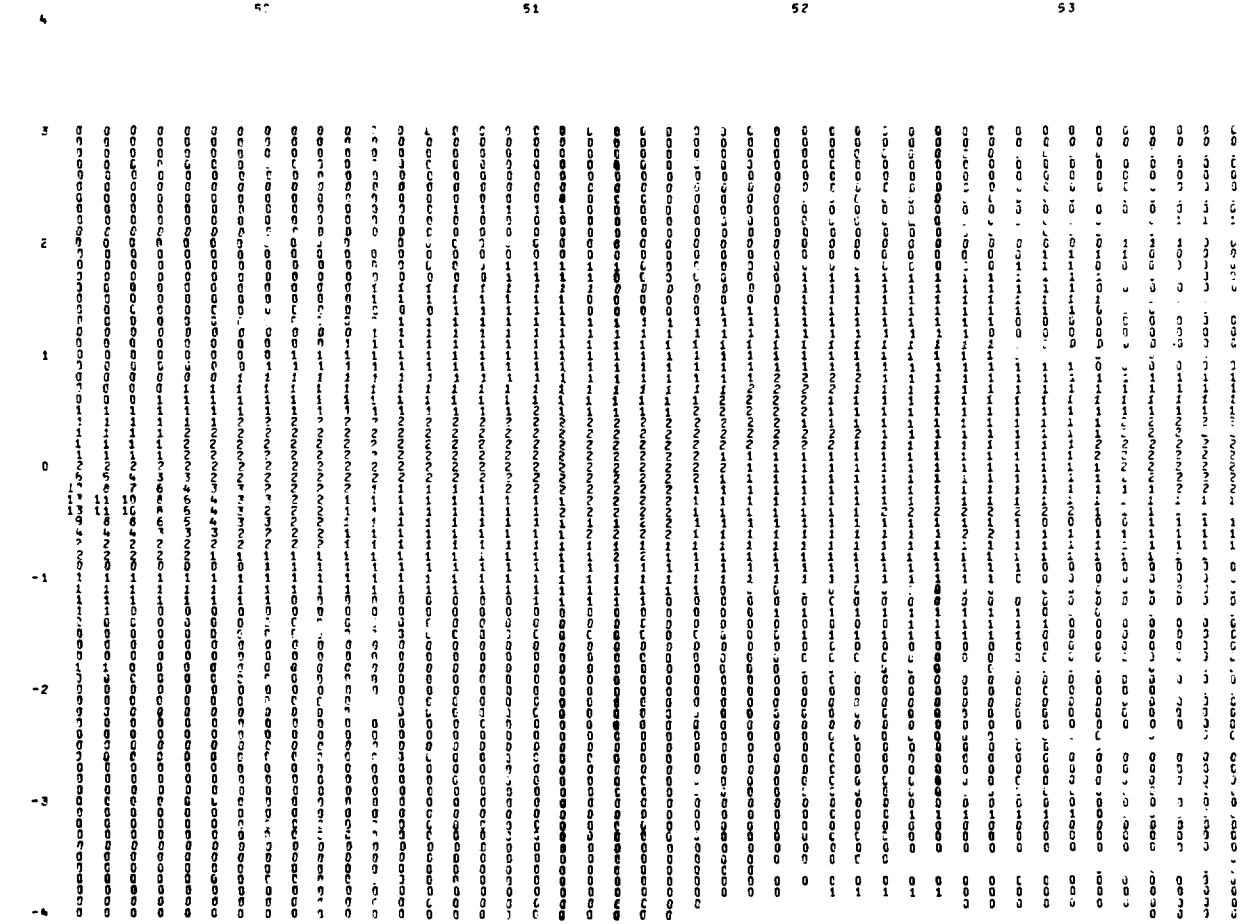

Table B2. 20-μm Grid of Intensities Along the Galactic Equator Between 40° and 95° Longitude (units in 10^{-11} W cm^{-2} μm^{-1} sr^{-1}) (Cont.)

Table B2. 20-μm Grid of Intensities Along the Galactic Equator Between 40° and 95° Longitude (units in 10^{-11} W cm^{-2} μm^{-1} sr^{-1}) (Cont.)

Table B2. 20-μm Grid of Intensities Along the Galactic Equator Between 40° and 95° Longitude (units in 10^{-11} W cm^{-2} μm^{-1} sr^{-1}) (Cont.)

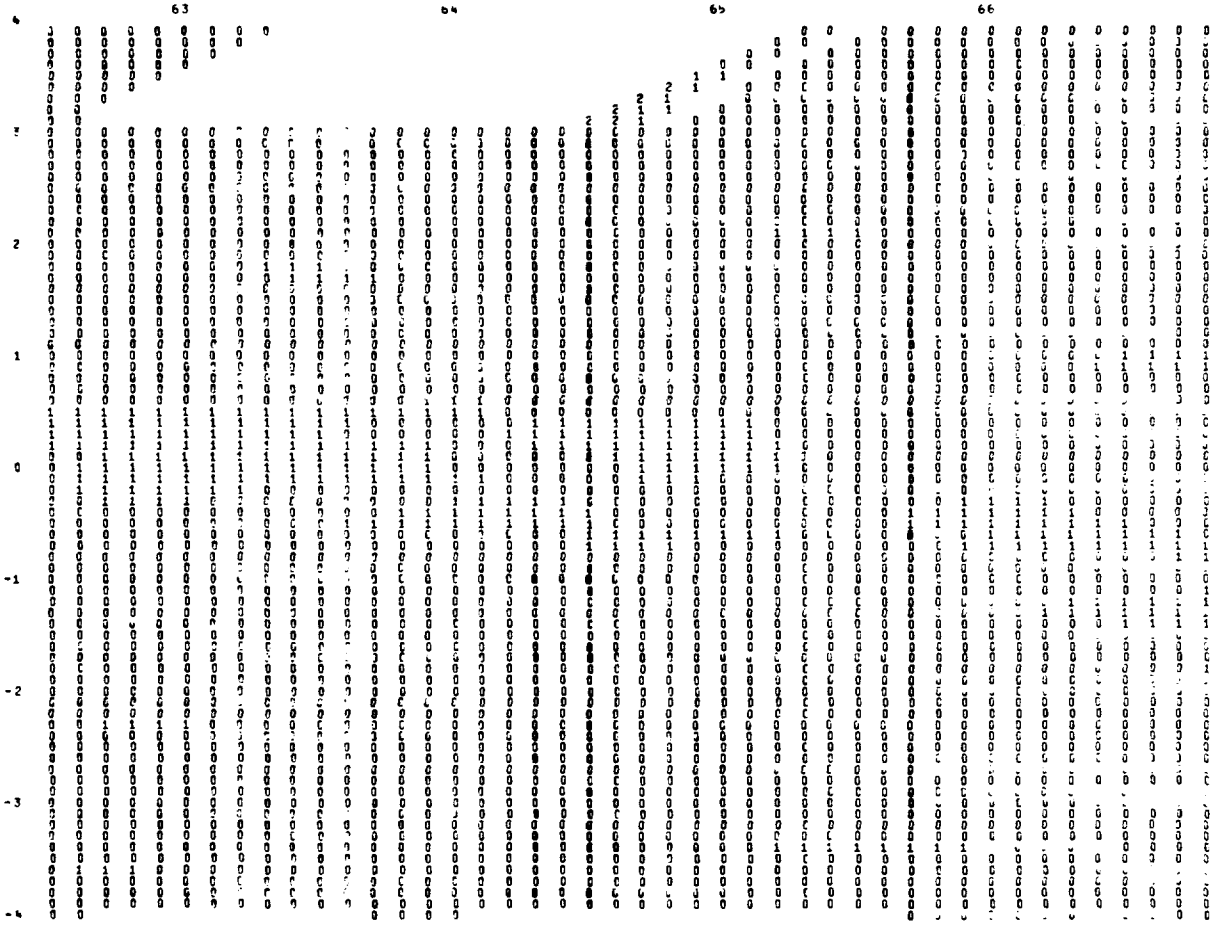

Table B2. 20-μm Grid of Intensities Along the Galactic Equator Between 40° and 95° Longitude (units in 10^{-11} W cm^{-2} sr^{-1}) (Cont.)

Table B2. 20-μm Grid of Intensities Along the Galactic Equator Between 40° and 95° I ongitude (units in 10^{-11} W cm^{-2} μm^{-1} sr^{-1}) (Cont.)

Table B2. 20-μm Grid of Intensities Along the Galactic Equator Between 40° and 95° Longitude (units in 10^{-11} W cm^{-2} μm^{-1} sr^{-1}) (Cont.)

Table B2. 20-μm Grid of Intensities Along the Galactic Equator Between 40° and 95° Longitude (units in 10^{-11} W cm^{-2} μm^{-1} sr^{-1}) (Cont.)

Table B2. 20-μm Grid of Intensities Along the Galactic Equator Between 40° and 95° Longitude (units in 10^{-11} W cm^{-2} μm^{-1} sr^{-1}) (Cont.)

Table B2. 20μm Grid of Intensities Along the Galactic Equator Between 40° and 95° Longitude (units in 10^{-11} W cm^{-2} μm^{-1} sr^{-1}) (Cont.)

Table B3. 27-μm Grid of Intensities Along the Galactic Plane Between 40° and 85° Longitude (units in 10^{-11} W cm^{-2} μm^{-1} sr^{-1})

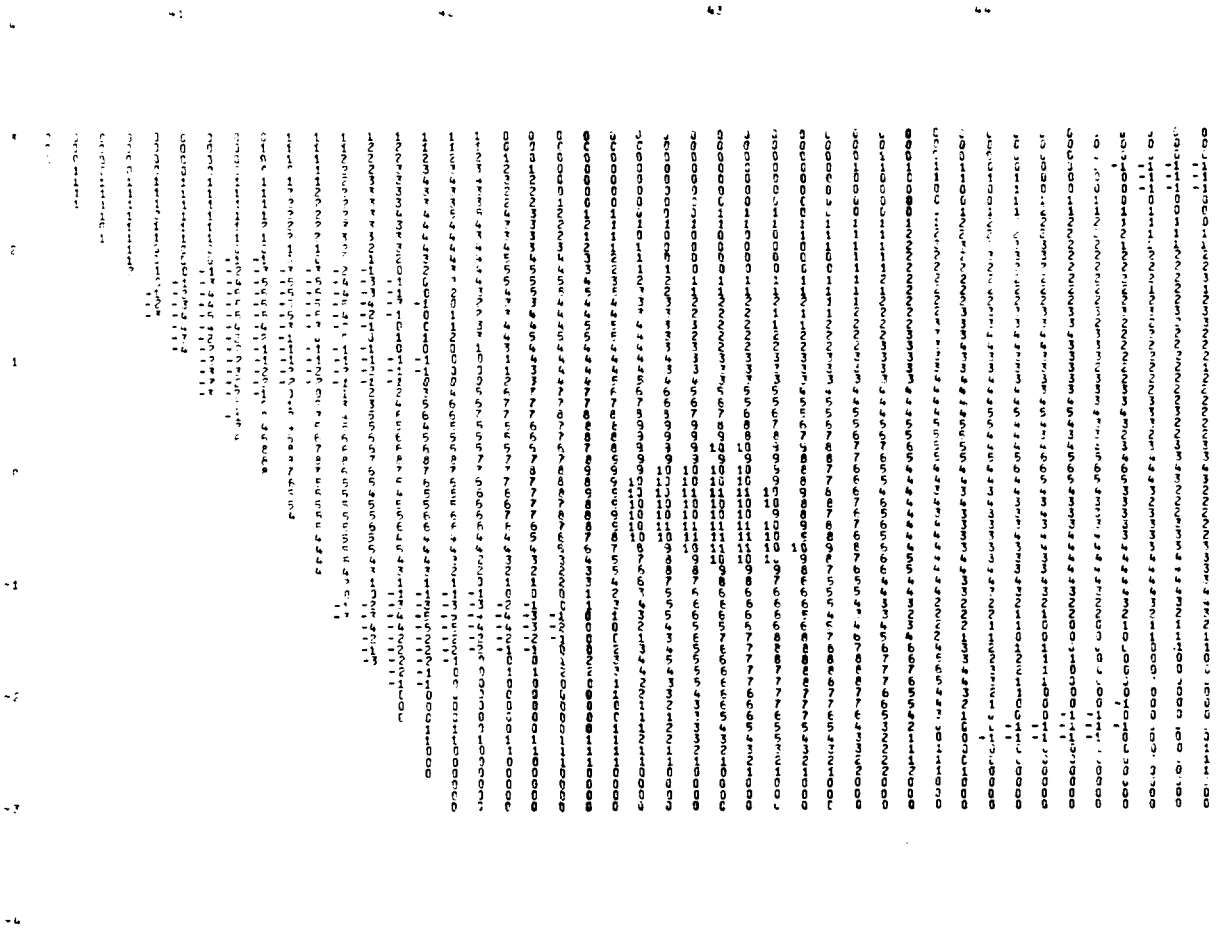

Table B3. 27-μm Grid of Intensities Along the Galactic Plane Between 40° and 85° Longitude (units in 10^{-11} W cm^{-2} μm^{-1} sr^{-1}) (Cont.)

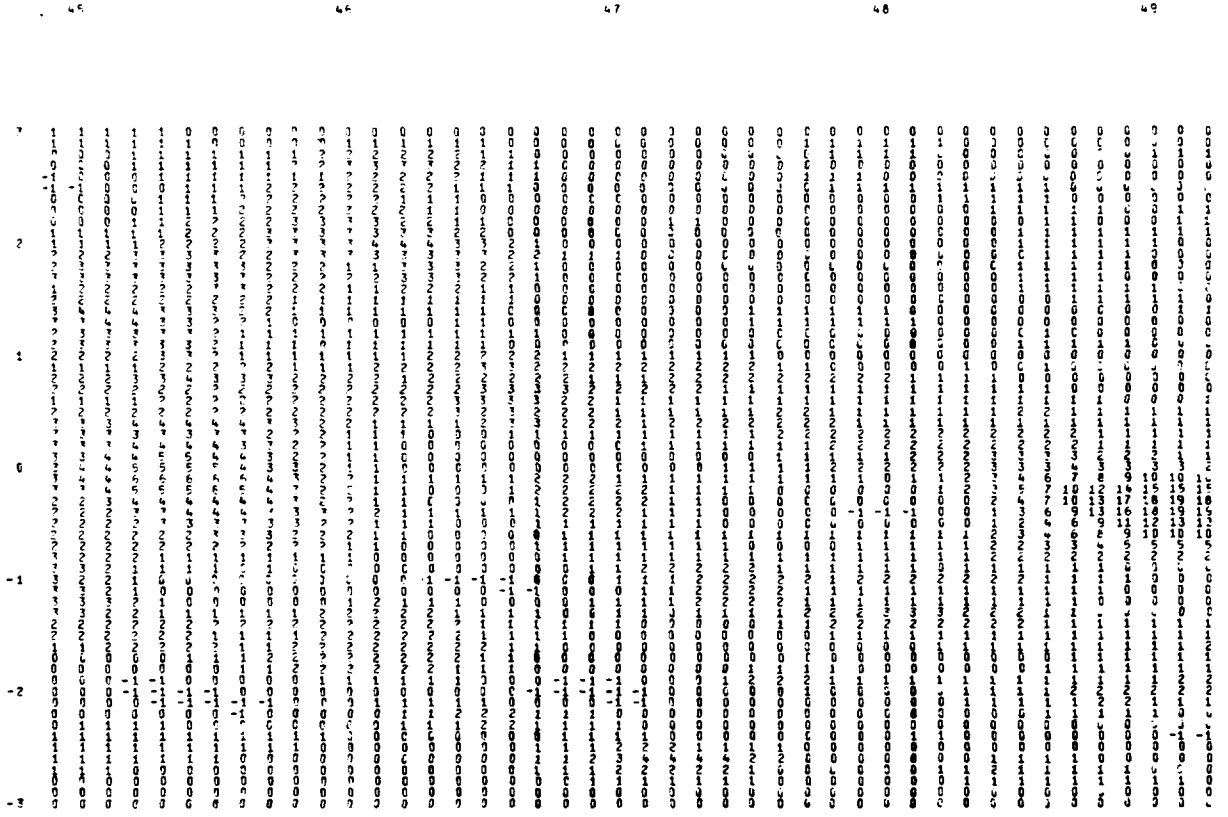

Table B3. 27-μm Grid of Intensities Along the Galactic Plane Between 40° and 85° Longitude (units in 10^{-11} W cm^{-2} μm^{-1} sr^{-1}) (Cont.)

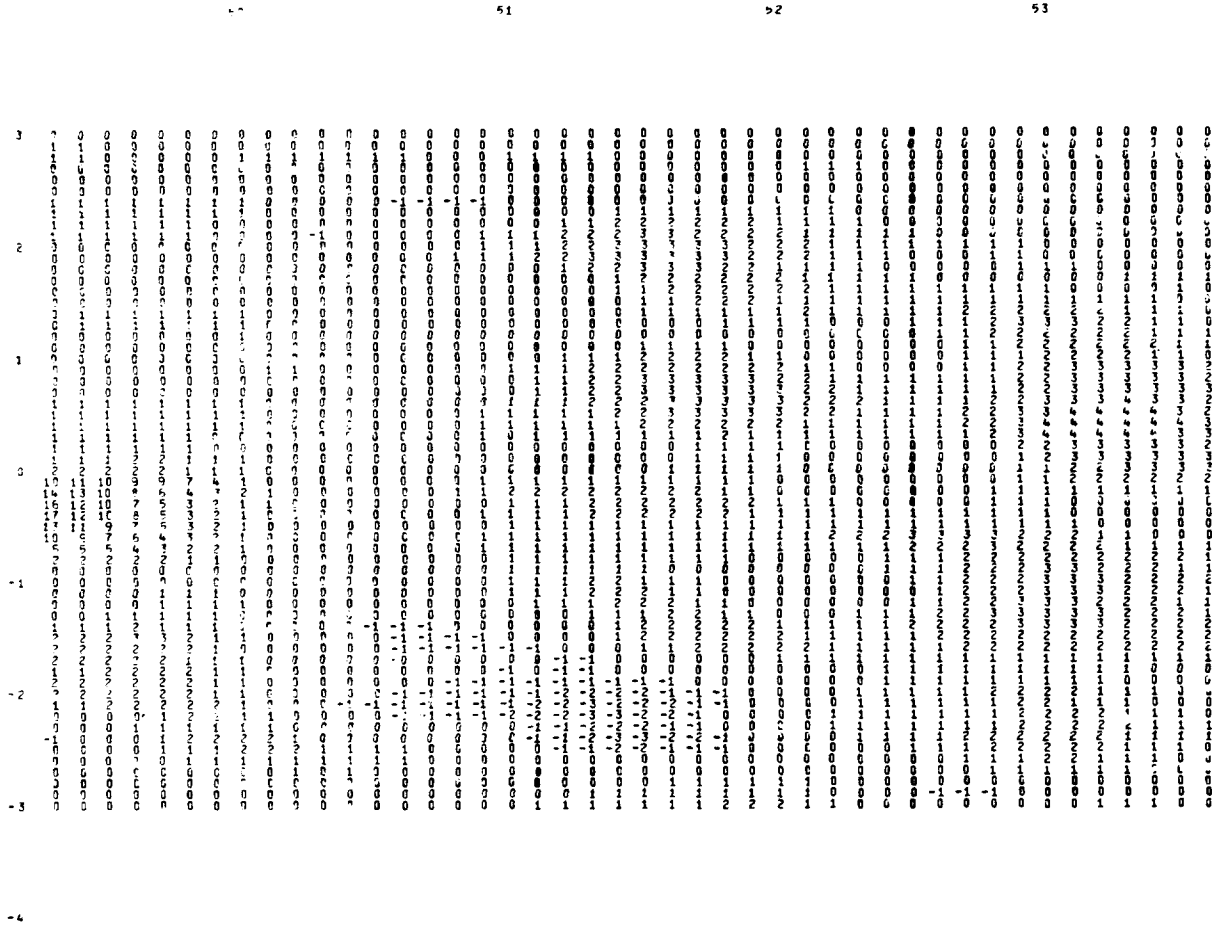

Table B3. 27μm Grid of Intensities Along the Galactic Plane Between 40° and 85° Longitude (units in 10^{-11} W cm^{-2} μm^{-1} sr^{-1}) (Cont.)

Table B3. 27-μm Grid of Intensities Along the Galactic Plane Between 40° and 85° Longitude (units in 10^{-11} W cm^{-2} μm^{-1} sr^{-1}) (Cont.)

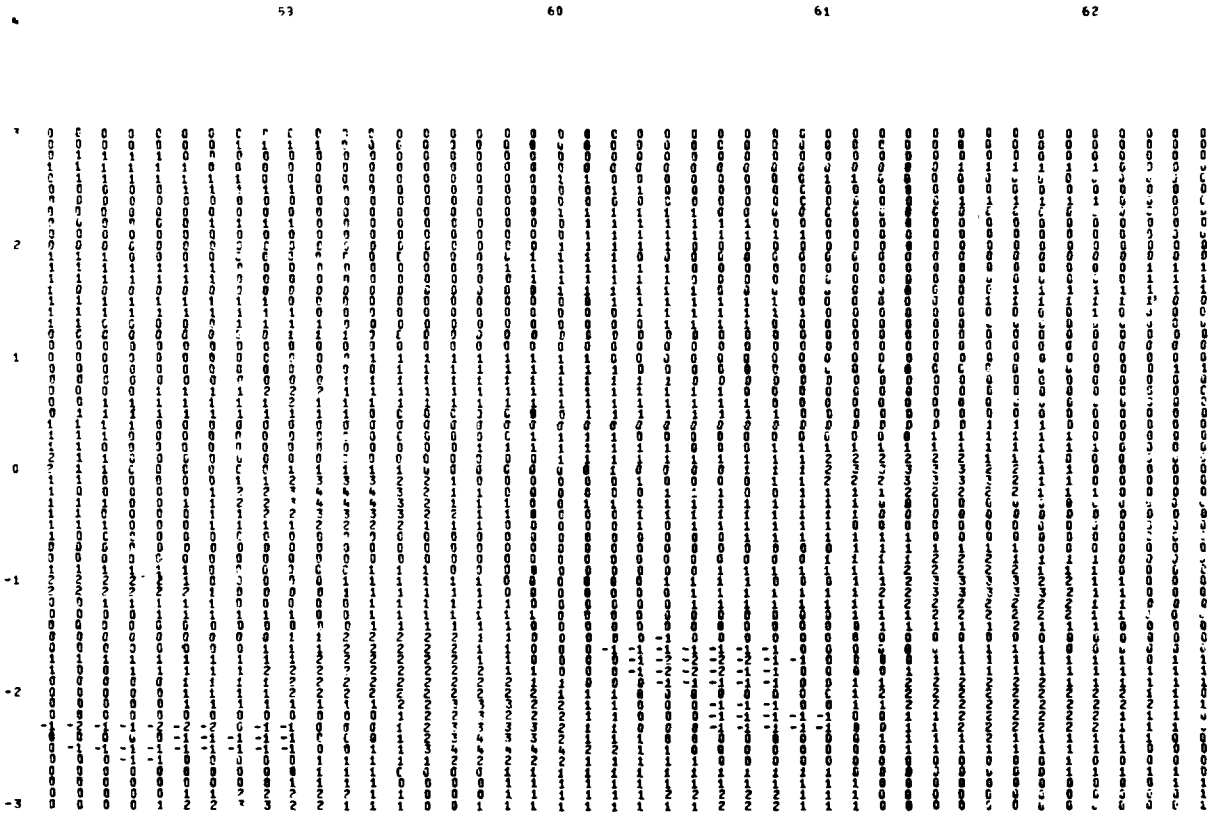

Table B3. 27-μm Grid of Intensities Along the Galactic Plane Between 40° and 85° Longitude (units in 10^{-11} W cm^{-2} μm^{-1} sr^{-1}) (Cont.)

Table B3. 27μm Grid of Intensities Along the Galactic Plane Between 40° and 85° Longitude (units in 10^{-11} W cm^{-2} μm^{-1} sr^{-1}) (Cont.)

Table B3. 27-μm Grid of Intensities Along the Galactic Plane Between 40° and 85° Longitude (units in 10^{-11} W cm^{-2} μm^{-1} sr^{-1}) (Cont.)

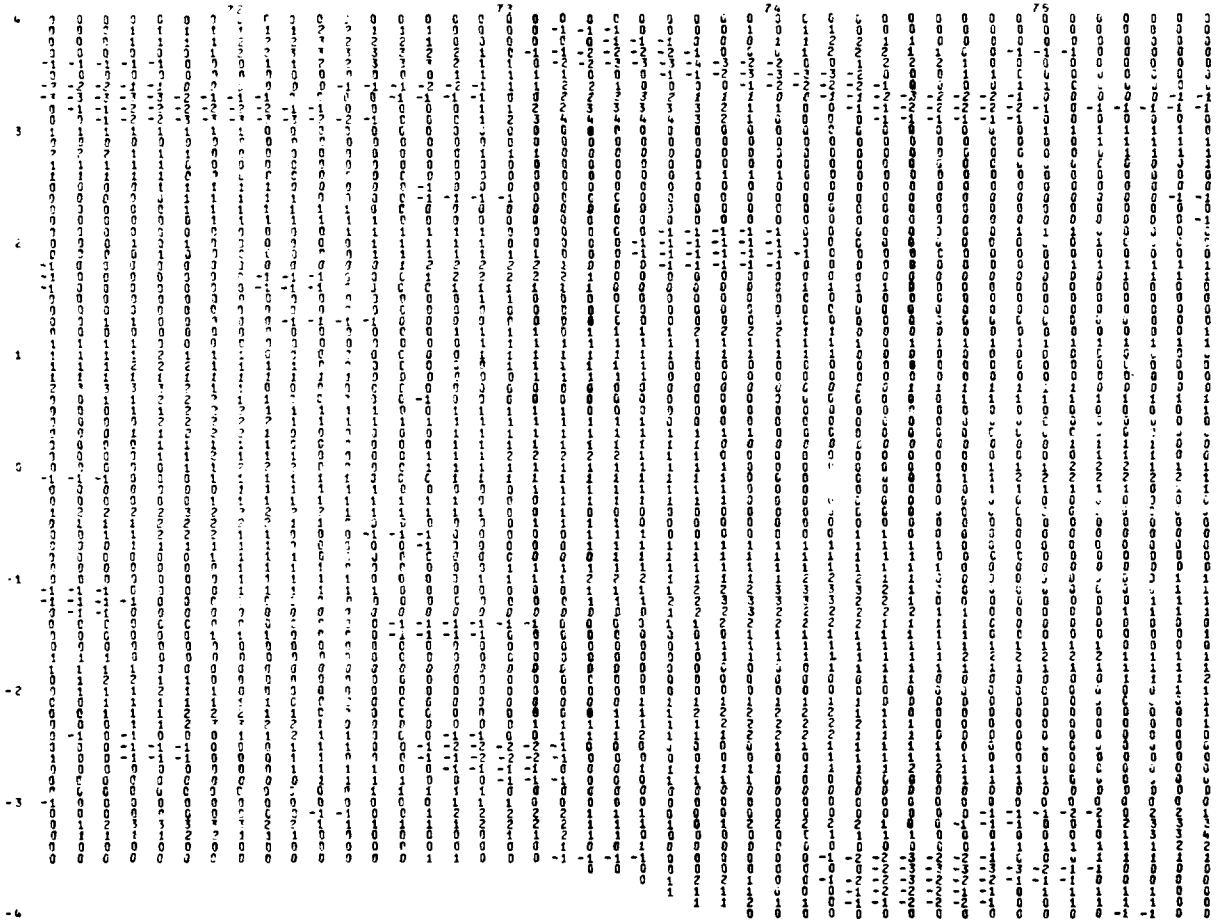

Table B3. 27-μm Grid of Intensities Along the Galactic Plane Between 40° and 85° Longitude (units in 10^{-11} W cm^{-2} μm^{-1} sr^{-1}) (Cont.)

Table B3. 27-μm Grid of Intensities Along the Galactic Plane Between 40° and 85° Longitude (units in 10^{-11} W cm^{-2} μm^{-1} sr^{-1}) (Cont.)

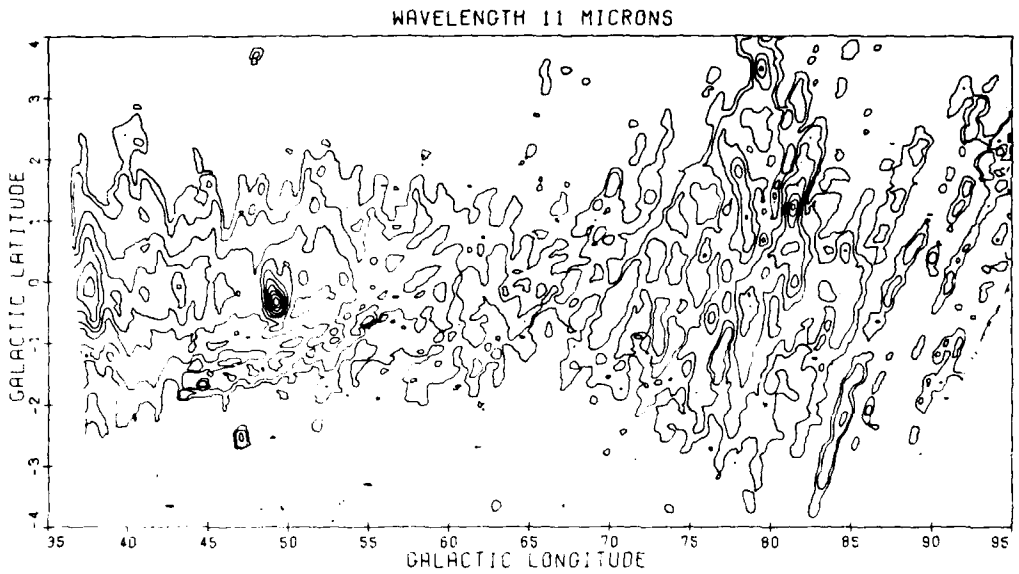

Figure B1. 11-μm Map along the Galactic Plane Between $35^{\circ} < \ell < 95^{\circ}$. Contour levels are 1, 2, 4, 6, ... $\times 10^{-11}$ W cm^{-2} μm^{-1} sr^{-1}

Figure B2. 20-μm Map of the Galactic Plane in the Region $40^{\circ} < \ell < 85^{\circ}$. Contour levels are 0.5, 1, 2, 3, ... $\times 10^{-11}$ W cm^{-2} μm^{-1} sr^{-1}

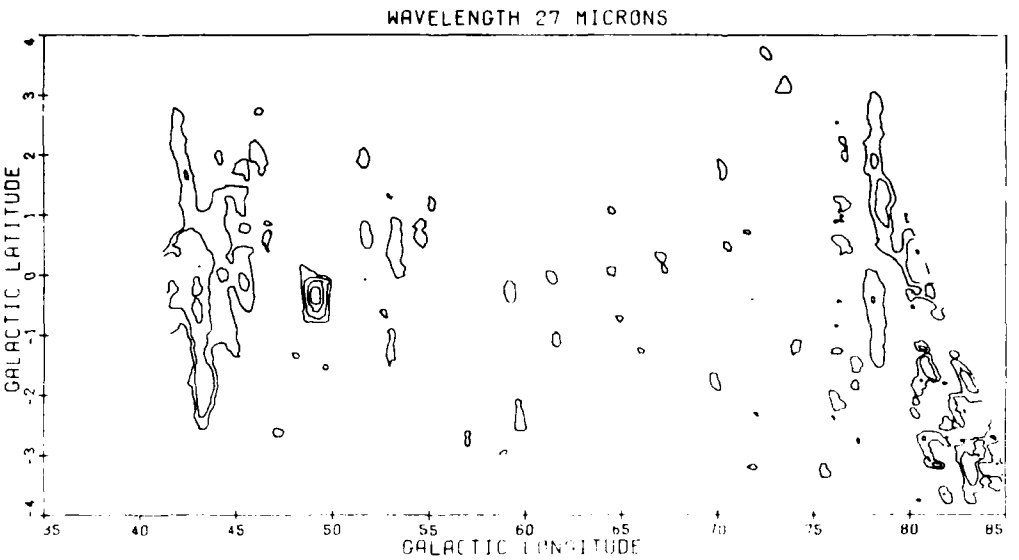

Figure B3. 27-μm Map of the Galactic Plane in the Region $40^{\circ} < \ell < 85^{\circ}$. Contour levels are 2, 5, 5, 10, 15, ... $\times 10^{-11}$ W cm^{-2} μm^{-1} sr^{-1}

Appendix C

Diffuse 11- and 20-μm Measurements Along the Galactic Plane Between 100° and 240° Longitude

No diffuse emission directly associated with the galactic background was observed at these longitudes. Further, the HII regions were observed to be of low surface brightness, for the most part, and reasonably well separated. The confusion and ambiguity in the contour plots are not as much of a problem in this region as for other longitudes. Consequently, the intensity grids do not add much more information than the high resolution plots and were deleted in the interest of saving space.

The 11-and 20-μm contour plots of the restored measurements before averaging over a circular aperture is shown in Figures C1 and C2 for the longitudes between 100° and 170° and in Figures C3 and C4, respectively, for the region between 195° and 245° longitude.

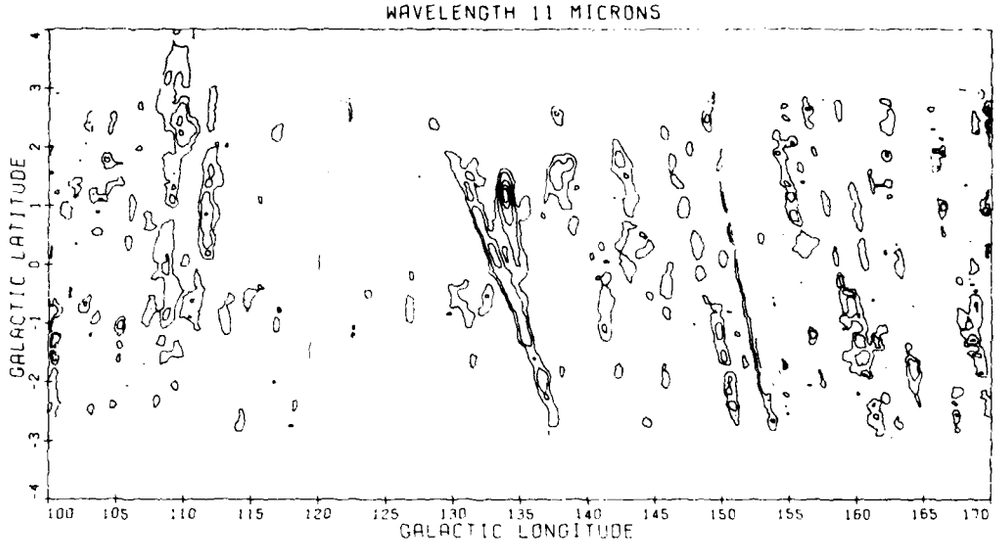

Figure C1. The 11-μm Contour Map Between 100° and 170° Longitude. Contour levels are 1, 2, 4, 6 and 8×10^{-11} W cm^{-2} μm^{-1} sr^{-1} with the peak of 8×10^{-11} W cm^{-2} μm^{-1} sr^{-1} centered on the W3 complex at $\ell \sim 134^{o}$ and $b \sim +1^{o}$. Resolution is about $0.^{o}5$ in latitude and $0.^{o}8$ in longitude with sources smaller than $0.^{o}2$ across being eliminated

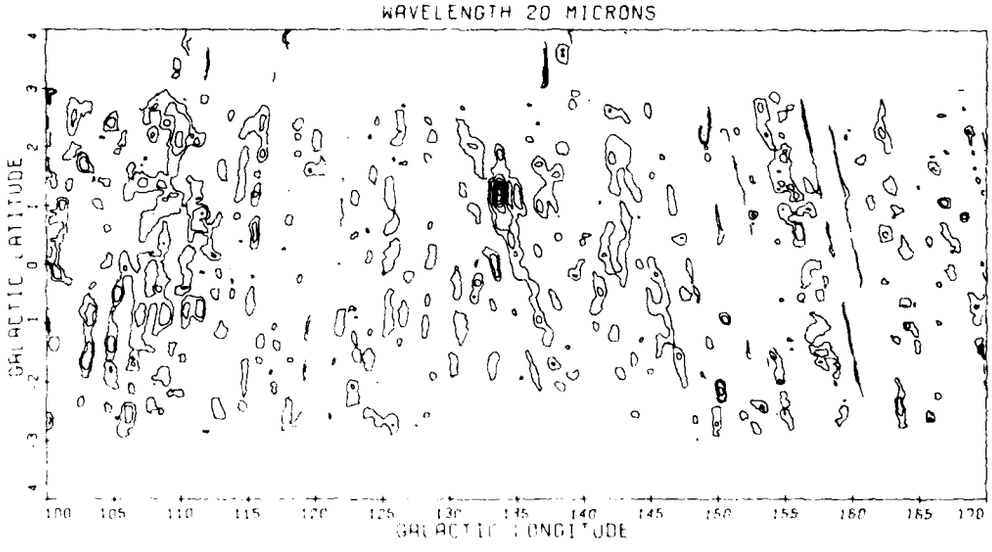

Figure C2. The 20-μm Contour Map Between 100° and 175° Longitude. Contour levels are 0.5, 1, 2, 3, 4, 5 and 6×10^{-11} W cm^{-2} μm^{-1} sr^{-1} with the highest level at the W3 complex. The resolution is $0.^{o}4$ by $0.^{o}7$ in latitude and longitude

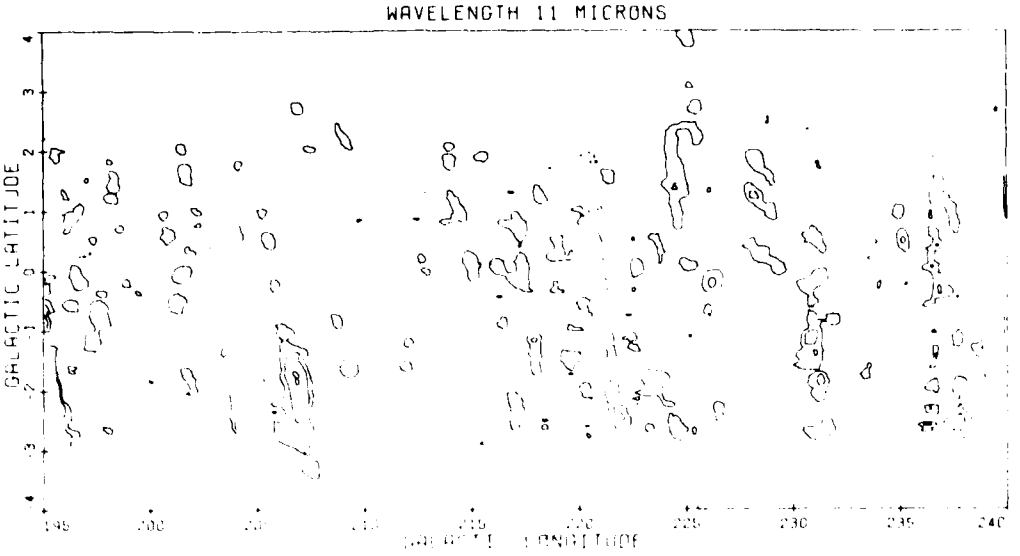

Figure C3. The 11-μm Map Between 195° and 240° Longitude. Contour levels are 1, 2 and 4 $\times$ 10^{-11} W cm^{-2} μm^{-1} sr^{-1}. The peak emission occurs in the NGC 2244 complex, $\ell \sim 207^{o}$ and $b \sim -2^{o}$, although scans across NGC 2244 itself and NGC 2264 were eliminated due to telemetry problems. The spatial resolution is of the order of 0.º5 by 0.º8 in latitude and longitude, respectively

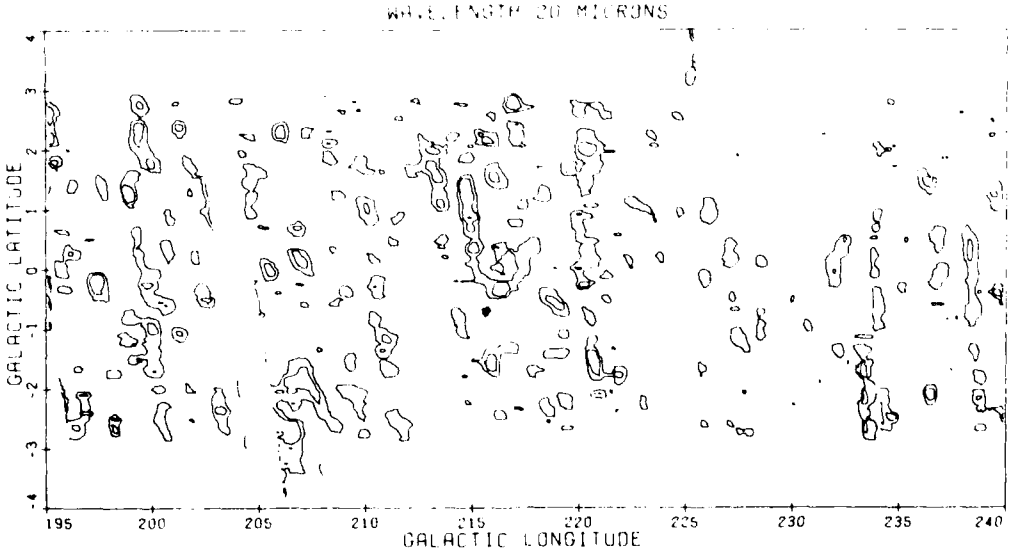

Figure C4. The 20-μm Map of the Region Between 195° and 240° Longitude Along the Galactic Plane. Contour levels are 0.5, 1 and 2 $\times$ 10^{-11} W cm^{-2} μm^{-1} sr^{-1}

Appendix D

Intensity Grids in the 11-, 20- and 27-μm Spectral Bands Covering the Regions $280^{o} \lesssim \ell \lesssim 320^{o}$, $|b| \lesssim 4^{o}$

The grids of the intensities in this region are given in Table D1 for 11-μm observations; Table D2 for the 20-μm values and Table D3 for the 27-μm data. The format is the same as for the grids in the other Appendices; longitude increases across the page and latitude decreases down the page with every degree labeled in each coordinate. Blank streaks through the data are due to two or more missing adjacent channels. Blank entries are also listed external to the assumed limits of the source.

Figure D1 shows the 11-μm contour map generated from the same data base used for Table D1. The 20 and 27-μm iso-intensity plots are shown in Figures D2 and D3, respectively.

PRECEDING PAGE BLANK-NOT FILMED

Table D1. Grid of 11-μm Intensities Along the Galactic Plane Between $-30^{\circ} \leq \ell \leq 320^{\circ}$ (units in 10^{-11} W cm^{-2} μm^{-1} sr^{-1})

Table D1. Grid of 11-μm Intensities Along the Galactic Plane Between $280^{\circ} \leq \ell \leq 320^{\circ}$ (units in 10^{-11} W cm^{-2} μm^{-1} sr^{-1}) (Cont.)

Table D1. Grid of 11-μm Intensities Along the Galactic Plane Between $280^{\circ} \leq \ell \leq 320^{\circ}$ (units in 10^{-11} W cm^{-2} μm^{-1} sr^{-1}) (Cont.)

Table D1. Grid of 11-μm Intensities Along the Galactic Plane Between $280^{o} \leq \ell \leq 320^{o}$ (units in 10^{-11} W cm^{-2} μm^{-1} sr^{-1}) (Cont.)

Table D1. Grid of 11-μm Intensities Along the Galactic Plane Between $280^{\circ} \leq \ell \leq 320^{\circ}$ (units in 10^{-11} W cm^{-2} μm^{-1} sr^{-1}) (Cont.)

Table D1. Grid of 11-μm Intensities Along the Galactic Plane Between $280^{\circ} \leq \ell \leq 320^{\circ}$ (units in 10^{-11} W cm^{-2} μm^{-1} sr^{-1}) (Cont.)

Table D1. Grid of 11-μm Intensities Along the Galactic Plane Between $280^{\circ} \leq \ell \leq 320^{\circ}$ (units in 10^{-11} W cm^{-2} μm^{-1} sr^{-1}) (Cont.)

Table D1. Grid of 11-μm Intensities Along the Galactic Plane Between $280^{o} \leq \ell \leq 320^{o}$ (units in 10^{-11} W cm^{-2} μm^{-1} sr^{-1}) (Cont.)

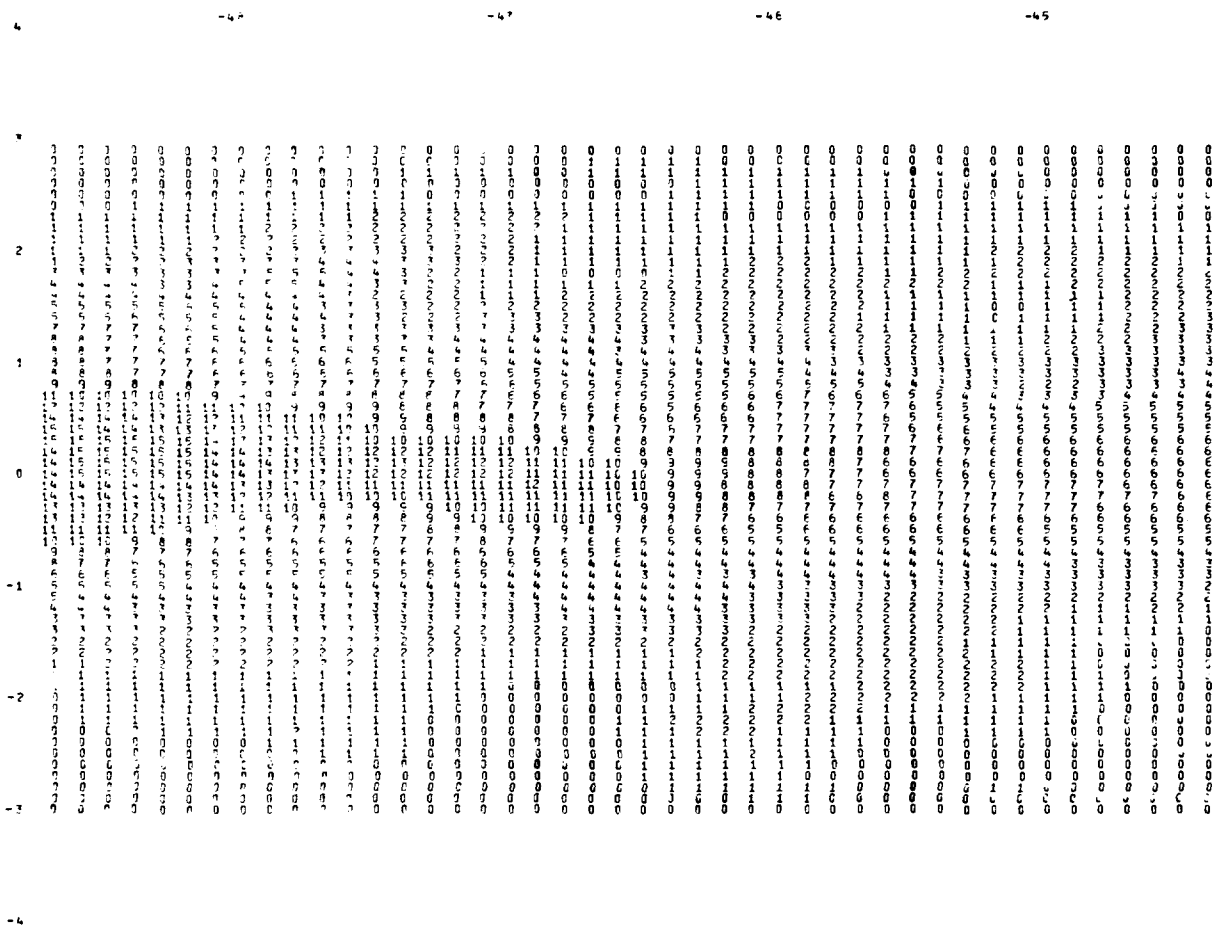

Table D1. Grid of 11-μm Intensities Along the Galactic Plane Between $280^{o} \leq \ell \leq 320^{o}$ (units in 10^{-11} W cm^{-2} μm^{-1} sr^{-1}) (Cont.)

Table D2. Grid of 23-μm Intensities Along the Galactic Plane Between $280^{o} \leq \ell \leq 318^{o}$ (units in 10^{-11} W cm^{-2} μm^{-1} sr^{-1})

Table D2. Grid of 20-μm Intensities Along the Galactic Plane Between $280^{\circ} \leq l \leq 318^{\circ}$ (units in 10^{-11} W cm^{-2} μm^{-1} sr^{-1}) (Cont.)

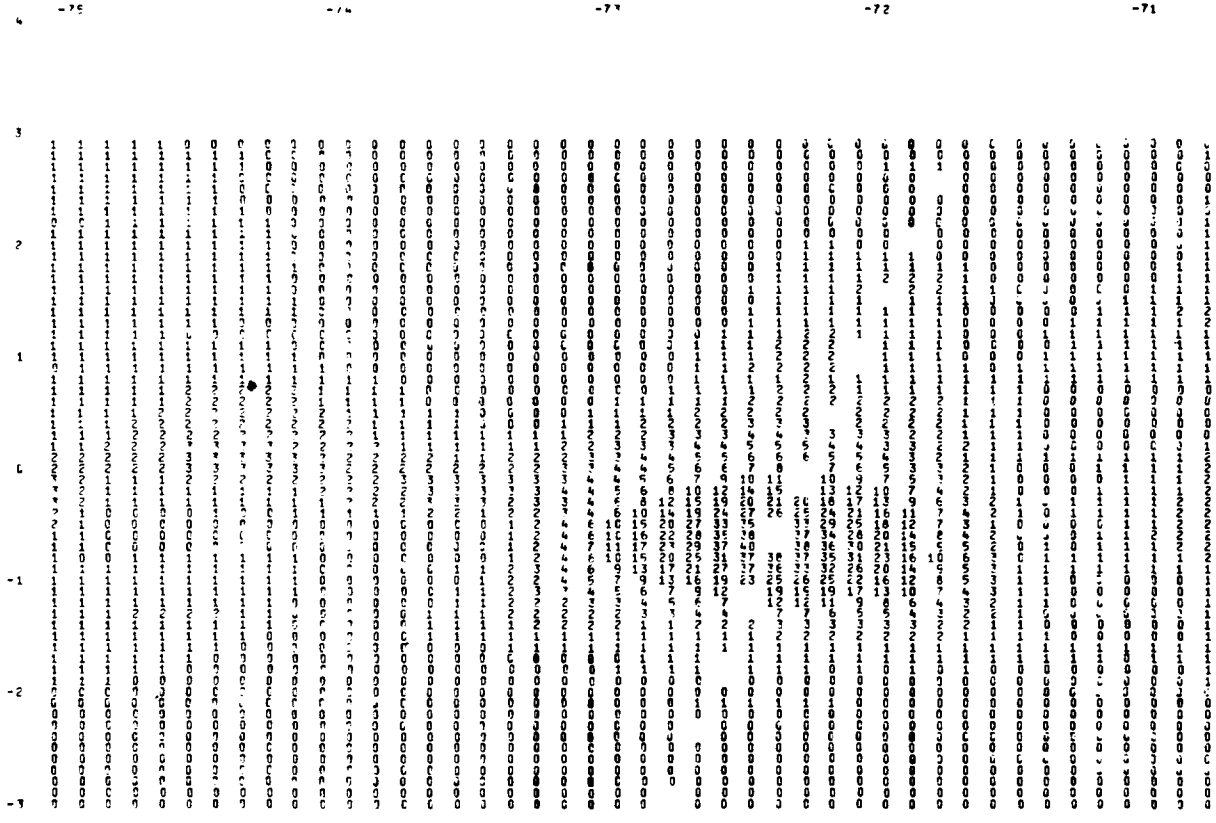

Table D2. Grid of 20-μm Intensities Along the Galactic Plane Between $280^{\circ} \leq \ell \leq 318^{\circ}$ (units in 10^{-11} W cm^{-2} μm^{-1} sr^{-1}) (Cont.)

Table D2. Grid of 20-μm Intensities Along the Galactic Plane Between $280^{\circ} \leq \ell \leq 318^{\circ}$ (units in 10^{-11} W cm^{-2} μm^{-1} sr^{-1}) (Cont.)

Table D2. Grid of 20-μm Intensities Along the Galactic Plane Between $280^{\circ} \leq \ell \leq 318^{\circ}$ (units in 10^{-11} W cm^{-2} μm^{-1} sr^{-1}) (Cont.)

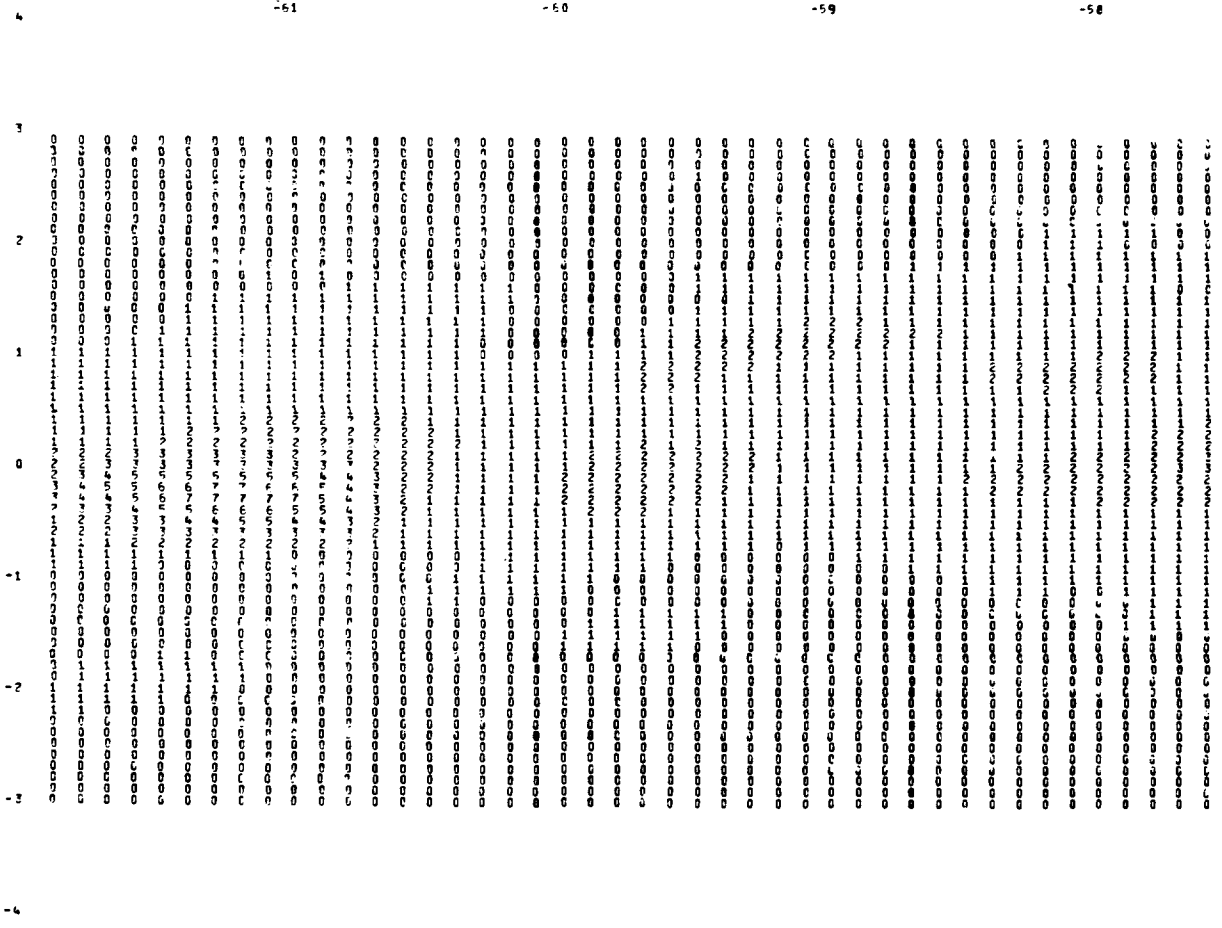

Table D2. Grid of 20μm Intensities Along the Galactic Plane Between $280^{o} \leq \ell \leq 318^{o}$ (units in 10^{-11} W cm^{-2} μm^{-1} sr^{-1}) (*Cont.*)

Table D2. Grid of 20-μm Intensities Along the Galactic Plane Between $280^{\circ} \leq \ell \leq 318^{\circ}$ (units in 10^{-11} W cm^{-2} μm^{-1} sr^{-1}) (Cont.)

Table D2. Grid of 20-μm Intensities Along the Galactic Plane Between $280^{\circ} \leq \ell \leq 318^{\circ}$ (units in 10^{-11} W cm^{-2} μm^{-1} sr^{-1}) (Cont.)

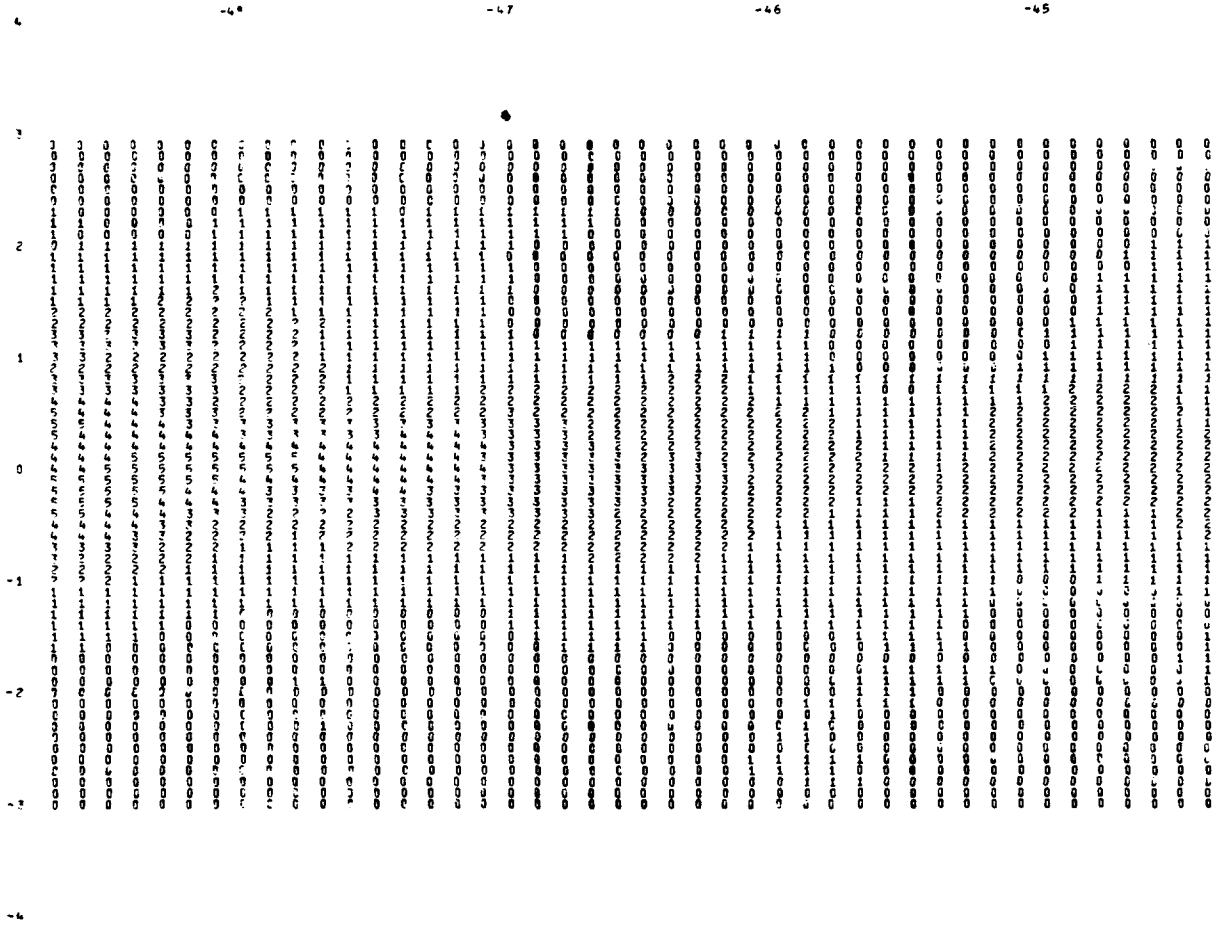

Table D2. Grid of 20 μm Intensities Along the Galactic Plane Between $280^{\circ} \leq \ell \leq 318^{\circ}$ (units in 10^{-11} W cm^{-2} μm^{-1} sr^{-1}) (Cont.)

Table B3. Grid of 27-μm Intensities Along the Galactic Plane Between $280^{\circ} \lesssim \ell \lesssim 318^{\circ}$ (units in 10^{-11} W cm^{-2} μm^{-1} sr^{-1})

Table D3. Grid of 27-μm Intensities Along the Galactic Plane Between $280^{\circ} \lesssim \ell \lesssim 318^{\circ}$ (units in 10^{-11} W cm^{-2} μm^{-1} sr^{-1}) (Cont.)

Table D3. Grid of 27-μm Intensities Along the Galactic Plane Between $280^{\circ} \lesssim l \lesssim 318^{\circ}$ (units in 10^{-11} W cm^{-2} μm^{-1} sr^{-1}) (Cont.)

Table D3. Grid of 27-μm Intensities Along the Galactic Plane Between $280^{o} \lesssim \ell \lesssim 318^{o}$ (units in 10^{-11} W cm^{-2} μm^{-1} sr^{-1}) (Cont.)

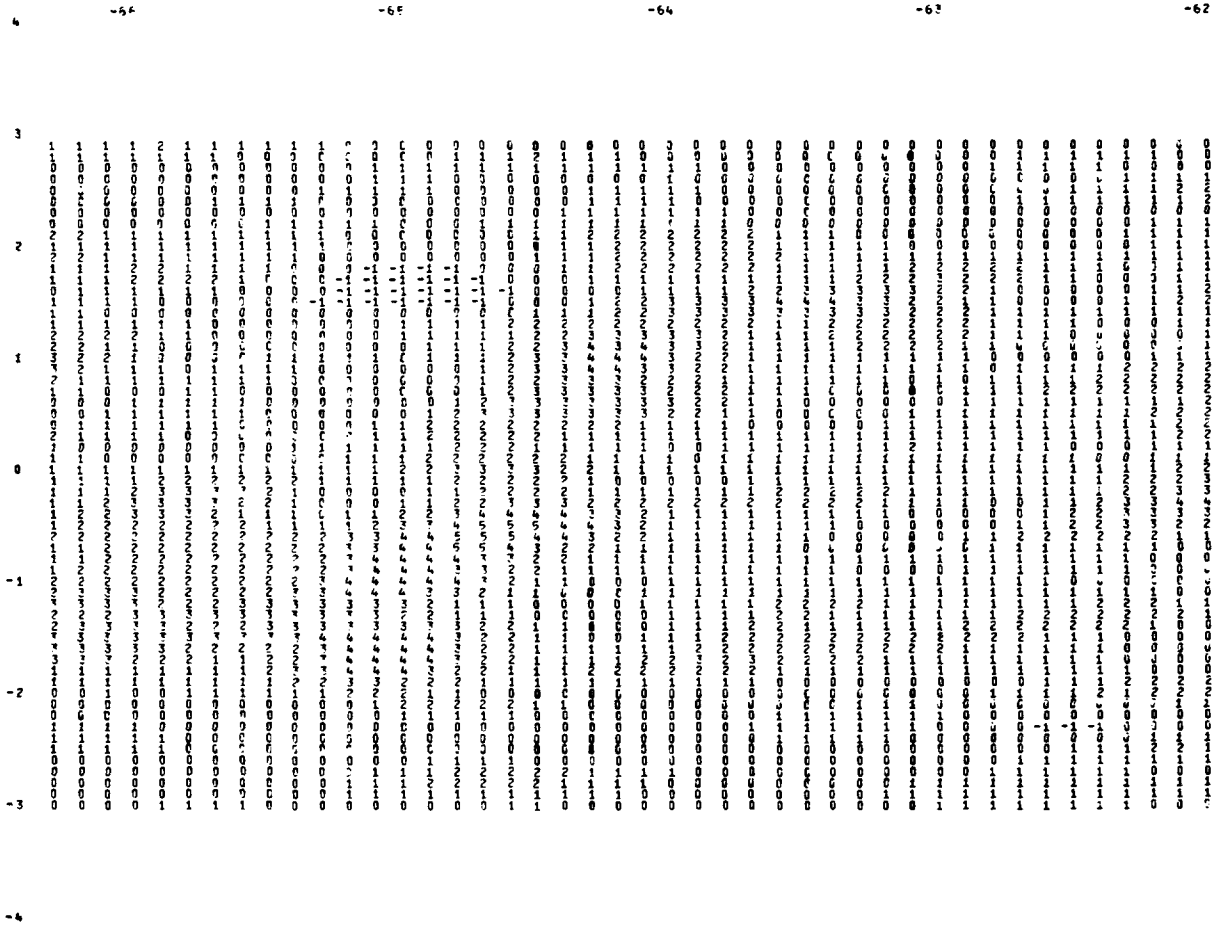

Table D3. Grid of 27-μm Intensities Along the Galactic Plane Between $280^{\circ} \lesssim \ell \lesssim 318^{\circ}$ (units in 10^{-11} W cm^{-2} μm^{-1} sr^{-1}) (Cont.)

Table D3. Grid of 27-μm Intensities Along the Galactic Plane Between $280^{\circ} \lesssim \ell \lesssim 318^{\circ}$ (units in 10^{-11} W cm^{-2} μm^{-1} sr^{-1}) (Cont.)

	-7	-56	-55	-54
[illegible]	[illegible]	[illegible]	[illegible]	[illegible]

Table D3. Grid of 27-μm Intensities Along the Galactic Plane Between $280^{\circ} \lesssim \ell \lesssim 318^{\circ}$ (units in 10^{-11} W cm^{-2} μm^{-1} sr^{-1}) (Cont.)

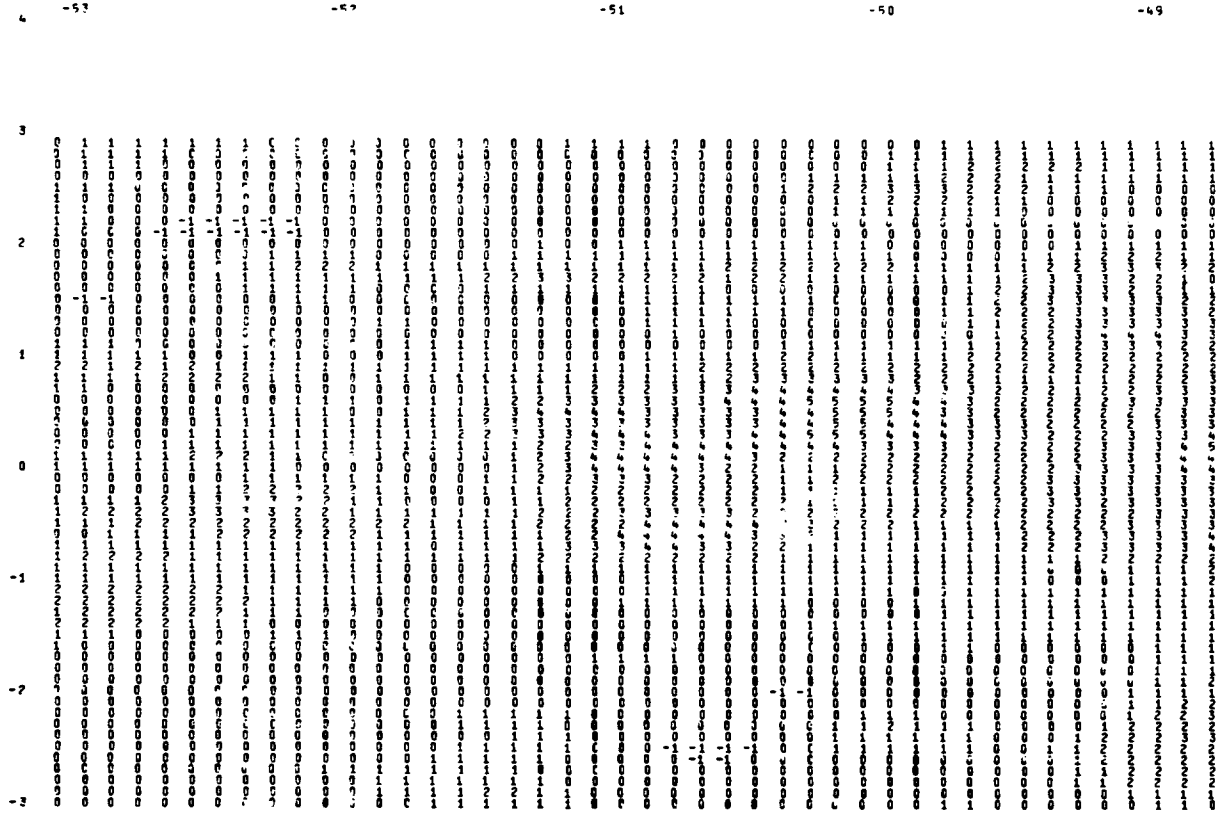

Table D3. Grid of 27-μm Intensities Along the Galactic Plane Between $280^{\circ} \lesssim l \lesssim 318^{\circ}$ (units in 10^{-11} W cm^{-2} μm^{-1} sr^{-1}) (Cont.)

Table D3. Grid of 27-μm Intensities Along the Galactic Plane Between $280^{\circ} \lesssim \ell \lesssim 318^{\circ}$ (units in 10^{-11} W cm^{-2} μm^{-1} sr^{-1}) (Cont.)

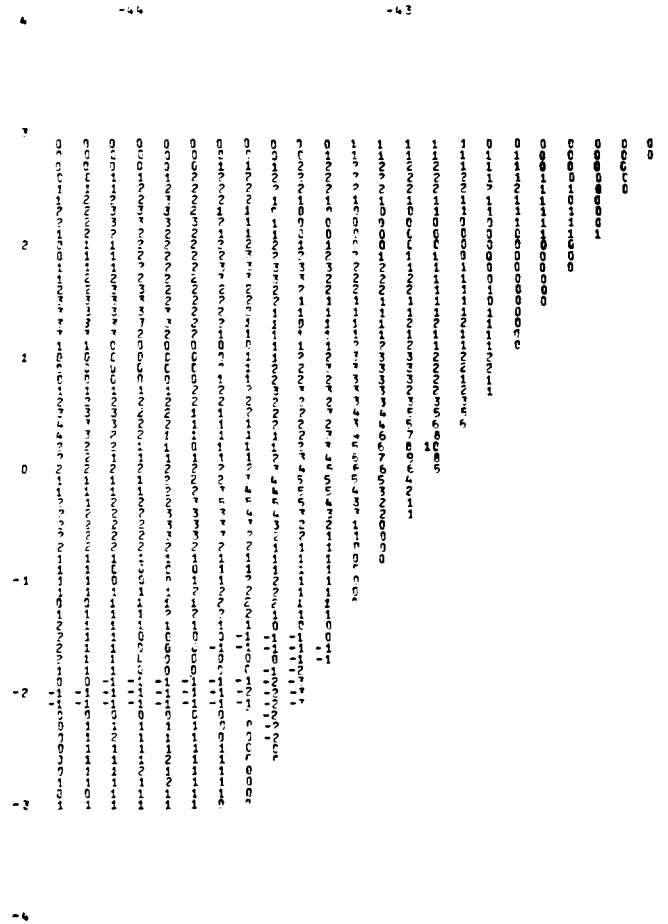

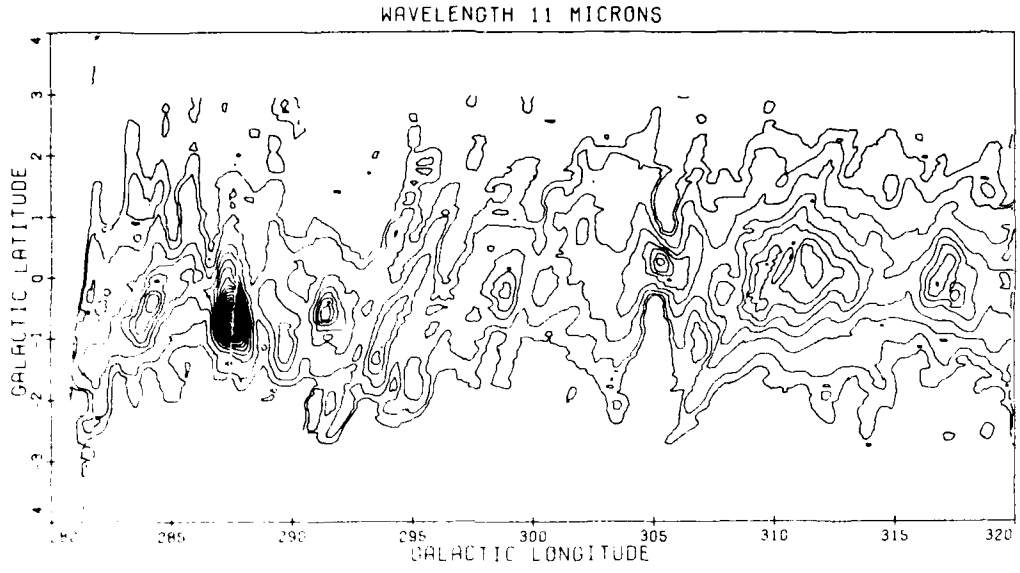

Figure D1. 11-μm Contour Map. Iso-intensity map of the 11-μm measurements along the galactic plane from 280° to 320° longitude using the same data base as Table D1. Lowest and outermost contour is 1×10^{-11} W cm^{-2} μm^{-1} sr^{-1}, next contour brightness is 2×10^{-11} W cm^{-2} μm^{-1} sr^{-1} with each succeeding level being an increase of 2×10^{-11} W cm^{-2} μm^{-1} sr^{-1}; that is, 1, 2, 4, 6, ... $\times 10^{-11}$ W cm^{-2} μm^{-1} sr^{-1}

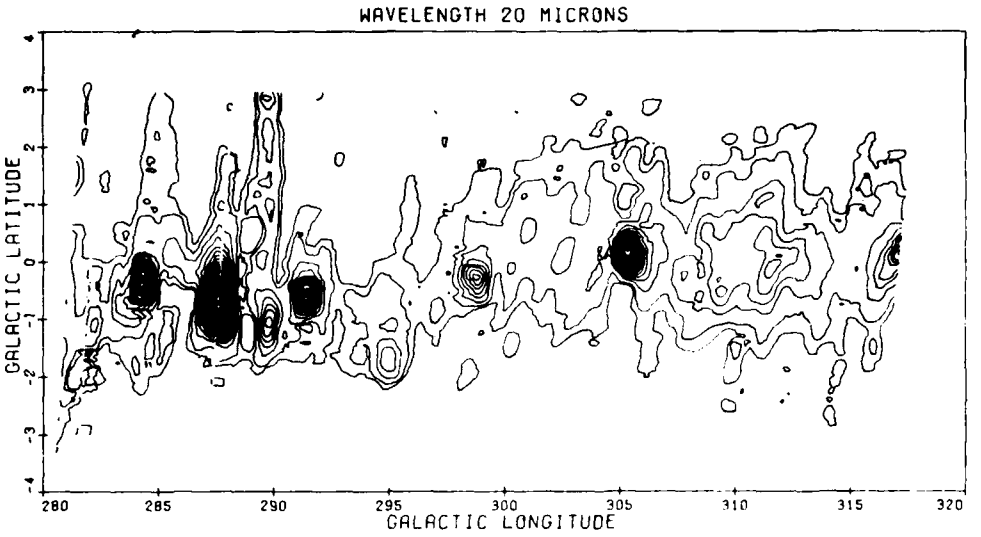

Figure D2. 20-μm Contour Map. The iso-intensity map of the 20-μm data used for Table D2 along the galactic plane from $280^{\circ} \leq \ell \leq 320^{\circ}$. Lowest contour value is set at 5×10^{-12} W cm^{-2} μm^{-1} sr^{-1}, the next brighter level is 1×10^{-11} W cm^{-2} μm^{-1} sr^{-1} with each succeeding level being an increase of 1×10^{-11} W cm^{-2} μm^{-1} sr^{-1}; that is, 0.5, 1, 2, 3, 4, ... $\times 10^{-11}$ W cm^{-2} μm^{-1} sr^{-1}

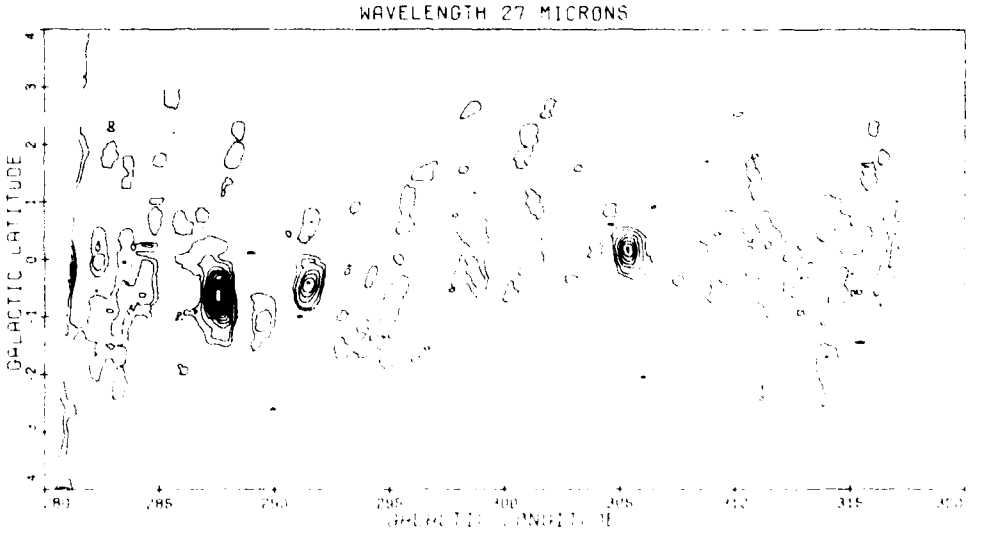

Figure D3. 27-μm Contour Map. Iso-intensity plot of the 27-μm measurements used to generate Table D3. These data span the region of 280° to 320° longitude and -4° to $+4^{\circ}$ latitude. The lowest contour is set at 2.5×10^{-11} W cm^{-2} μm^{-1} sr^{-1}, the next brightest is 5×10^{-11} W cm^{-2} μm^{-1} sr^{-1}